Water flow and solute transport in the *stream corridor* :

hyporheic flow directions, parameter identifiability and transient storage processes

Die approbierte gedruckte Originalversion dieser Dissertation ist an der TU Wien Bibliothek verfügbar.
The approved original version of this doctoral thesis is available in print at TU Wien Bibliothek.
TU Bibliothek Your knowledge hub

Vienna Doctoral Programme on
Water Resource Systems

Doctoral Thesis

Water flow and solute transport in the stream corridor: hyporheic flow directions, parameter identifiability and transient storage processes

submitted in satisfaction of the requirements for the degree of
Doctor of Science in Civil Engineering
of the Vienna University of Technology, Faculty of Civil Engineering

as part of the
Vienna Doctoral Programme on Water Resource System

by

Dott. Mag. Ing. **Enrico Bonanno**
Matr. Number: 11729005

Examiner: Univ.Prof. Dipl.-Ing. Dr.techn. **Günter Blöschl**
Fakultät für Bau- und Umweltingenieurwesen,
Technische Universität Wien
Karlspatz 13/222/2, 1040 Wien, Österreich
Examiner: Univ.Prof. Dr. rer. nat **Julian Klaus**
Geographische Institut,
Universität Bonn
Meckenheimer Allee 166 - 53115 Bonn, Deutschland
Examiner: Professore Associato Ing. **Fulvio Boano**
Department of Environment, Land, and Infrastructure Engineering,
Politecnico di Torino,
Corso Duca degli Abruzzi, 24, 10129, Torino, Italy
Examiner: Prof. Affil. Dr. habil. **Laurent Pfister**
Faculty of Science, Technology and Medicine
University of Luxembourg
2, Av. de l'Universite, 4365, Esch-sur-Alzette, Luxembourg

Vienna, 21 February 2023 ______________________________

Die approbierte gedruckte Originalversion dieser Dissertation ist an der TU Wien Bibliothek verfügbar.
The approved original version of this doctoral thesis is available in print at TU Wien Bibliothek.
TU Bibliothek Your knowledge hub

Vienna Doctoral Programme on
Water Resource Systems

Dissertation

Wasser- und Stofftransport im Flusskorridor: Hyporheische Fließrichtung, Identifizierbarkeit von Modellparametern und instationäre Speicherprozesse

ausgeführt zum Zwecke der Erlangung des akademischen Grades eines
Doktors der technischen Wissenschaft
eingereicht an der Technischen Universität Wien, Fakultät für Bauingenieurwesen

als Teil des
Doktoratskolleg für Water Resource Systems

von

Dott. Mag. Ing. **Enrico Bonanno**
Matrikelnummer: 11729005

Gutachter: Univ.Prof. Dipl.-Ing. Dr.techn. **Günter Blöschl**
Fakultät für Bau- und Umweltingenieurwesen,
Technische Universität Wien
Karlspatz 13/222/2, 1040 Wien, Österreich

Gutachter: Univ.Prof. Dr. rer. nat **Julian Klaus**
Geographische Institut,
Universität Bonn
Meckenheimer Allee 166 - 53115 Bonn, Deutschland

Gutachter: Professore Associato Ing. **Fulvio Boano**
Department of Environment, Land, and Infrastructure Engineering,
Politecnico di Torino,
Corso Duca degli Abruzzi, 24, 10129, Torino, Italy

Gutachter: Prof. Affil. Dr. habil. **Laurent Pfister**
Faculty of Science, Technology and Medicine
University of Luxembourg
2, Av. de l'Universite, 4365, Esch-sur-Alzette, Luxembourg

Wien, 21 Februar 2023

To my sisters, to my parents
with love and gratitude

Acknowledgements

I want to express my gratitude to Professor Julian Klaus and Professor Günter Blöschl. Thank you for the massive amount of time you dedicated to me, for guiding me through my mistakes, for pushing me back on track when I was losing it, and for mentoring me day by day on how to be a scientist in the most powerful way: with your example and your flaming dedication.

I would like to express my profound gratitude to the Catchment and Ecohydrology group and the Observatory for Climate, Environment and Biodiversity group. The bright scientific exchanges I had in the office, together with the great support and teaching I received in the fieldwork activities, made me grow both in terms of rigorous thinking and in terms of pragmatism. A special thanks to Laurent Pfister for being tireless, supportive, and for providing wise guidance in the toughest times. I am also especially grateful to Jean François Iffly for his experience and his grumpy, yet warm, assistance.

I would like to thank all the colleagues met at the Luxembourg Institute of Science and Technology and the Institute of Hydraulic Engineering and Water Resources Management at the Vienna University of Technology. I feel grateful to have met so many brilliant people whom I have had the pleasure of calling "friends".

To my parents, the brightest reference points in my life as a young man. If today I am half the man you taught me to be, it is only thanks to you.

To my sisters, both sensitive and strong souls, always too far away. Thank you for your temperance and for being a vivid example of constant improvement.

To my grandparents, a continuous pure spring of love, support and dedication. Your words are always with me, holding my body, and your sweet smiles comfort my days, wherever I am.

To Ginevra. My charming bay, my luminous meadow, my breathing forest. My curious wind, my generous mountain stream. Day after day, you make me want to become a better man.

Die approbierte gedruckte Originalversion dieser Dissertation ist an der TU Wien Bibliothek verfügbar.
The approved original version of this doctoral thesis is available in print at TU Wien Bibliothek.
TU Bibliothek WIEN Your knowledge hub

Contents

List of Tables 13

List of Figures 14

Abstract 17

Zusammenfassung 19

Introduction 22

Chapter 1: Flow directions of stream-groundwater exchange in a headwater catchment during the hydrologic year 30

- Graphical abstract 30
- 1.1 Abstract 31
- 1.2 Introduction 31
- 1.3 Study site 33
- 1.4 Methods 35
  - 1.4.1 Observation of the groundwater table 35
  - 1.4.2 ERT measurements 36
  - 1.4.3 Analysis of precipitation events and groundwater flow direction 36
- 1.5 Results 38
  - 1.5.1 Groundwater and streamflow dynamics 38
  - 1.5.2 Spatiotemporal dynamics of groundwater flow direction 42
- 1.6 Discussion 45
  - 1.6.1 Drivers of near-stream groundwater dynamics 45
    - 1.6.1.1 Role of depth-dependent storage capacity on groundwater response 45
    - 1.6.1.2 Role of precipitation characteristics on groundwater response 46
    - 1.6.1.3 Role of regolith thickness above the fractured bedrock on groundwater response 47
  - 1.6.2 Drivers of near-stream groundwater flow directions depending on hydrologic conditions 48

1.6.2.1 Role of upslope-footslope connectivity and streamwater level 48

1.6.2.2 The role of surface topography and anisotropic hydraulic conductivity of the fractured bedrock 50

1.6.3 Implications for runoff generation and hydrological connectivity 50

1.7 Conclusions 51

1.8 Acknowledgements 52

Chapter 2: Exploring tracer information in a small stream to improve parameter identifiability and enhance the process interpretation in transient storage models 54

2.1. Abstract 54

2.2 Introduction 55

2.2 Study site and methods 58

2.2.1 Study site and tracer data 58

2.2.2 Advection-dispersion equation and Transient Storage Model formulation 58

2.2.3 Random sampling and global identifiability analysis 59

2.2.4 Identifiability analysis on specific sections of the BTC 60

2.2.5 Iterative approach to achieve model identifiability 61

2.2.6 Number of parameter sets, parameter range, and identifiability of model parameters 63

2.2.7 Comparison with an inverse modelling scheme and a Monte Carlo random sampling approach 63

2.2.8 Metrics and hydrologic interpretation of TSM results 65

2.3 Results 65

2.3.1 ADE parameters 65

2.3.2 TSM parameters 65

2.3.2.1 Identifiability of model parameters when velocity is considered as a calibration parameter 65

2.3.2.2 Identifiability of model parameters when velocity is set equal to v_{peak} 66

2.3.3 Dynamic identifiability analysis 67

2.3.3.1 Dynamic identifiability analysis when velocity is considered as a calibration parameter 67

2.3.3.2 Dynamic identifiability analysis when velocity is set equal to v_{peak} 68

2.3.4 Role of the used parameter range and the number of parameter sets for the identifiability of model parameters 70

2.3.5 Comparison with OTIS-P and OTIS-MCAT results 70

Die approbierte gedruckte Originalversion dieser Dissertation ist an der TU Wien Bibliothek verfügbar.
The approved original version of this doctoral thesis is available in print at TU Wien Bibliothek.
TU WIEN Bibliothek Your knowledge hub

2.3.6 Variation of transport metrics with increasing identifiability of model parameters 71

2.4 Discussion 73

2.4.1 The role of velocity in random sampling approaches for TSM 73

2.4.2 Control of model parameters on the rising limb, the peak, and the tail of the BTC 74

2.4.3 On the importance of parameter range, parameter sets, and challenges associated to parameter identifiability in TSM 76

2.4.4 Implications of identifiable model parameters for hydrologic interpretation of modelling results 78

2.5 Conclusion 79

2.6 Acknowledgements 80

Chapter 3: Discharge, groundwater gradients, and streambed micro-topography control the temporal dynamics of transient storage in a headwater reach 82

3.1 Abstract 82

3.2 Plain Language Summary 83

3.3 Introduction 83

3.4 Methods 90

3.4.1 Study site 90

3.4.2 Tracer experiments 90

3.4.3 Water table measurements and groundwater flow direction 92

3.4.4 Evaluation of streambed micro-topography 92

3.4.5 Formulation of the Transient Storage Model 93

3.4.6 Calibration and identifiability of Transient Storage Model parameters 93

3.4.7 Metrics characterizing solute transport in stream 96

3.5 Results 97

3.5.1 Transient storage model parameters and their identifiability 97

3.5.2 Extension and contraction of the hyporheic zone and development of in-stream dead zones 100

3.5.3 How does transient storage change between experiments? 102

3.6 Discussion 105

3.6.1 Parameter identifiability in the Transient Storage Model depends on discharge during the tracer experiments 105

3.6.2 Dynamics of transient storage processes under different hydrologic conditions 107

3.7 Conclusion 109

3.8 Acknowledgments 110

Chapter 4: Overall conclusions and future outlook 112

References 115

Appendix A 133

Appendix B 136

Appendix C 138

Appendix D 145

Appendix E 149

Appendix F 151

List of Tables

Table 1.1. Subsurface layers in the study site and their properties 35
Table 1.2. Periods of dry, intermediate, and wet conditions and their duration 38
Table 2.1. Parameter names, abbreviations, and units together with a summary of publications that address the identifiability of transient storage model parameters 62
Table 2.2. Summary of the TSM results. 71
Table 3.1. Relationships between transient storage parameters α and ATS and stream discharge Q in published literature 86
Table 3.2. List of the in-stream instantaneous tracer injections, date, discharge from dilution gauging, and amount of injected NaCl 91
Table 3.3. List of calibration parameters and used initial ranges for the first iteration of the random sampling of TSM parameters. 96
Table B. Details for the groundwater and piezometer network at the study site. 136
Table C1 Spearman Rank correlation coefficients between ΔGWH, and precipitation characteristics per each groundwater monitoring well. 138
Table C2 Spearman Rank correlation coefficients between ΔGWT, and precipitation characteristics per each groundwater monitoring well. 141
Table C3 Spearman Rank correlation coefficients between groundwater response to events and morphological properties in the groundwater monitoring network. 144
Table F. Comparison between modelling results via iterative modelling approach and OTIS-P for 31 slug tracer experiments 151

Die approbierte gedruckte Originalversion dieser Dissertation ist an der TU Wien Bibliothek verfügbar.
The approved original version of this doctoral thesis is available in print at TU Wien Bibliothek.
TU Bibliothek Your knowledge hub WIEN

List of Figures

Figure I. A timeline of significant publications contributing to increasing the understanding of water movement in the stream corridor. 24

Figure 1.1. Study reach, location and name of the wells/piezometers and bedrock surface topography in metres above reference plane (m a.r.p.) 34

Figure 1.2. Triangles for the calculation of the groundwater flow direction using the groundwater monitoring well network. 37

Figure 1.3. Time series of precipitation, streamflow, and groundwater level at the study site. 38

Figure 1.4. Groundwater response to precipitation events in the groundwater monitoring well network. 39

Figure 1.5. Event precipitation, streamflow and groundwater level at the study site for selected events during dry, intermediate, and wet hydrologic conditions 41

Figure 1.6. Histograms of the number of wells that have a significant positive and negative Spearman relationship between the groundwater increase (ΔGWH) and groundwater response time (ΔGWt) for different properties of the precipitation events. 42

Figure 1.7. Precipitation and streamflow time series for dry conditions and wet conditions together with the groundwater flow directions at the study site. 43

Figure 1.8. Boxplots of groundwater flow direction α for a selection of triangles (Figure 1.2) 44

Figure 1.9. Precipitation and streamflow together with a zoom on the change in groundwater flow directions for selected precipitation events during dry and wet conditions. 46

Figure 2.1: Conceptual modelling workflow for the iterative modelling approach used for TSM. 64

Figure 2.2. Parameter values plotted against the corresponding RMSE values for the TSM results conducted for the tracer injections 66

Figure 2.3. Same as Figure 2.2, but reporting TSM results when velocity was considered equal to v_{peak} 67

Figure 2.4. Dynamic identifiability analysis of model parameters for E1 when v was considered as a varying model parameter 68

Figure 2.5. Same as Figure 4, but reporting dynamic identifiability results for E1 when velocity was considered equal to v_{peak} 69

Figure 2.6: Mean and standard deviation for RMSE values relative to the top 10% of the modelling results as a function of the number of parameter sets used in the TSM. 70

Figure 2.7. Boxplots of the investigated transport metrics for the best 100 parameter sets for the three simulated experiments. 72

Figure 2.8. Qualitative plots of the TSM parameter influence on different sections of the BTC and comparison with previous studies. 75

Figure 3.1. Description of the study site, transects extracted from LIDAR scans, and discharge stages investigated during the slug tracer injections. 93

Figure 3.2. Results of the iterative modelling approach reported as parameter values plotted against the corresponding RMSE values 98

Figure 3.3. Boxplot of the distributions of model error for the 10% best-performing parameter sets for each slug tracer injection. 99

Figure 3.4. Dependency of the mean and standard deviation of model error for the top 10% of the modelling results on the number of TSM iterations 99

Figure 3.5. Contraction and extension of the size of the hyporheic zone exemplified for two experiments together with the dependency of the size and volume of the hyporheic zone with discharge 101

Figure 3.6. Evaluation of hydraulic radius HR, Darcy-Weisbach friction factor f, Manning's roughness coefficient n, and percentage of the stream reach where the hydraulic radius or the stream water level was higher than the 5-percentile, average, 95-percentile and maximum height of the slate fragment in the streambed against discharge for the 31 tracer experiments 102

Figure 3.7. TSM parameters against discharge during the experiments 103

Figure 3.8. Metrics describing transient storage at the study site against discharge 104

Figure A1. Location of the electrical resistivity tomography (ERT) transects 133

Figure A2. Visual determination of the interface between the subsolum and solum in the riparian wetland by the use of a hand-drilling probe 134

Figure A3. Map of the Weierbach catchment. 135

Figure D1: Examples of the four types of visualizations intended for parameter identifiability and sensitivity 146

Figure D2. Dynamic identifiability analysis algorithm flowchart. 147

Figure D3. Parameter values plotted against the corresponding *RMSE* values for the ADE results for E1, E2, and E3 148

Figure E1: Observed BTC (red line) together with the grey area comprised between the top 100 simulated BTCs and the best-fitting BTC........ 149

Figure E2: Observed BTC (red line) together with the grey area comprised between the top 100 simulated BTCs and the best-fitting BTC for the second TSM iteration (E1) only........ 150

Die approbierte gedruckte Originalversion dieser Dissertation ist an der TU Wien Bibliothek verfügbar.
The approved original version of this doctoral thesis is available in print at TU Wien Bibliothek.
TU Bibliothek Your knowledge hub WIEN

While past in-stream experiments of solute transport were mostly conducted during low flow conditions, Chapter 3 presents results from 31 in-stream tracer experiments carried out in the Weierbach over three hydrologic years that comprise both low flow and high flow conditions. The spatially dense groundwater data from Chapter 1 are used to estimate the extent of the groundwater zone receiving streamwater during each experiment, while the iterative modelling approach from Chapter 2 allows robust estimation of the model parameters for each tracer experiment. The analyses show that the streamwater-groundwater exchange has a decreasing influence on water and solute transport in the stream corridor with increasing discharge. This is because of the relatively lower localised water losses from the stream channel to the adjacent groundwater. Model parameter interaction increases with discharge, due to the dominance of advection-dispersion parameters over transient storage parameters.

Overall, the thesis advances our understanding of hydrological and solute transport processes in stream corridors. The research highlights the role of both morphological and hydrological factors in stream corridor processes, and the dynamics of near-stream water flow directions during the hydrologic year. The results reported in this thesis pave the way for a holistic understanding of water movement through the torrent corridor and contribute to accurate model predictions under different hydrological conditions.

Abflussbedingungen zu simulieren. Die Ergebnisse zeigen, dass die Methode in der Lage ist, identifizierbare Modellparameter zu bestimmen, was in früheren Arbeiten nicht der Fall war. Die Analysen zeigen auch, wie die Kalibrierung der Parameter ohne Bewertung ihrer Identifizierbarkeit zu unsicheren Vorhersagen des Transportes gelöster Stoffe im Flusskorridor führen kann. Die neue Methode verbessert somit die Prozessinterpretation der Parameter.

Während frühere Experimente zum Stofftransport in Fließgewässern meist bei Niederwasserbedingungen durchgeführt wurden, werden in Kapitel 3 die Ergebnisse von 31 Tracerexperimenten im Weierbach vorgestellt, die über drei hydrologische Jahre hinweg durchgeführt wurden und sowohl Nieder- als auch Hochwasserbedingungen umfassen. Die räumlich dichten Grundwasserdaten aus Kapitel 1 werden verwendet, um die Ausdehnung jener Grundwasserzone abzuschätzen, die während jedes Experiments Bachwasser aufnimmt, während der iterative Modellierungsansatz aus Kapitel 2 eine robuste Schätzung der Modellparameter für jedes Tracerexperiment ermöglicht. Die Analysen zeigen, dass der Flusswasser-Grundwasser-Austausch mit zunehmendem Abfluss einen abnehmenden Einfluss auf den Wasser- und Stofftransport im Flusskorridor hat. Dies ist auf die geringen relativen Wasserverluste aus dem Bachlauf in Richtung des angrenzenden Grundwassers zurückzuführen. Die Interaktion der Modellparameter nimmt mit dem Abfluss zu, da die Advektions-Dispersions-Parameter gegenüber den Parametern der instationären Speicherung dominieren.

Insgesamt trägt die Arbeit zu einem besseren Verständnis der hydrologischen Prozesse und des Stofftransports in Flusskorridoren bei. Die Untersuchungen unterstreichen die Rolle sowohl morphologischer als auch hydrologischer Faktoren für die Prozesse in Flusskorridoren und die Dynamik der Strömungsrichtung im bachnahen Grundwasser über das gesamte hydrologische Jahr hinweg. Die in dieser Arbeit berichteten Ergebnisse ebnen den Weg für ein ganzheitliches Verständnis der Wasserbewegung durch den Wildbachkorridor und tragen zu genauen Modellvorhersagen unter verschiedenen hydrologischen Bedingungen bei.

Endowed with the essences of flowers,
Eight precious minerals does he eat.
Astride dragons, he hides within the torrent,
Flowing onwards, the sea-god Ruo to meet.
Indeed he is a Transcendent of the waters:
"Lord of the River" is his name, complete.

– Guo Pu, presentation of Hebo, the Yellow River God

Die approbierte gedruckte Originalversion dieser Dissertation ist an der TU Wien Bibliothek verfügbar.
The approved original version of this doctoral thesis is available in print at TU Wien Bibliothek.
TU Bibliothek WIEN Your knowledge hub

other studies also highlighted that streamwater can flow vertically through the streambed in pool-and-riffle sections (Bencala, 1983) and that it can also mix laterally with the adjacent groundwater (Triska et al., 1989) before returning into the stream channel. This process goes under the name of hyporheic exchange, where the hyporheic zone can thus be defined as the saturated area that is physically influenced by the water exchange between the stream channel and the adjacent groundwater (Triska et al., 1989; White, 1993; Cardenas and Wilson, 2007). While the occurrence of the hyporheic zone as a buffer area between the streamwater and the groundwater was already well recognized by ecologists and biologists before the 1960s, it was fully acknowledged in stream hydrology only a few decades later (J-NABS, special issue 1993). This finding changed dramatically the way stream hydrologists viewed rivers, which from that moment on were not seen as distinct and separate units from the catchment, but rather as part of a much larger continuum comprising stream channels, together with fluvial deposits, riparian zones, and floodplains: the stream corridor (National Research Council, 2002).

The conjoint action of dead-zones, in-stream eddies, and hyporheic exchange on the streamwater transport within the stream corridor goes under the name of "transient storage process" and it can thus be seen as the fourth process governing the movement of water in river networks together with advection, dispersion and dilution (Gooseff et al., 2008). Being able to understand and model the mechanisms governing the transient storage in streams not only allows one to predict the transport of water downstream, but also improves the understanding of the processes governing water quality in river networks. Transient storage processes increase the residence time of solutes and pollutants in the stream channel, thus enhancing oxygen distribution, nutrient cycling, and contaminant removal (Vaux, 1962; Smith, 2005; Harvey & Gooseff, 2015; Krause et al., 2017). In particular, the hyporheic zone is naturally a buffer area between the stream water and the groundwater. Thus, the hyporheic zone exhibits slower flow velocities in comparison to surface flow, and faster velocities when compared to groundwater (Krause et al., 2011). The hyporheic zone also displays temperature and chemical gradients between streamflow and groundwater (Triska et al., 1989a, 1989b; Brunke and Gonser, 1997; Datry & Larned, 2008). These peculiar physical and chemical properties make the hyporheic zone a fundamental ecotone for riverine biology, leading to a rich distribution of various riverine microorganisms such as bacteria, benthic autotrophs, and nest-building vertebrates (Cummins 1980; Boulton et al., 2010).

Despite the importance of transient storage processes on both controlling water transport and its quality in stream channels, the current state of the art is unable to fully capture the spatio-temporal variability of the drivers regulating it. This inconsistent understanding of the underlying mechanisms controlling water movement in stream channels is the consequence of three major issues.

First, a common approach in the design of fieldwork experiments consists in assuming a certain process to be predominant compared to the others. As a result, there are several studies specifically focusing on hyporheic transport (Wondzell 2006; Fabian et al., 2011; Rathore et al., 2021), or on in-stream dead-zones (Davis et al., 2000; Weitbrecht, 2004; Gooseff et al., 2005). This research design does not allow capturing the conjoint action of different mechanisms participating in the

Die approbierte gedruckte Originalversion dieser Dissertation ist an der TU Wien Bibliothek verfügbar.
The approved original version of this doctoral thesis is available in print at TU Wien Bibliothek.
TU Bibliothek WIEN Your knowledge hub

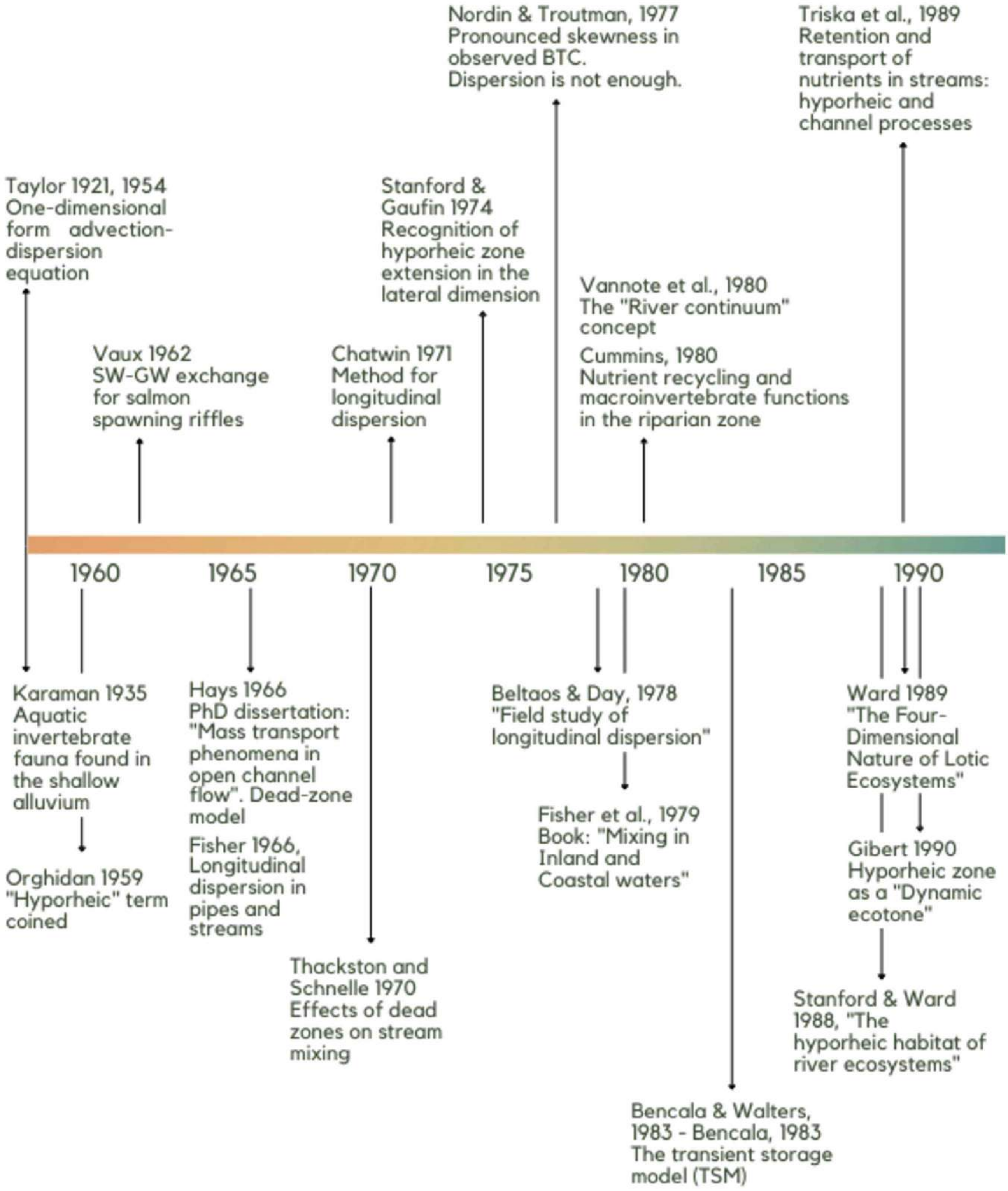
Nordin & Troutman, 1977
Pronounced skewness in observed BTC.
Dispersion is not enough.
Triska et al., 1989
Retention and transport of nutrients in streams: hyporheic and channel processes
Taylor 1921, 1954
One-dimensional form advection-dispersion equation
Stanford & Gaufin 1974
Recognition of hyporheic zone extension in the lateral dimension
Vannote et al., 1980
The "River continuum" concept
Vaux 1962
SW-GW exchange for salmon spawning riffles
Chatwin 1971
Method for longitudinal dispersion
Cummins, 1980
Nutrient recycling and macroinvertebrate functions in the riparian zone
1960
1965
1970
1975
1980
1985
1990
Karaman 1935
Aquatic invertebrate fauna found in the shallow alluvium
Orghidan 1959
"Hyporheic" term coined
Hays 1966
PhD dissertation: "Mass transport phenomena in open channel flow". Dead-zone model
Fisher 1966,
Longitudinal dispersion in pipes and streams
Thackston and Schnelle 1970
Effects of dead zones on stream mixing
Beltaos & Day, 1978
"Field study of longitudinal dispersion"
Fisher et al., 1979
Book: "Mixing in Inland and Coastal waters"
Bencala & Walters, 1983 - Bencala, 1983
The transient storage model (TSM)
Ward 1989
"The Four-Dimensional Nature of Lotic Ecosystems"
Gibert 1990
Hyporheic zone as a "Dynamic ecotone"
Stanford & Ward 1988, "The hyporheic habitat of river ecosystems"

Figure I. A timeline of significant publications contributing to increasing the understanding of water movement in river networks, streamwater-groundwater (SW-GW) exchange and the significance of the hyporheic zone (HZ).

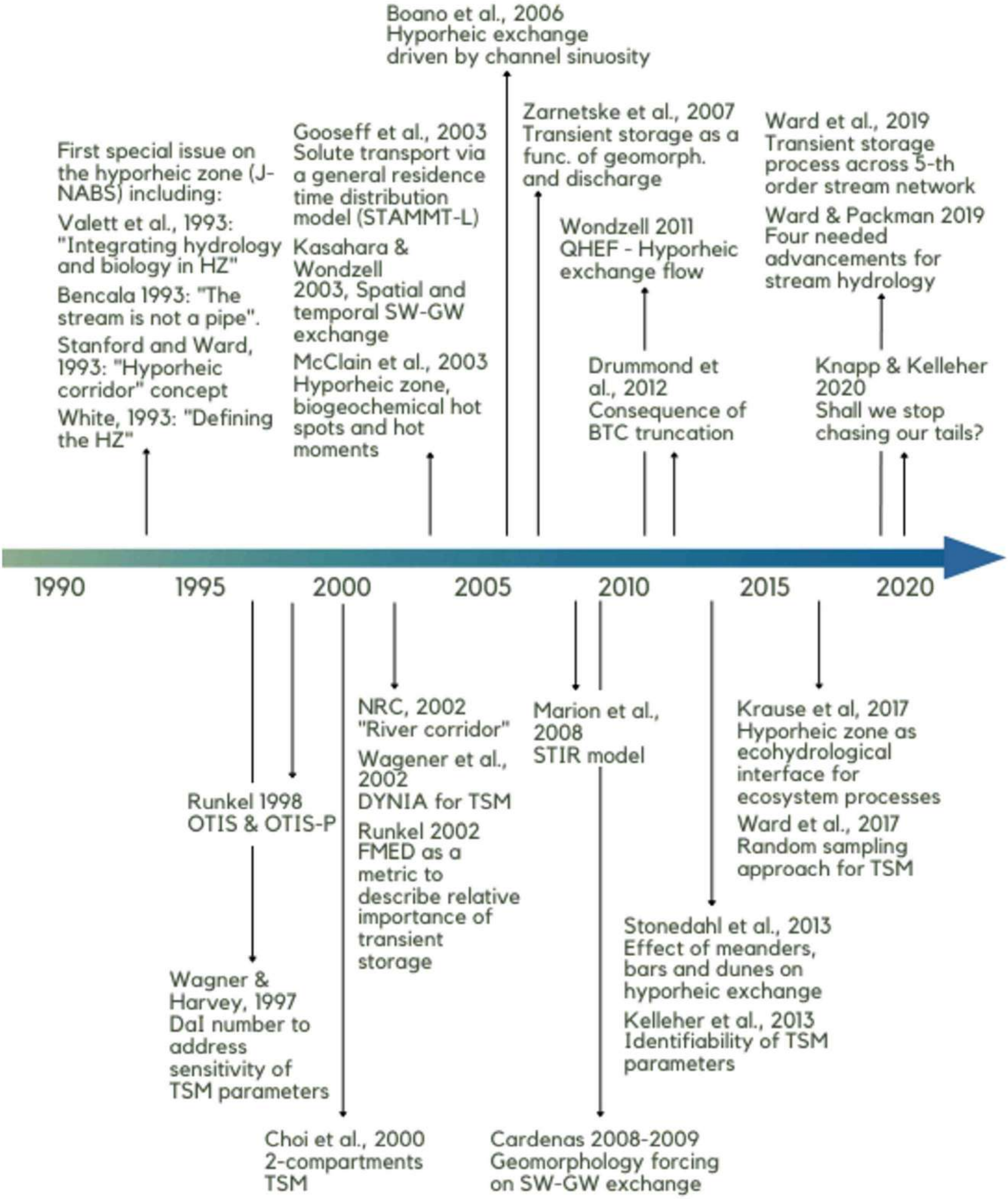
Boano et al., 2006
Hyporheic exchange driven by channel sinuosity
First special issue on the hyporheic zone (J-NABS) including:
Valett et al., 1993: "Integrating hydrology and biology in HZ"
Bencala 1993: "The stream is not a pipe".
Stanford and Ward, 1993: "Hyporheic corridor" concept
White, 1993: "Defining the HZ"
Gooseff et al., 2003
Solute transport via a general residence time distribution model (STAMMT-L)
Kasahara & Wondzell 2003, Spatial and temporal SW-GW exchange
McClain et al., 2003
Hyporheic zone, biogeochemical hot spots and hot moments
Zarnetske et al., 2007
Transient storage as a func. of geomorph. and discharge
Wondzell 2011
QHEF - Hyporheic exchange flow
Drummond et al., 2012
Consequence of BTC truncation
Ward et al., 2019
Transient storage process across 5-th order stream network
Ward & Packman 2019
Four needed advancements for stream hydrology
Knapp & Kelleher 2020
Shall we stop chasing our tails?
1990
1995
2000
2005
2010
2015
2020
Runkel 1998
OTIS & OTIS-P
Wagner & Harvey, 1997
DaI number to address sensitivity of TSM parameters
Choi et al., 2000
2-compartments TSM
NRC, 2002
"River corridor"
Wagener et al., 2002
DYNIA for TSM
Runkel 2002
FMED as a metric to describe relative importance of transient storage
Marion et al., 2008
STIR model
Cardenas 2008-2009
Geomorphology forcing on SW-GW exchange
Stonedahl et al., 2013
Effect of meanders, bars and dunes on hyporheic exchange
Kelleher et al., 2013
Identifiability of TSM parameters
Krause et al, 2017
Hyporheic zone as ecohydrological interface for ecosystem processes
Ward et al., 2017
Random sampling approach for TSM

Figure I. Continuation.

the identifiability of TSM parameters is independent of discharge conditions, and ii) higher discharge stages have a lower influence on both hyporheic exchange and in-stream transient storage compared to lower discharge conditions. The outcomes of this study provide a clear process interpretation of water movement at the study site. Also, this work offers a promising approach for future research addressing transient storage processes via different and more complex TSM formulations or over more complex stream morphologies.

To test the hypothesis of this thesis, an exhaustive fieldwork campaign has been conducted from 2018 to 2021 to monitor groundwater table dynamics and solute transport along a 55 m stream reach in the Weierbach catchment. The Weierbach catchment is a 0.42 km^2 experimental site located in the North-West of the Gran Duchy of Luxembourg (49°49'38''N, 5°47'44''E). The climate is semi-oceanic with an annual precipitation depth equal to 958.32 mm (2009-2019, Hissler et al., 2020). The catchment is forested and dominated by a combination of *Fagus sylvatica* (European beech), *Quercus petraea* (Sessile oak), *Pseudotsuga menziesii* (Douglas fir) and *Picea abies* (Norway spruce) species.

The stream channel at the study site is unvegetated, characterized by a pool-and-riffle morphology and with an average slope of ≃6%. The reach was equipped with 36 wells and seven piezometers drilled via a portable rotative drilling system and a percussion hammer. The groundwater monitoring network was designed to investigate the groundwater dynamics in the stream channel and on the left and right stream banks. A total of 31 in-stream tracer injections were conducted from December 2018 to June 2021 via sodium chloride solutions covering both wet and dry hydrologic conditions.

Several studies have investigated runoff generation at the study site (Wrede et al., 2015; Glaser et al., 2016; Martínez-Carreras et al., 2016; Rodriguez & Klaus, 2019; Antonelli et al., 2020). The catchment hillslopes in the Weierbach catchment are characterized by a regolith layer with a relatively high hydraulic conductivity compared to the fractured bedrock layer beneath (Glaser et al., 2016, 2020). The subsurface structure does not promote shallow lateral flow toward the stream channel (Klaus & Jackson, 2018), and precipitation water percolates vertically toward the groundwater table in the fractured bedrock (Rodriguez & Klaus, 2019). Discharge is generated by both a fast and a slow response to precipitation events. The fast response of stream discharge to precipitation events largely consists of event water, both in dry and wet hydrologic conditions (Wrede et al., 2015). This has been interpreted as surface runoff of event-water over the saturated organic soil in the riparian zone toward the stream channel or by direct precipitation in the stream channel (Wrede et al., 2015; Glaser et al., 2016; Antonelli et al., 2020). The slow response occurs when the amount of water from precipitation events exceeds the storage capacity at the hillslope. When this happens, the groundwater is laterally redistributed over the fractured bedrock from the hillslopes toward the stream channel causing an increase in discharge and a double-peak behaviour in the hydrograph (Martínez-Carreras et al., 2016).

TU Bibliothek WIEN Your knowledge hub
Die approbierte gedruckte Originalversion dieser Dissertation ist an der TU Wien Bibliothek verfügbar.
The approved original version of this doctoral thesis is available in print at TU Wien Bibliothek.

And oft as swift-footed, goodly Achilles strove to make stand against him and
to learn if all the immortals that hold broad heaven were driving him in rout,
so often would the great flood of the heaven-fed Stream beat upon his shoulders from above;
and he would spring on high with his feet in vexation of spirit,
and the Stream was ever tiring his knees with its violent flow beneath,
and was snatching away the ground from under his feet.

– Homer, Iliad, Chapter 21.

Die approbierte gedruckte Originalversion dieser Dissertation ist an der TU Wien Bibliothek verfügbar.
The approved original version of this doctoral thesis is available in print at TU Wien Bibliothek.
TU WIEN Bibliothek Your knowledge hub

Chapter 1: Flow directions of stream-groundwater exchange in a headwater catchment during the hydrologic year

The present chapter corresponds to the following scientific publication:

Bonanno, E., Blöschl, G., and Klaus, J. (2021). Flow directions of stream-groundwater exchange in a headwater catchment during the hydrologic year. Hydrological Processes, 35(8), 1–18. https://doi.org/10.1002/hyp.14310

Graphical abstract

This work investigates the drivers of near-stream groundwater dynamics and stream-groundwater exchange across the hydrologic year. Our results stress the time-variant role of the position of the groundwater table with respect to the fractured bedrock, precipitation depth and intensity, upslope-footslope connectivity and streamwater level in determining the flow dynamics.

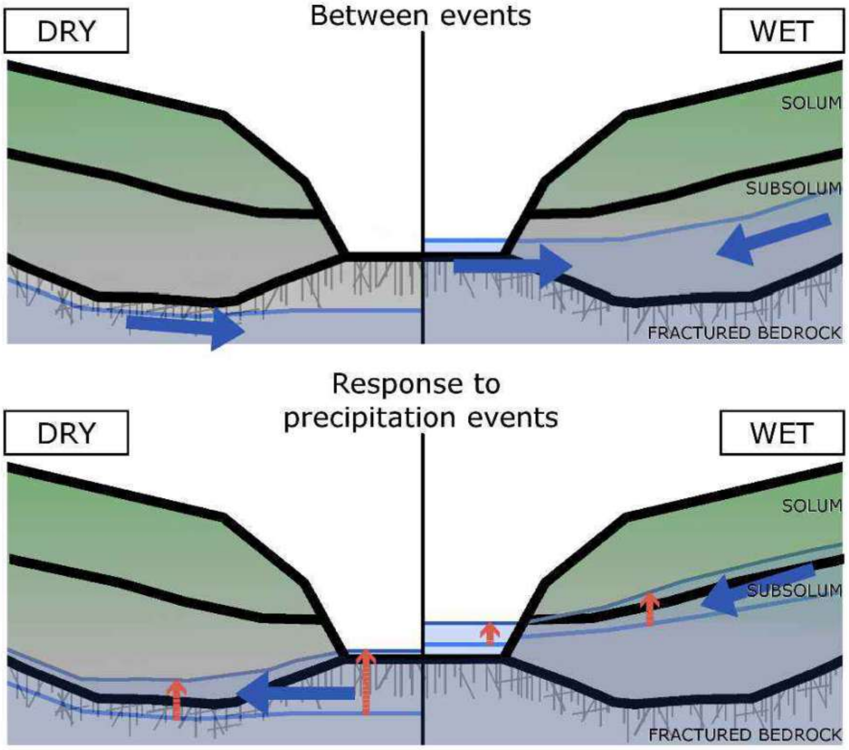
DRY
Between events
WET
SOLUM
SUBSOLUM
FRACTURED BEDROCK
Response to
precipitation events
DRY
WET
SOLUM
SUBSOLUM
FRACTURED BEDROCK

Die approbierte gedruckte Originalversion dieser Dissertation ist an der TU Wien Bibliothek verfügbar.
The approved original version of this doctoral thesis is available in print at TU Wien Bibliothek.
TU WIEN Bibliothek Your knowledge hub

precipitation characteristics (Dhakal & Sullivan, 2014; Fannin et al., 2000), and antecedent conditions (Detty & McGuire, 2010a). However, compared to hillslopes, near-stream groundwater dynamics are also affected by the local accumulation of finer soil material in the riparian zones (Rinderer et al., 2017; Scheliga et al., 2018), streamwater infiltration (Dudley-Southern & Binley, 2015), and changes in gradients due to streambed morphology (e.g., pool-and-riffle sections, Buffington & Tonina, 2009). Studies investigating the near-stream and hillslope groundwater also highlighted the higher degree of variability of groundwater flow direction in the near-stream domain compared to upslope locations (Burt et al., 2002; Hinton et al., 1993; Rodhe & Seibert, 2011; Von Freyberg et al., 2014).

Despite groundwater dynamics and flow direction being recognized as strongly variable in the near-stream domain, many studies have focussed on the spatiotemporal differences between near-stream and upslope groundwater and assumed that a small number of wells close to the stream are representative of the near-stream domain. As a result, data and observations in the stream corridor are often fragmented (Burt et al., 2002; Rodhe & Seibert, 2011) and do not provide a complete description of the processes controlling streamwater-groundwater exchange (Ward & Packman, 2019). One limitation of most experimental studies that may contribute to the diversity of results is the design of the observation networks. Most studies relied on near-stream well networks on only one side of the stream channel (Burt et al., 2002; Heeren et al., 2014) or on a low temporal measurement resolution (monthly or biweekly) (Vidon & Hill, 2004; Vidon & Smith, 2007). While important understanding has been obtained from these studies, such measurement designs do not capture the high frequency evolution of near-stream groundwater level and flow directions. Another limitation amongst studies is the lack of observations across the full range of hydrologic conditions. Although precipitation characteristics and hydrologic conditions play a major role in groundwater dynamics, past studies mostly focussed on shorter periods at baseflow conditions (Ward, 2016) or on a limited number of precipitation events (Dudley-Southern & Binley, 2015; Heeren et al., 2014; van Meerveld et al., 2015; Vidon, 2012; Voltz et al., 2013). Consequently, we lack long-term observations in the near-stream domain across different flow conditions. This hampers our ability to address spatiotemporal changes in groundwater flowpaths in the stream corridor. Responding to calls from Ward and Packman (2019) on the need to decipher the time-variant role of the drivers controlling the streamwater-groundwater exchange, we investigated a stream corridor with a network of 36 wells and 7 piezometers over a period of 18 months, to address the following research questions:

1. How and why does the near-stream groundwater table dynamic vary in different hydrologic conditions?
2. How and why does the near-stream groundwater flow direction change in different hydrologic conditions?

1.3 Study site

The study site is a 55 m-long corridor along a headwater stream in Luxembourg (49°49'38''N, 5°47'44''E) downstream of the Weierbach experimental catchment (Hissler et al., 2021; Figure A3). The geology consists of Devonian slate and quartzite bedrock, covered by Pleistocene periglacial slope deposits. The climate is semi-oceanic with precipitation rather uniformly distributed throughout the year. Higher evapotranspiration rates in summer induce streamflow seasonality with its lowest values (potential no-flow) between July and October. Streamflow generation is controlled by the interplay of surface flowpaths from abundant riparian wetlands (Antonelli et al., 2020; Glaser et al., 2016; Glaser et al., 2020) and deeper flowpaths with longer travel times (Rodriguez et al., 2021; Rodriguez & Klaus, 2019).

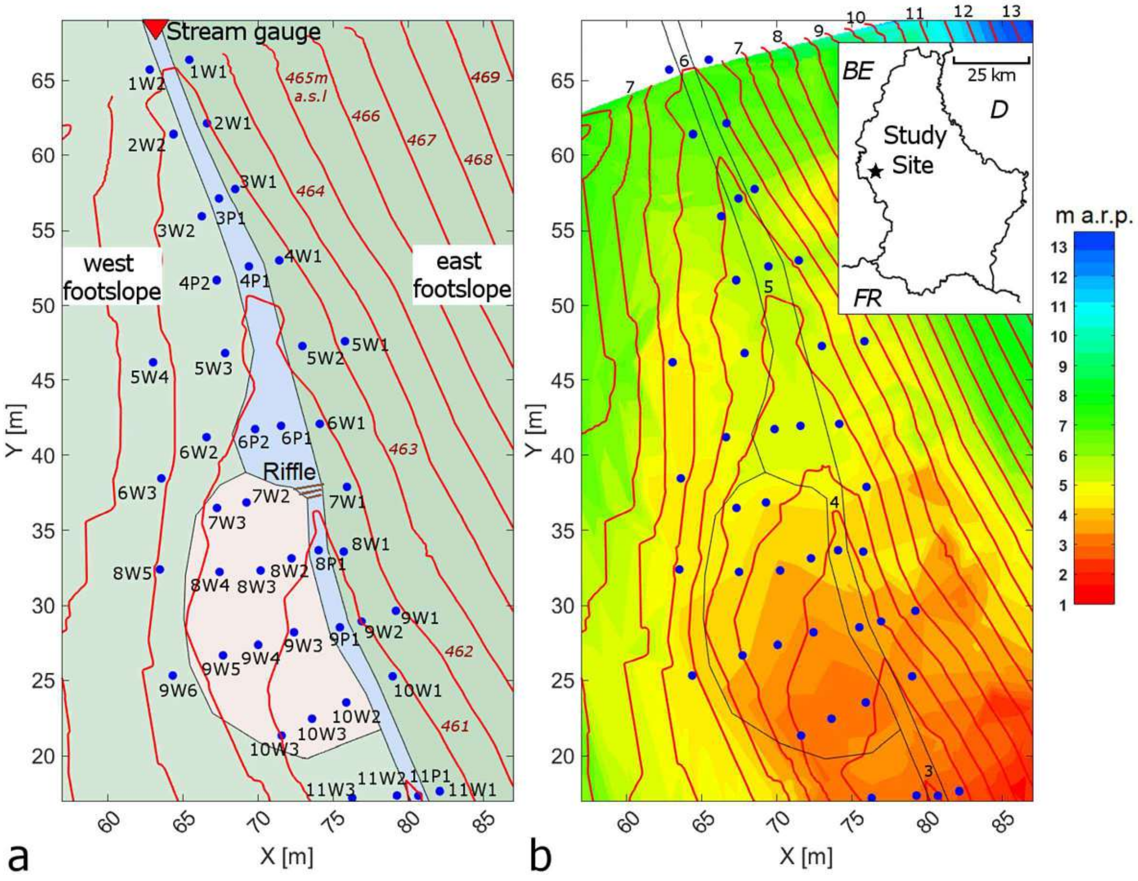
Stream gauge
west footslope
east footslope
Riffle
465m a.s.l
461
462
463
464
466
467
468
469
1W1
1W2
2W1
2W2
3W1
3W2
3P1
4W1
4P1
4P2
5W1
5W2
5W3
5W4
6W1
6W2
6W3
6P1
6P2
7W1
7W2
7W3
8W1
8W2
8W3
8W4
8W5
8P1
9W1
9W2
9W3
9W4
9W5
9W6
9P1
10W1
10W2
10W3
11W1
11W2
11W3
11P1
Y [m]
X [m]
a
b
BE
D
FR
25 km
Study Site
m a.r.p.
1
2
3
4
5
6
7
8
9
10
11
12
13

Figure 1.1. (a) Study reach, location and name of the wells/piezometers (blue circles) with stream channel (blue), riparian wetland (ochre), hillslopes (green) and contour lines (m a.s.l.) (red); (b) bedrock surface topography (colours) from electrical resistivity tomography (ERT) survey and red contour lines showing surface topography, both expressed in metres above reference plane (m a.r.p.). The flow direction of the stream is from top to bottom on the map.

The stream channel is unvegetated and consists of deposited colluvial material and fragmented schists (up to 50 cm depth) with underlying fractured slate bedrock that sporadically forms the streambed. The average channel slope is ≃6% and a 50 cm step riffle sits between wells 7W1 and 7W2 (Y = 36 m, Figure 1.1(a)). The regolith (i.e., the unconsolidated material deriving from the degeneration of the bedrock in situ, Merrill (1906)) in the Weierbach catchment can be subdivided into solum and subsolum (Gourdol et al., 2021; Juilleret et al., 2016; Moragues-Quiroga et al., 2017). The solum, that is, the upper part of the regolith where pedogenic processes are dominant and biota play an important role consists of an O horizon (highly decomposed organic material) above a silty clay Ah Horizon and a silty clay loam B Cambic horizon (Juilleret et al., 2016;

Die approbierte gedruckte Originalversion dieser Dissertation ist an der TU Wien Bibliothek verfügbar.
The approved original version of this doctoral thesis is available in print at TU Wien Bibliothek.
TU Bibliothek WIEN Your knowledge hub

Moragues-Quiroga et al., 2017). The solum is characterised by a loam texture with high porosity (from 61% to 45%, Glaser et al., 2016; Gourdol et al., 2021) and low volumetric content of rock fragments (from 13% to 27%, Moragues-Quiroga et al., 2017; Gourdol et al., 2021). The subsolum, that is, the lower part of the regolith where the original rock structure or fabric of the bedrock is preserved consists of loam 2Cg1 and sandy loam 2Cg2 horizons above a 3CR saprolithic horizon (Juilleret et al., 2016; Moragues-Quiroga et al., 2017). It is characterised by sandy-loam texture (Gourdol et al., 2021) with abundant rock fragments (from 25% to more than 80%, Gourdol et al., 2021) and decreasing porosity (from 30% to 15%, Glaser et al., 2016). The fractured bedrock below the subsolum consists of Devonian slate and phyllites fractured bedrock (3R horizon, paralithic material; Juilleret et al., 2016; Moragues-Quiroga et al., 2017) where porosity decreases with depth (from 15% to 10%, Glaser et al., 2016) and the volumetric content of rock fragments increases up to 90% (Gourdol et al., 2021). The drastic decrease of porosity with depth is also reflected by a decrease in storage capacity observed in the field investigations, where the volumetric water content in the solum was almost double that in the subsolum during drainage conditions (Martínez-Carreras et al., 2016). The properties of the solum, subsolum, and fractured bedrock are summarized in Table 1. A riparian wetland (Figure 1.1(a)) is located beside the stream channel. Such wetlands account for 1.2% of the Weierbach catchment (Antonelli et al., 2020) and consist of shallow organic clay-loamy soil over the fractured bedrock (Leptosols, Glaser et al., 2016).

Table 1.1. Subsurface layers in the study site and their properties.

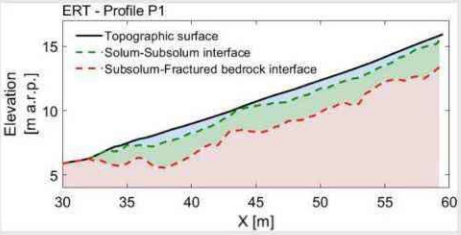

	Layer		
Properties	Solum	Subsolum	Fractured bedrock
Rock fragments volumetric content	13%–27%[a]	25% to more than 80%[c]	90%–100%[c]
Porosity	45%–61%[b]	15%–30%[b]	10%–15%[b]
Composition	Loam texture[c]	Sandy-loam texture with abundant rock fragments[c]	Devonian slate and phyllites fractured bedrock (paralithic layer)[c]

[a] Moragues-Quiroga et al. (2017).
[b] Glaser et al. (2016).
[c] Gourdol et al. (2021).

1.4 Methods

1.4.1 Observation of the groundwater table

We installed 36 wells and seven piezometers (Figure 1.1(a)). We placed the piezometers directly into stream channel boreholes drilled with a percussion hammer (Cobra TT, Eijkelkamp, Netherlands). Wells were drilled with a portable drilling system (Gabrielli & McDonnell, 2012) down to fresh bedrock and cased the wells with a 4 cm diameter PVC pipe screened at the bottom (Table B). We filled the space between the borehole and the pipe with gravel and sealed the borehole with bentonite at the top. We observed the water level every 15 min at 22 of the 36 wells with a water level sensor (Orpheus Mini, OTT, Kempten, Germany, resolution of 1 mm and accuracy of ±0.05% FS) and approximately biweekly in all wells and piezometers via manual measurements. Measurements started in July 2018 and continued until February 2020. Inflow into the study section was measured using a steam gauge (Figure 1.1(a)) with a pressure transducer (ISCO 4120 Flow Logger). Discharge was derived from a water level–discharge rating curve that

dry days). We correlated the spatial differences in the average groundwater response time and increase per well with the regolith depth above the fractured bedrock and with the distance from and the elevation above the streambed using the Spearman rank correlation coefficient (Rs). Significance was evaluated with the Mann–Whitney test (significance level: p-value < 0.05). We computed groundwater flow directions by assuming that they were equal to the slope of a planar groundwater table determined by three adjacent wells. We quantified the direction by angle α (degrees) on the *xy* plane (cf. Rodhe & Seibert, 2011). The stream is oriented with -72° on the *xy* plane (cf. Figure 1.2(b)). α-values pointing towards the stream channel indicate that the stream is gaining conditions, whereas α pointing away from the channel suggests losing conditions. The subsurface groundwater flow direction was calculated every 15 min. For the wells equipped with continuous water level loggers (Figure 1.2(a), 29 triangles), and for all wells every 2 weeks (Figure 1.2(b), 65 triangles). For every triangle, we also derived the direction of the fractured bedrock fall line (defined as the direction on the *xy* plane [degrees] of the slope of the fractured bedrock surface) and the direction of the surface topography fall line (defined as the direction on the *xy* plane [degrees] of the slope of the topographic surface) using the same approach used for obtaining the direction of the groundwater table. Data analysis has been conducted with MATLAB R2020a (The Mathworks, Natick, MA).

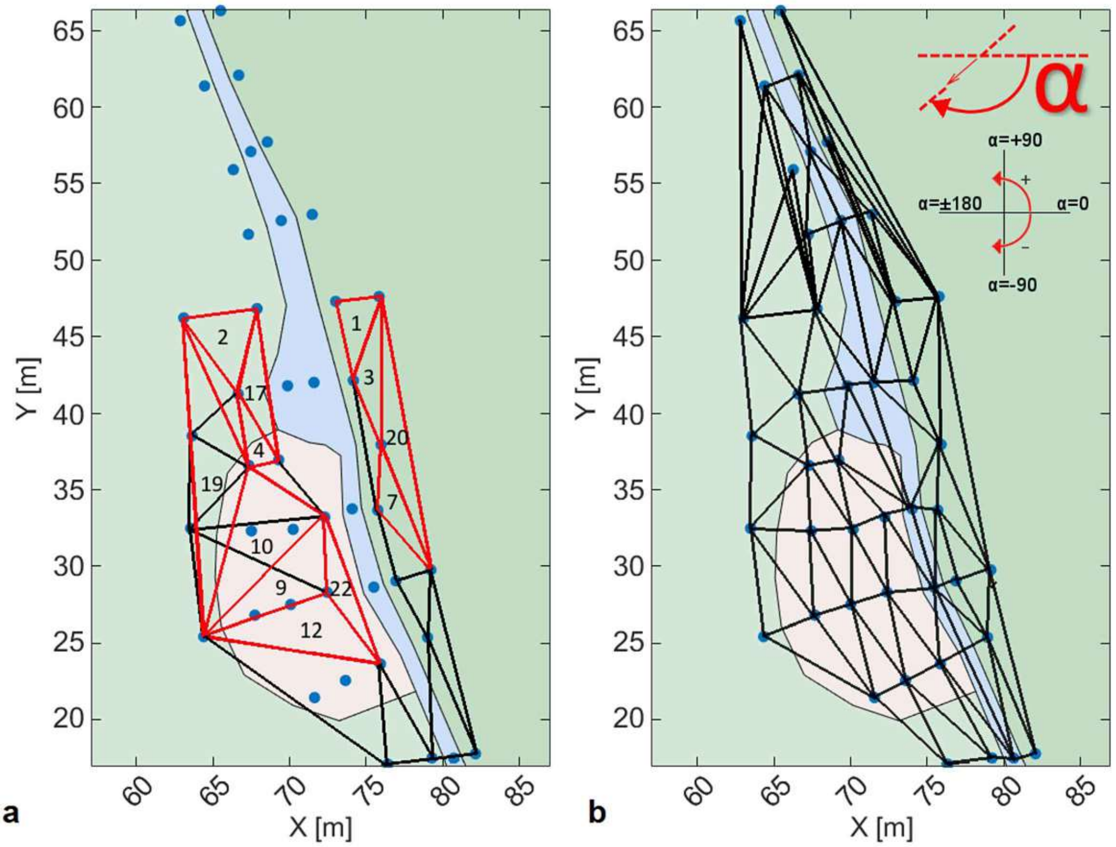

Figure 1.2. (a) Triangles for the calculation of the groundwater flow direction from wells with continuous measurements, and (b) from manual groundwater monitoring; the direction of angle **α** is reported at the top of the panel. Example triangles are indicated with a red perimeter and their number.

Die approbierte gedruckte Originalversion dieser Dissertation ist an der TU Wien Bibliothek verfügbar.
The approved original version of this doctoral thesis is available in print at TU Wien Bibliothek.
TU WIEN Bibliothek Your knowledge hub

1.5 Results

1.5.1 Groundwater and streamflow dynamics

Streamflow varied widely (Figure 1.3, arithmetic mean of 6.5 l/s, median of 1.7 l/s, interquartile range of 9.1 l/s, St.Dev. of 11.52 l/s), with extended no-flow periods during summer (no discharge for a total of 194 days during the study period), persistent streamflow during winter and spring, and variable event responses. We defined three different hydrologic conditions (dry, intermediate, wet) based on streamflow and groundwater levels (shown as grey shades, Figure 1.3; details in Table 1.2) to classify groundwater behaviour.

We defined wet conditions when discharge Q exceeded 0 l/s for 14 consecutive days regardless of the groundwater elevation in the wells. Intermediate conditions were only defined when they immediately occurred before or after the wet conditions. Intermediate conditions were specified when $Q = 0$ or $Q > 0$ l/s lasted less of 14 consecutive days, and when the monitored groundwater in at least 17 (75%) of the wells was above the subsolum-fractured bedrock. Dry conditions were specified when $Q = 0$ or $Q > 0$ l/s lasted less than 14 consecutive days and when the monitored groundwater in less than 17 (75%) of the wells was above the subsolum-fractured bedrock.

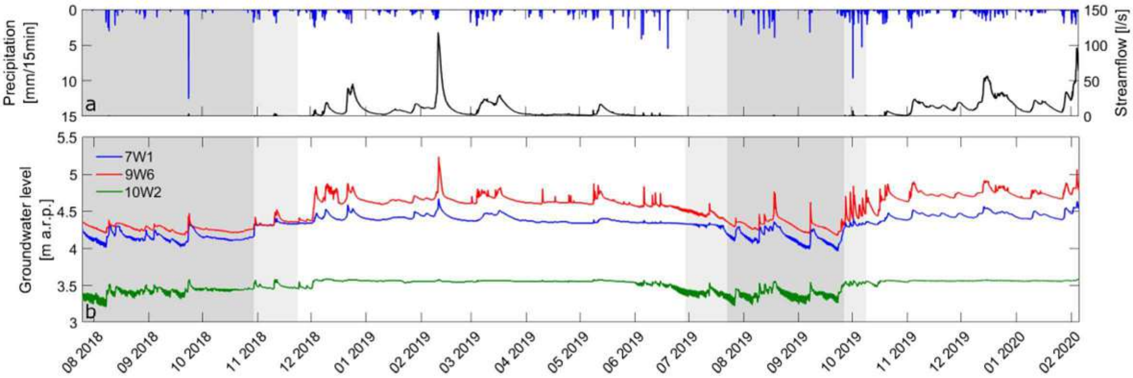

Figure 1.3. (a) Precipitation (blue) and streamflow (black); (b) groundwater level for a selection of wells in the east footslope (7W1, blue), west footslope (9W6, red) and riparian wetland (10W2, green). Dark grey areas indicate dry hydrologic conditions; light grey, intermediate hydrologic conditions; and white areas, wet hydrologic conditions.

Table 1.2. Periods of dry-intermediate-wet conditions and their duration, fraction of time with streamflow, total number of precipitation events, total depth of precipitation and rainfall characteristics (depth per event, inter-arrival time, duration).

Period	Hydrologic classification	Fraction of time with streamflow (%)	Number of precipitation events	Total depth of precipitation (mm)	Precipitation depth per event (mm)		Precipitation inter-arrival time (days)		Duration of precipitation events (h)	
					Mean	St.dev.	Mean	St.dev	Mean	St.dev
25/07/2018–30/10/2018	Dry	4.97	18	111.8	6.21	9.43	4.54	5.41	5.01	6.92
30/10/2018–24/11/2018	Intermediate	26.05	12	57.3	4.77	6.25	1.99	2.52	5.39	3.52
24/11/2018–29/06/2019	Wet	100	94	584.6	6.22	9.07	2.26	4.51	7.1	8.28
29/06/2019–23/07/2019	Intermediate	36.18	0	0	//	//	//	//	//	//
23/07/2019–24/09/2019	Dry	4.71	19	102.5	5.39	5.02	3.00	5.21	4.79	4.78
24/09/2019–08/10/2019	Intermediate	46.87	17	113.2	6.66	7.23	0.45	0.49	6.66	6.57
08/10/2019–05/02/2020	Wet	100	71	523.7	7.37	7.78	1.29	1.88	9.29	7.71

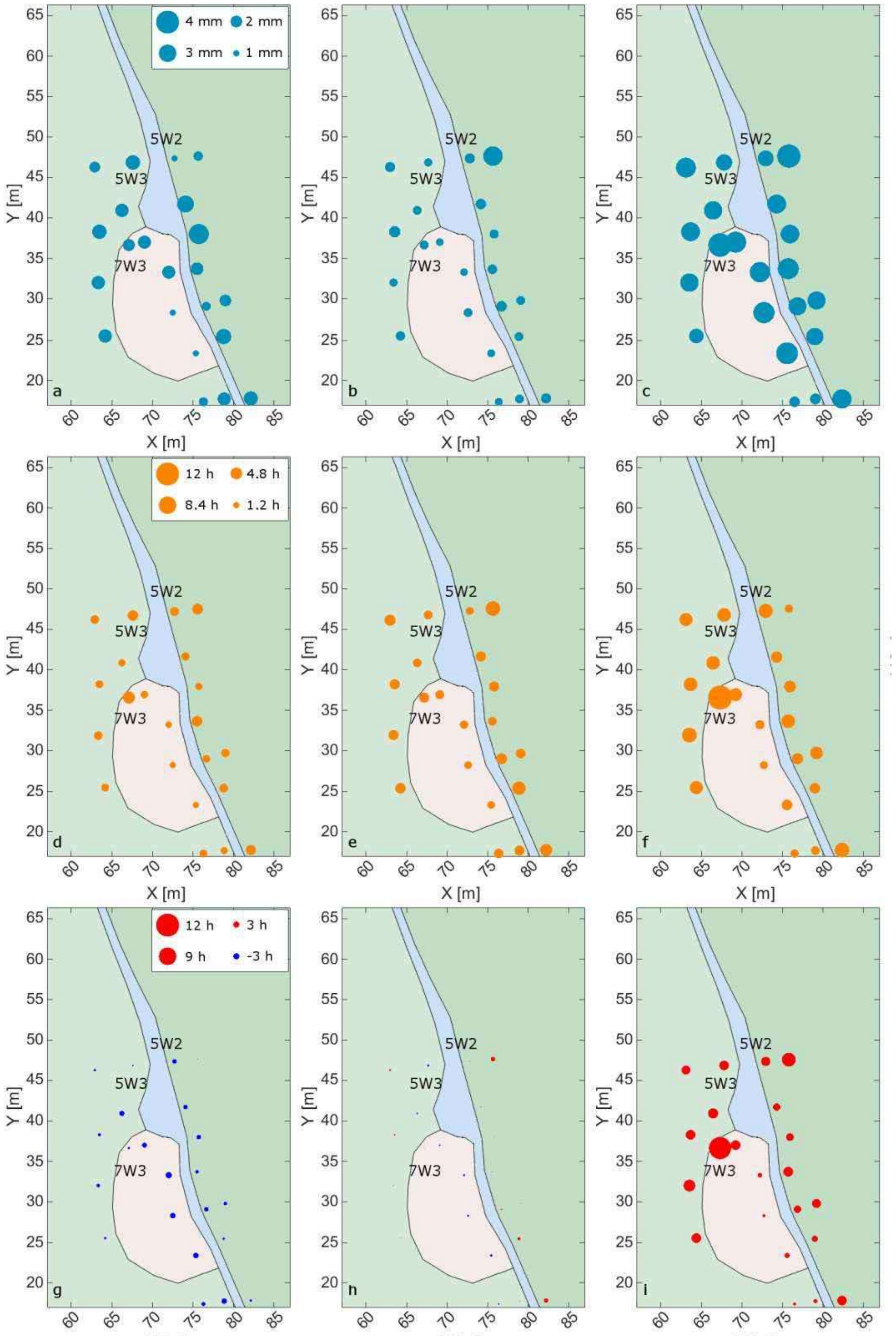
4 mm
2 mm
3 mm
1 mm
12 h
4.8 h
8.4 h
1.2 h
12 h
3 h
9 h
-3 h
5W2
5W3
7W3
a
b
c
d
e
f
g
h
i
Y [m]
X [m]
65
60
55
50
45
40
35
30
25
20
60
65
70
75
80
85

Figure 1.4. Groundwater response to precipitation events. Average magnitude of the minimum precipitation depth needed to trigger a groundwater level response of at least 1 cm for each well in dry (a), intermediate (b), and wet (c) conditions; average lag time between the beginning of precipitation and groundwater level response of at least 1 cm for dry (d), intermediate (e), and wet (f) conditions; average lag time between the beginning of a discharge increase (when present) and a groundwater level response of at least 1 cm for dry (g), intermediate (h), and wet (i) conditions. Negative numbers indicate a groundwater response earlier than the recorded discharge increase.

Die approbierte gedruckte Originalversion dieser Dissertation ist an der TU Wien Bibliothek verfügbar.
The approved original version of this doctoral thesis is available in print at TU Wien Bibliothek.
TU WIEN Bibliothek Your knowledge hub

Dry conditions (dark grey shading, Figure 1.3, 28.7% of the observation period) (Table 1.2) had no-flow for 95.3% of the time. The average streamflow in this period was 0.01 l/s. Groundwater (Figure 1.3(b)) displayed flashy and short-lived increases after precipitation. The groundwater table in the east and west footslopes (wells 7W1 and 9W6, Figure 1.3(b)) showed larger increases and faster recessions than tables in the riparian wetland (well 10W2, Figure 1.3(b)). During intermediate conditions (light grey shading, Figure 1.3, 11.0% of the observation period, Table 1.2), precipitation occurred more frequently and with higher amounts; no-flow persisted for 67.4% of the time (Table 1.2) and average streamflow was 0.12 l/s. During wet conditions (white shading, Figure 1.3), which covered 60.3% of the observation period (Table 1.2), streamflow was persistent (average discharge was 10.8 l/s with a maximum of 118 l/s).

To quantify the drivers of groundwater dynamics, we analysed the average response time and increase after precipitation events for groundwater and streamflow (Figure 1.4). During dry conditions, a groundwater response was triggered in all wells by small precipitation depths (<3 mm for 21 of the 22 wells; median = 2.2 mm, min = 1 mm, max = 3.5 mm, Figure 1.4(a)). This groundwater rise occurred a few hours after the onset of precipitation (<3 h, for 17 of the 22 wells; median = 2.48 h, min = 1.21 h, max = 5.15 h, Figure 1.4(d)). If streamflow was generated following precipitation, it appeared several hours after the rise of the groundwater table (between 0.25 and 2.95 h; median = 1.75 h, Figure 1.4(g)). During dry conditions and before precipitation events (Figure 1.5(a)), the groundwater table in the footslopes (e.g. wells 5W2, 5W3) was below the streambed elevation (Figure 1.5(d)) in the fractured bedrock (Figure 1.5(g)). The groundwater table in the riparian wetland (e.g. well 7W3) was above the subsolum-bedrock interface and – for some wells – above streambed elevation (Figure 1.5(d),(g)). In response to precipitation events, groundwater in the footslopes rose rapidly from the fractured bedrock into the subsolum – and in a few instances – above streambed elevation. After events, the groundwater level decreased rapidly towards the pre-event level.

During intermediate conditions, the minimum precipitation depth necessary for a groundwater response was <3 mm for 21 of the 22 wells (median = 1.5 mm, min = 1.3 mm, max = 3.37 mm, Figure 1.4(b)). Groundwater rise usually occurred less than 5 h after the beginning of a precipitation event for most wells (median = 3.56 h, min = 2.17 h, max = 6.53 h; Figure 1.4(e)). In response to precipitation, streamflow increased (or re-appeared) almost synchronously with the groundwater table (Figure 1.4(h)). During intermediate conditions, the groundwater table was above the fractured bedrock and rose within the subsolum layer after the events and decreased to the pre-event level within 2–3 days (Figure 1.5(h)). The groundwater in the riparian wetland was always above the streambed elevation before and after precipitation events, while the groundwater in the footslopes was mostly at the level of the streambed (Figure 1.5(e)).

During wet conditions, the groundwater table was always above streambed elevation (Figure 1.5(f)) and in the upper subsolum or the solum (Figure 1.5(i)). The groundwater table variation in the footslopes mirrored streamflow variations (Figure 1.2(a),(b)), while the groundwater table in the riparian wetland was more stable with less frequent and smaller peaks (Figure 1.2(b)). The precipitation depth necessary to trigger an increase in the groundwater level was highest in wet

Die approbierte gedruckte Originalversion dieser Dissertation ist an der TU Wien Bibliothek verfügbar.
The approved original version of this doctoral thesis is available in print at TU Wien Bibliothek.
TU Bibliothek WIEN Your knowledge hub

conditions (median = 3.24 mm, min = 1.81 mm, max = 4.1 mm, Figure 1.4(c)) and the groundwater response to precipitation events was more delayed compared to dry and intermediate conditions (median = 5.58 h, min = 2.35 h, max = 12.68 h Figure 1.4(f)). In contrast to dry and intermediate conditions, streamflow response occurred before groundwater response (median = 4.54 h, min = 1.26 h, max = 11.41 h, Figure 1.4(i)). In the riparian wetland, the groundwater table reached the surface in several wells (8.5%, 6.8%, 14.6%, and 50.3% of the time for wells 7W2, 7W3, 9W3, and 10W2, respectively). Some wells displayed artesian behaviour for extended periods of time (46.5% and 14.9% of the time for wells 7W3 and 10W2, respectively).

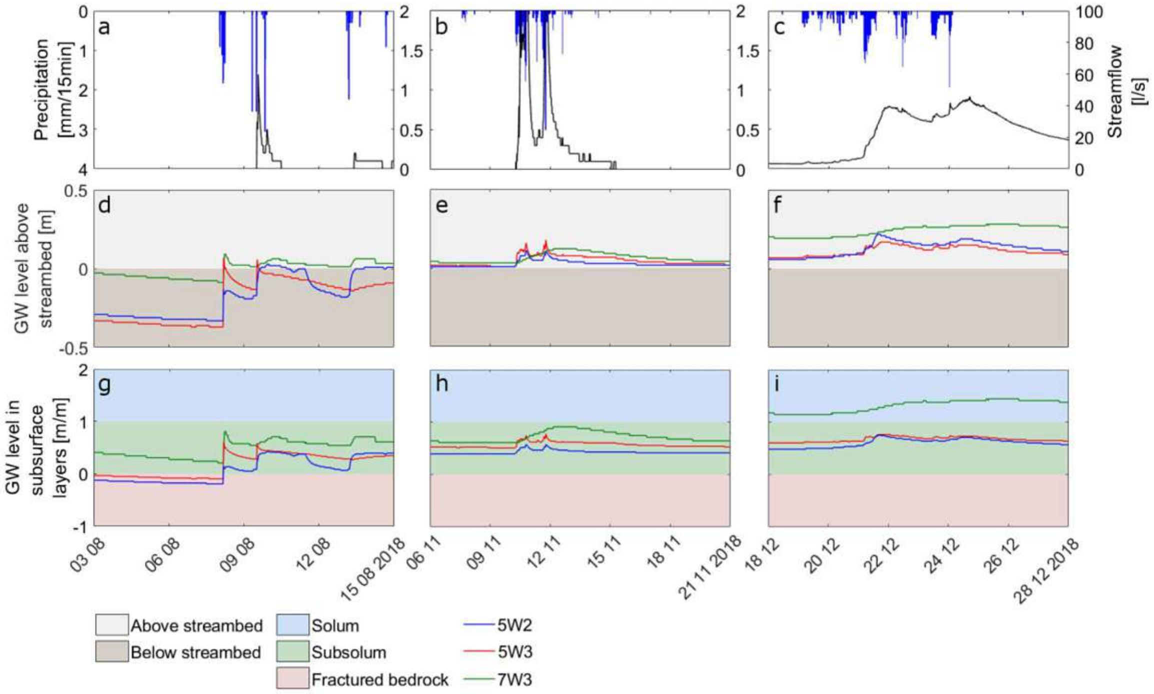

Figure 1.5. Event precipitation (blue) and streamflow (black) for selected events during dry (a), intermediate (b), and wet (c) conditions; groundwater level relative to the streambed elevation for the same three events during dry (d), intermediate (e) and wet (f) conditions; groundwater level relative to different subsurface layers for dry (g), intermediate (h), and wet (i) conditions. Wells 9W2, 11W3, and 7W3 are located respectively on the east footslope (blue line), west footslope (red line), and riparian wetland (green line), Figure 1.4.

We conducted a correlation analysis for every well to determine whether precipitation characteristics and initial groundwater table elevation drove temporal variability of groundwater dynamics in different hydrologic conditions (Figure 1.6 and Appendix C). The increase in the groundwater level was always positively correlated with precipitation depth (Figure 1.6(a)), and it was positively correlated with precipitation intensity for the whole study period and for intermediate and wet conditions (Figure 1.6(b)). The increase in the groundwater level was also negatively correlated with the initial groundwater level for most wells during the whole study period (Figure 1.6(d)). We found no significant correlation between groundwater increase and number of antecedent dry days (Figure 1.6(c)). The observed groundwater response time was always negatively correlated with precipitation intensity (Figure 1.6(f)) and the correlation was significant for the whole study period and for intermediate and wet conditions. For the whole study period, the groundwater response time was also significantly positively correlated with initial groundwater levels for most wells (Figure 1.6(h)). We found that only a few wells had a significant correlation between groundwater response time and precipitation depth or the number of antecedent dry days (Figure 1.6(e,g)).

We conducted a correlation analysis to determine whether the regolith thickness and distance from and elevation above the stream channel drove spatial variability in groundwater dynamics for different hydrologic conditions. During wet conditions, the average groundwater increase and response time were significantly positively correlated with regolith thickness above the fractured bedrock and elevation above and distance from the streambed. During dry conditions, the average groundwater increase and response time were respectively significantly correlated with elevation above the streambed and regolith thickness above the fractured bedrock (Appendix C).

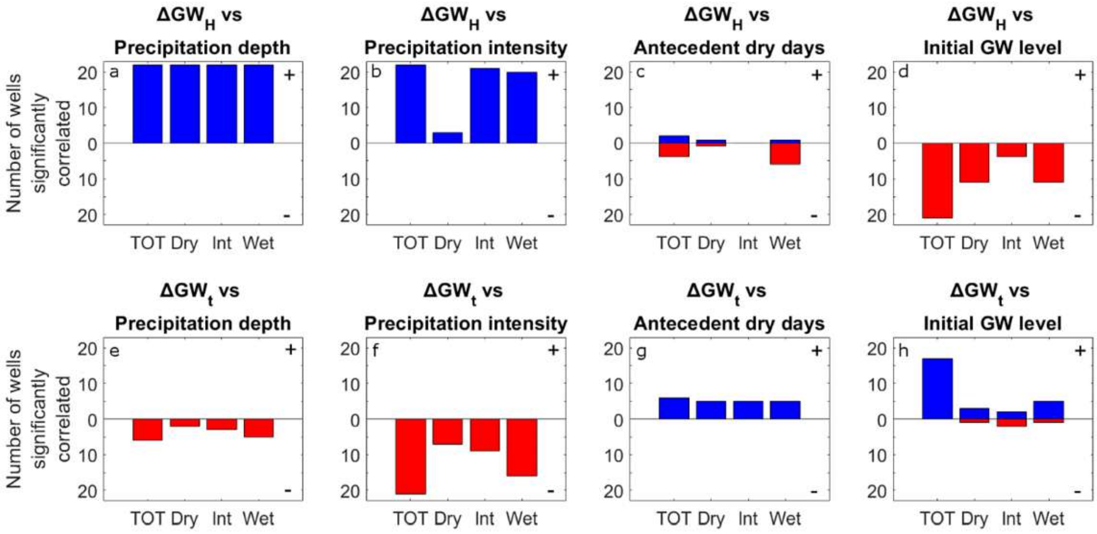

Figure 1.6. Histograms of the number of wells that have a significant positive (blue histogram) and significant negative (red histogram) Spearman relationship between the groundwater increase (ΔGW_H) and groundwater response time (ΔGW_t) for (a, e) precipitation depth, (b, f) precipitation intensity, (c, g) number of antecedent dry days, and (d, h) initial groundwater level. The results are reported for the entire observation period (TOT) and for dry, intermediate and wet conditions (intervals reported in Table 1.2).

1.5.2 Spatiotemporal dynamics of groundwater flow direction

α showed spatial patterns with clear differences between the east footslope, west footslope and the riparian wetland. The patterns are illustrated for two sets of 2 days using manual level measurements before and after precipitation events (Figure 1.7). The first example of 2 days relates to dry conditions (Figure 1.7(a),(c),(e)). Before the event (falling limb, 26 August 2019), α pointed towards the stream channel on the east footslope and towards the hillslope on the west footslope (Figure 1.7(e), red arrows). Observed groundwater levels were mostly below the streambed ($\text{median}_{GW\_wells} = 7.2$ cm and $\text{median}_{GW\_piezo} = 11$ cm below the streambed) with groundwater in the stream channel generally at the same level or below groundwater in the footslopes (e.g., the level differences between the piezometers 4P1 and the adjacent well 4W1 was $\Delta GW_{4P1\text{-}4W1} = -4.7$ cm). In the riparian wetland, α pointed towards the stream channel. The event on 7 September led to

Die approbierte gedruckte Originalversion dieser Dissertation ist an der TU Wien Bibliothek verfügbar.
The approved original version of this doctoral thesis is available in print at TU Wien Bibliothek.
TU Bibliothek Your knowledge hub WIEN

an increase in the groundwater level throughout the study reach ($\text{median}_{\text{GW\_wells}} = 1.1\,\text{cm}$, $\text{median}_{\text{GW\_piezo}} = 1.8\,\text{cm}$ below the streambed on 9 September 2019; Figure 1.7(a),(c),(e), blue arrows). As a result, groundwater in the streambed rose above the level of the adjacent groundwater in several sections (e.g., $\Delta\,\text{GW}_{\text{4P1-4W1}} = 15.3\,\text{cm}$) and α pointed towards the footslopes in some sections of the stream corridor (Figure 1.7(e)).

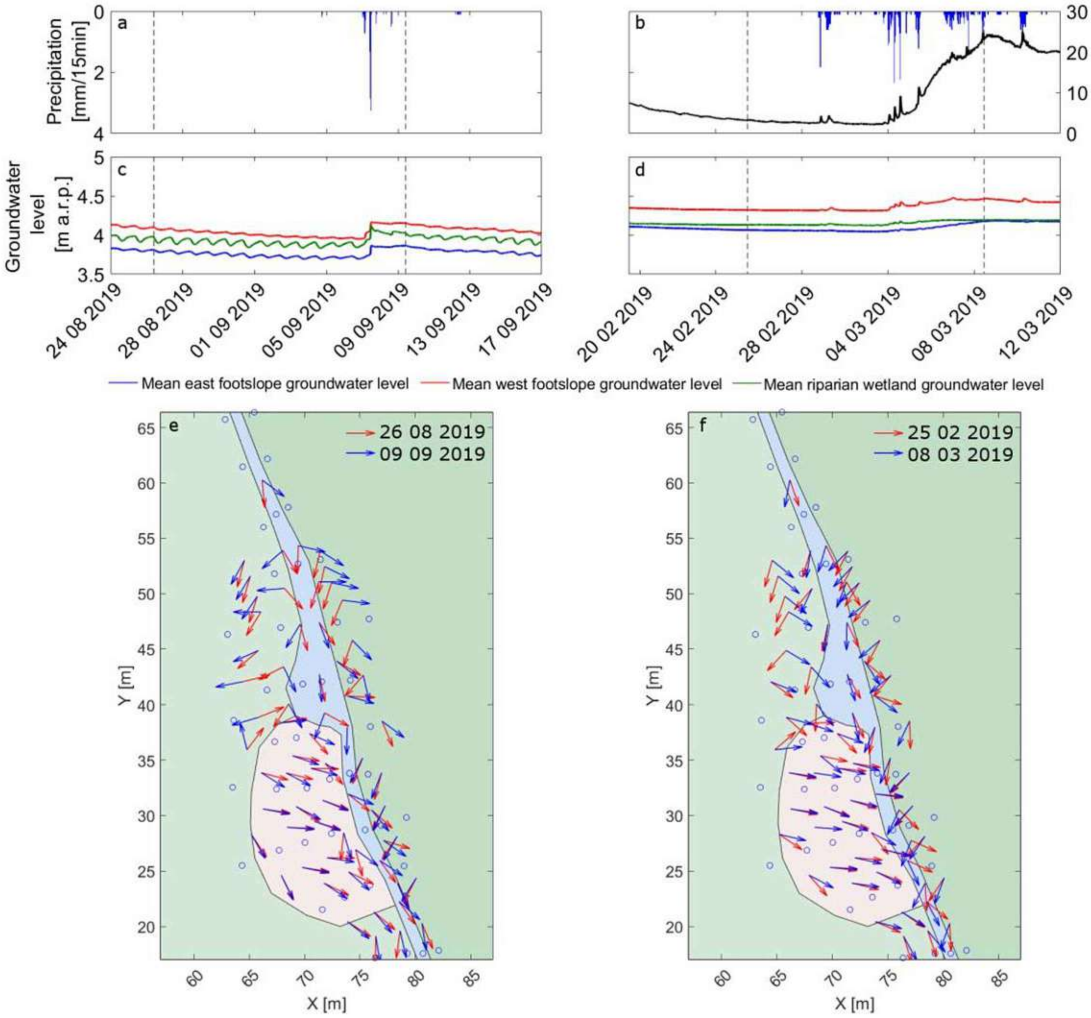

Figure 1.7. Precipitation and streamflow time series for (a) dry conditions and (b) wet conditions and groundwater levels on the east footslope (blue), the west footslope (red), and the riparian wetland (green). Bottom panels: Groundwater flow directions at the time of manual inspections for (e) dry and (f) wet conditions. The times of inspection are indicated as blackdotted lines in (a, b, c).

The second example relates to wet conditions (Figure 1.7(b),(d),(f)). Before the event (falling limb, 25 February 2019), the groundwater table was above the streambed elevation ($\text{median}_{\text{GW\_wells}} = 7.8\,\text{cm}$, $\text{median}_{\text{GW\_piezo}} = 3\,\text{cm}$ above the streambed in the wells). Yet, groundwater in some piezometers was above that of the adjacent wells (e.g., $\Delta\,\text{GW}_{\text{6P2-6W2}} = 3.5\,\text{cm}$), and at the same level or below the streamwater level (e.g., $\Delta\,\text{GW}_{\text{6P2-SW}} = -1\,\text{cm}$). α pointed towards the hillslope on the west footslope and in a few locations close to the stream channel on the east footslope (Figure 1.7(f), red arrows). However, α pointed towards the stream on the east footslope upstream of the stream riffle and in the riparian wetland. This occurrence of both gaining and losing conditions in different sections of the stream was not persistent during wet conditions. After a series

Die approbierte gedruckte Originalversion dieser Dissertation ist an der TU Wien Bibliothek verfügbar.
The approved original version of this doctoral thesis is available in print at TU Wien Bibliothek.
TU WIEN Bibliothek Your knowledge hub

of precipitation events (total precipitation = 49 mm between 1 and 8 March 2019) the groundwater level increased and α pointed towards the stream channel throughout the study reach (8 March 2019, median$_{\text{GW\_wells}}$ = 16.6 cm, median$_{\text{GW\_piezo}}$ = 5.2 cm above the streambed; Figure 1.7(f), blue arrows). Groundwater in the piezometers was generally below the adjacent groundwater in the footslopes (e.g., $\Delta\,\text{GW}_{\text{6P2-6W2}} = -6$ cm) and at the same level or above the streamwater level (e.g., $\Delta\,\text{GW}_{\text{6P2-SW}} = 0$ cm). An exception was the east footslope close to the riffle, where local gradients pointed away from the stream channel.

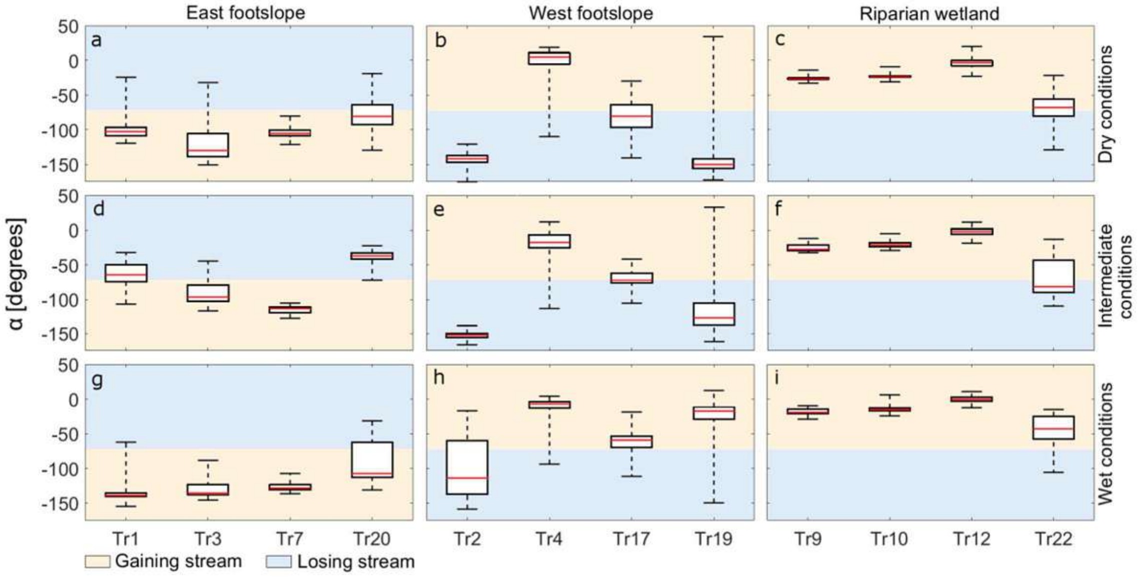

Figure 1.8. Boxplots of groundwater flow direction α for a selection of triangles (Figure 1.2). (a) East footslope dry conditions, (b) west footslope dry conditions, (c) riparian wetland dry conditions, (d) east footslope intermediate conditions, (e) west footslope intermediate conditions, (f) riparian wetland intermediate conditions, (g) east footslope wet conditions, (h) west footslope wet conditions, and (i) riparian wetland wet conditions. Boxes indicate 25%–75% quantiles, whiskers, minima and maxima. The dry, intermediate and wet conditions analysed here refer to the intervals reported in Table 1.2 and shown in Figure 1.3.

The analysis of groundwater flow directions with continuously-monitored wells is generally consistent with the biweekly data and provided clear short-term dynamics of α and the duration of the gaining and losing conditions for different sections of the stream corridor (Figure 1.8). On the east footslope, α pointed towards the stream channel in dry, intermediate, and wet conditions in most triangles for most of the time (Figure 1.8(a),(d),(g)). However, during intermediate and dry conditions, α occasionally pointed away from the stream channel (Figure 1.8(a),(d)). On the west footslope, the groundwater flow direction towards the stream channel became relatively more important compared to the groundwater flow direction pointing away the stream channel with increasing wetness conditions (Figure 1.8(b),(e),(h); Tr2, Tr19). Here, spatial differences were observed in triangles closer to the stream, where α pointed mostly parallel ($\simeq -72°$) to the stream channel (Figure 1.8(b),(e),(h); Tr17), and in triangles closer to the riparian wetland, where α pointed constantly towards the stream channel (Figure 1.8(b),(e),(h); Tr4). In the riparian wetland, α nearly continuously pointed towards the stream channel for different hydrologic conditions (Figure 1.8(c),(f),(i)) with some exceptions close to the stream (cf. Triangle 22).

The continuously observed groundwater wells allowed us to capture the behaviour of α during the transition from dry to wet conditions (Figure 1.9(a)–(d)) and during events (Figure 1.9(e)–(l)). The transition was accompanied by a gradual change in α towards the stream on the east (Figure 1.9(b)) and west (Figure 1.9(c)) footslopes and partly in the riparian wetland (Figure 1.9(d)). α also varied between the directions of the fall line of the surface topography and the direction of the fall line of the factured bedrock surface for the majority of the continuously monitored wells.

The continuous measurements offered insights into event-based changes of α. During dry conditions, precipitation events were followed by sporadic re-appearance of the streamflow in the channel (from $Q = 0$ to $Q > 0$ L/s for 3 h Figure 1.9(a),(e)) and a shift of groundwater flow direction on the east footslope, with α pointing towards the stream between events and towards the hillslope after events (Figure 1.9(b),(g)). On the west footslope, α always pointed towards the hillslope (Figure 1.9(c)) and was almost perpendicular to the stream channel ($\alpha \sim -160°$) after events (Figure 1.9(i)). During wet conditions, precipitation events were followed by an increase of streamflow (Figure 1.9(f)) and a more pronounced groundwater flow direction towards the stream. While this variation did not considerably change α on the east footslope (Figure 1.9(b),(h)), it caused a change in the groundwater flow direction on the west footslope. Here, α shifted from pointing towards the footslope during recessions to pointing towards the stream during and few days (up to 3 days) after events (Figure 1.9(c),(j)). In the riparian wetland, α always pointed towards the stream channel (Figure 1.9(d)) and approached the direction of the surface fall line after sporadic precipitation events in dry conditions (Figure 1.9(k)) and persistently during wet conditions (Figure 1.9(l)).

1.6 Discussion

1.6.1 Drivers of near-stream groundwater dynamics

1.6.1.1 Role of depth-dependent storage capacity on groundwater response

We observed clear differences in groundwater response to precipitation between dry, intermediate, and wet conditions with the most pronounced and fastest increase of groundwater levels during dry conditions, and more delayed and less pronounced increases during wet conditions (Figure 1.4). Our results suggest that a decrease in porosity and storage capacity with depth act as critical controls on the average precipitation depth necessary to trigger a groundwater level increase and groundwater response times. This is supported by the Spearman correlation coefficients, which suggest that the deeper the initial groundwater table is, the faster and the higher the groundwater table response to precipitation (Figure 1.6(d),(h), Appendix C). This is due to the subsurface layering in the Weierbach, with high porosity and storage capacity in the solum and subsolum, and lower porosities and storage capacity in the fractured bedrock below (Glaser et al., 2016; Martínez-Carreras et al., 2016). When groundwater levels were located in the low porous fractured bedrock (~10% – 15%, Table 1.1), the same amount of precipitation led to a more pronounced increase compared to higher groundwater stages where porosity was higher (15% – 30% in the subsolum and 45% – 61% in the solum, Table 1.1).

The role of variable storage capacities in the subsurface has been highlighted at other catchments, where groundwater response was faster and more pronounced in locations characterised by soils with low storage capacities compared to deeper soils with higher storage capacities (Penna et al., 2015; Rinderer et al., 2016; Rinderer et al., 2017; Rodhe & Seibert, 2011). These studies showed a spatial effect of storage capacity leading to a spatially non-unison response across hillslopes. Adding to this, we showed that the vertical decrease in storage capacity leads to clearly different groundwater responses between events in different hydrologic conditions. Our results highlight the relevance of covering the full range of hydrologic conditions in order to capture the effect of a decrease of subsurface storage capacity with depth on seasonally different groundwater responses.

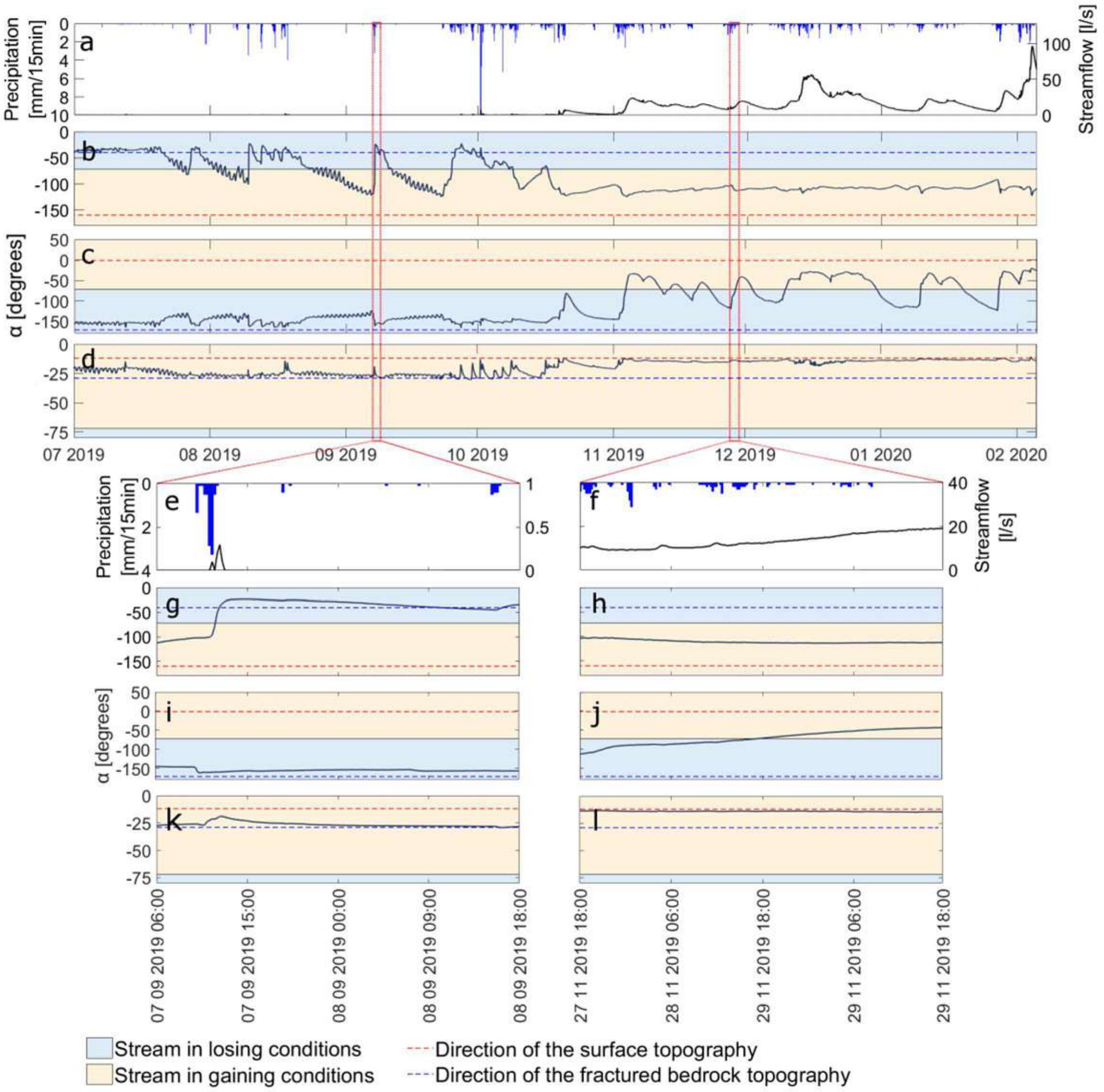

Figure 1.9. (a) Precipitation and streamflow during transition from dry to wet conditions. Groundwater flow direction (α) for a selection of triangles on (b) the east and (c) the west footslope, and (d) the riparian wetland. (e–l) Zoom on streamflow and the change in groundwater flow directions for selected precipitation events during dry and wet conditions.

1.6.1.2 Role of precipitation characteristics on groundwater response

The increase of the groundwater level following events was significantly correlated to precipitation depth for dry, intermediate, and wet conditions and for the entire study period (Figure 1.6(a),

Die approbierte gedruckte Originalversion dieser Dissertation ist an der TU Wien Bibliothek verfügbar.
The approved original version of this doctoral thesis is available in print at TU Wien Bibliothek.
TU WIEN Bibliothek Your knowledge hub

regolith. As a result, groundwater in shallower soils close to the stream quickly rose into the upper and more porous soil and displayed a lower increase than groundwater further from the stream. This result is consistent with observations at other sites, where the water table rose more in locations characterised by thicker soils further from than stream than in locations characterised by shallower soils (Penna et al., 2015).

When the groundwater level is below the fractured bedrock surface (i.e., dry conditions), the derived correlations indicate that groundwater further from the stream responds with a delayed and less pronounced increase compared to groundwater closer to the stream (Table C3). This result can be explained by inflow from the stream channel into footslopes. This is also consistent with groundwater levels below the dry streambed, which increased above the adjacent groundwater after precipitation events (Figure 1.7(e)).

During intermediate conditions, the correlation analysis was not able to decipher different drivers controlling the groundwater dynamic in the system (Table C3). This might be explained by the fact that the increase of the groundwater table above the fractured bedrock is neither in unison in time nor uniform in space during the transition from dry to wet conditions (and vice versa). Therefore, the groundwater dynamic for some wells might be controlled by regolith depth, as observed during wet conditions, while the groundwater table response to events might be controlled by streamwater inflow for other wells, like during dry conditions.

1.6.2 Drivers of near-stream groundwater flow directions depending on hydrologic conditions

1.6.2.1 Role of upslope-footslope connectivity and streamwater level

The more pronounced groundwater flow direction observed towards the stream channel with increasing wetness conditions can be explained by seasonal groundwater dynamics in the hillslopes. In the Weierbach catchment, high evapotranspiration in summer depletes storage in the regolith (Glaser et al., 2016) and groundwater tables in the hillslopes decrease into the fractured bedrock (Rodriguez & Klaus, 2019). During the wet-up, the groundwater table rises across the hillslope into more conductive layers and contributes increasingly to streamflow (Rodriguez & Klaus, 2019). Despite the lack of an extended groundwater monitoring network across hillslopes, the groundwater flow direction observed towards the stream channel, together with previous modelling results (Glaser et al., 2020), indicate persistent hydrologic connectivity between near-stream and upslope groundwater during wet conditions. This interpretation is in agreement with several studies on hydrological connectivity in different landscapes, which consistently found near-stream groundwater flow direction pointing towards the stream when the inflow from upslope locations maintained high levels of near-stream groundwater (Rodhe & Seibert, 2011; van Meerveld et al., 2015; Vidon & Hill, 2004).

However, α did not point uniformly towards the stream channel during wet conditions, and in some sections of the reach, groundwater flow direction pointed towards the stream channel only after precipitation events (Figures 1.7(f) and 1.8(b),(c)). Here, groundwater flow direction shifted from pointing towards the stream after events to pointing towards the footslopes during recessions

out. Therefore, our work highlights the importance of a spatially dense monitoring network in capturing the marked variability characterising streamwater-groundwater mixing.

1.6.2.2 The role of surface topography and anisotropic hydraulic conductivity of the fractured bedrock

During dry conditions, groundwater on the west and east footslopes decreased below the streambed into the fractured bedrock, and streamflow ceased (Figure 1.5(d)). At this stage, the groundwater flow direction showed a diverse pattern and pointed away from the stream at some locations and towards the stream at others (Figure 1.7(e)). This might be explained by a strong anisotropic hydraulic conductivity of the fractured bedrock. The weathering of bedrock can be heterogeneous, leading to the presence of preferential flowpaths (Gabrielli et al., 2012) and local changes in hydraulic conductivity (Hopp & McDonnell, 2009), resulting in spatial differences in the groundwater table (Welch & Allen, 2014). Moreover, bedrock fractures do not necessarily imply connectivity between wells and we do not necessarily expect the groundwater flow to exactly follow the observed gradients. This is reflected in Darcy's law if the conductivity tensor has large off-diagonal coefficients. The impact of fractured bedrock on groundwater flow directions is also evident once the groundwater rises above the fractured bedrock, then the groundwater table direction approaches the fractured bedrock fall line. This is apparent after precipitation events in dry conditions, when groundwater in some stream sections rose above the adjacent groundwater (Figure 1.7(e)), groundwater flow direction pointed towards the bedrock depression in the footslopes, and α approached the fractured bedrock fall line after events at several locations (Figure 1.9(b),(c),(g),(i)). These results are in line with observations in hillslope studies that showed that groundwater flow direction reflected the bedrock fall line during dry conditions (Hutchinson & Moore, 2000; van Meerveld et al., 2015). However, the information available on α in intermediate and wet conditions also demonstrated no significant correlation between α and the groundwater elevation above the fractured bedrock (results not shown). This is probably because inflow from upslope groundwater and the stream channel to stream corrido groundwater quickly fills the bedrock depressions in wetter conditions, interrupting their influence on the groundwater flowpaths.

1.6.3 Implications for runoff generation and hydrological connectivity

Without additional data on groundwater flow direction, one may have interpreted the observed response of groundwater before streamflow response in dry conditions at the study site as groundwater contributing to streamflow generation. Such an interpretation would be in agreement with hillslope-stream connectivity studies, which concluded that streamflow generation is driven by groundwater inflow when groundwater responds to events before streamwater (Beiter et al., 2020; Haught & Van Meerveld, 2011; Rinderer et al., 2016). However, α and the detailed pattern of the groundwater level, that was consistently below the streamwater level, clearly showed that groundwater flow direction pointed towards the hillslope during and after precipitation events in dry conditions. This is evidence for the lack of groundwater contributions to streamflow generation in the study reach.

α and groundwater level above the streamwater level jointly revealed that groundwater contributes to streamflow generation both before and after precipitation events during wet

While the lag time between groundwater and streamflow response to events can be used as indicator for groundwater contribution to streamflow generation and hillslope-stream connectivity, the observed groundwater flow directions were important to avoid result misinterpretation and allowed us to decipher different streamflow-generation processes in dry and wet conditions. The water flowpaths observed have important implications for solutes, nutrients and dissolved oxygen transport in the stream corridor with a strong potential for the development of hot-spots and hot-moments both in dry and wet hydrologic conditions. In conclusion, the results presented in this work offer new insights into the spatial heterogeneity and the time-variant role that different drivers exert on stream-groundwater exchange across a wide variety of precipitation events and hydrologic conditions. Additionally, our results highlight the pivotal importance of long-term observations in the stream corridor domain, since the lack of spatially-dense and high-frequency measurements can cause misinterpretation in the streamflow generation process, streamwater-groundwater exchange and hillslope-stream connectivity.

1.8 Acknowledgements

This work was supported by the funding from the Luxembourg National Research Fund (FNR) for doctoral training (PRIDE15/10623093/HYDRO-CSI). We would like to acknowledge the financial support of the Austrian Science Fund (FWF) as part of the Vienna Doctoral Programme on Water Resource Systems (DK W1219-N28). We thank Laurent Gourdol for providing the ERT surveys and analysing the resistivity data. We also thank Jean-François Iffly, Jérôme Juilleret, and Laurent Gourdol for their help in the installation of the monitoring well network and Cyrille Tailliez for the theodolite surveys. We thank Marta Antonelli, Samuele Ceolin, Ginevra Fabiani, Barbara Glaser, Christopher Hissler, Adnan Moussa, Laurent Pfister, and Nicolas Rodriguez for their fruitful input and discussions

“Let us imagine a man who, while standing on the street, would say to himself:

“It is six o'clock in the evening, the working day is over. Now I can go for a walk, or I can go to the club; I can also climb up the tower to see the sunset; I can go to the theatre; I can visit this friend or that one; indeed, I also can run out of the gate, into the wide world, and never return. All of this is strictly up to me, in this I have complete freedom. But still I shall do none of these things now, but with just as free a will I shall go home to my wife”.

This is exactly as if water spoke to itself:

“I can make high waves (yes! in the sea during a storm), I can rush downhill (yes! in the river bed), I can plunge down foaming and gushing (yes! in the waterfall), I can rise freely as a stream of water into the air (yes! in the fountain), I can, finally boil away and disappear (yes! at a certain temperature); but I am doing none of these things now, and am voluntarily remaining quiet and clear water in the reflecting pond.”

– Arthur Schopenhauer, Essay on the Freedom of the Will

Die approbierte gedruckte Originalversion dieser Dissertation ist an der TU Wien Bibliothek verfügbar.
The approved original version of this doctoral thesis is available in print at TU Wien Bibliothek.
TU Bibliothek
Your knowledge hub
WIEN

1. How does the identifiability of model parameters change in the random sampling of TSM when velocity is considered as a calibration parameter and when it is assumed fixed and equal to v_{peak}?
2. Does the identifiability analysis on specific sections of the BTC reduce the parameter non-identifiability in random sampling of TSM?
3. How much does the identifiability of model parameters in random sampling approaches depend to the used parameter range and on the number of parameter sets?

With the outcomes of these questions we will address:

4. How does the hydrologic interpretation of TSM results vary when model parameters are identifiable and when they are not?

2.2 Study site and methods

2.2.1 Study site and tracer data

The studied stream reach (49°49'38''N, 5°47'44''E) is located in western Luxembourg, downstream of the Weierbach experimental catchment (Hissler et al., 2021; Fabiani et al., 2021). The stream channel is unvegetated with a slope of ≃6% and consists of deposited colluvium material and fragmented schists (up to 50 cm depth) with local outcrops of fractured slate bedrock in the streambed. The flow regime is governed by the interplay of seasonality between precipitation and evapotranspiration (Rodriguez and Klaus, 2019; Rodriguez et al., 2021) with a persistent discharge between autumn and spring, and little to no discharge during summer months (discharge arithmetic mean equal to 6.5 l/s, median of 1.7 l/s, St.Dev. of 11.52 l/s between Aug 2018 and Feb 2020; Bonanno et al., 2021). To answer our research questions, we utilise three tracer experiments with an instantaneous tracer injection at three different flow (Q) conditions: 6th December 2018, Q = 2.52 l/s (E1); 23rd January 2019, Q = 9.05 l/s (E2); 28th January 2019, Q = 22.79 l/s (E3). For each experiment, we prepared a NaCl solution using 2 l of stream water and 100 g of reagent-grade NaCl. We injected the solution into a turbulent pool at the beginning of the stream reach to assure complete mixing in the stream water. Electric conductivity (EC) was measured via a portable conductivity meter (WTW) 55 m downstream of the injection point. Automatic compensation of stream temperature occurred (nLF, according to EN 27 888). EC-Cl^- conversion was obtained using a known-volume sample of stream water taken before tracer injection at the measurement location and adding known quantities of a solution with a known concentration of Na-Cl. Conversion into Cl- concentration was obtained via an EC-Cl^- regression line (R^2 = 0.9999). Discharge was calculated for every slug injection via the dilution gauging method using the Cl^- concentration obtained for each BTC (Beven et al., 1979; Butterworth et al., 2000).

2.2.2 Advection-dispersion equation and Transient Storage Model formulation

The one-dimensional Fickian-type advection and dispersion equation describes the combined effect of flow velocity and turbulent diffusion on solute transport (Beltaos and Day, 1978; Taylor, 1921, 1954). The differential form of ADE reads:

$$\frac{\partial C}{\partial t} = -v\frac{\partial C}{\partial x} + \frac{1}{A}\frac{\partial}{\partial x}\left(AD\frac{\partial C}{\partial x}\right) \qquad \text{Eq.1}$$

where t is time [T], x is the distance from the injection point along the stream reach [L], A [L^2] is the cross-sectional area of flow, v [L/T] is the average flow velocity, D [L^2/T] is the longitudinal dispersion coefficient, and C is the concentration of the observed tracer above background levels [M/L^3]. The solution of the differential form of ADE for an instantaneous solute injection at $x = 0$ [L] reads:

$$C(t) = \frac{M}{A(4\pi Dt)^{1/2}} exp\left[-\frac{(L-vt)^2}{4Dt}\right] \qquad \text{Eq. 2}$$

where M is the injected solute mass [M], t is time [T], and L is the length of the investigated reach [L].

The TSM describes the solute transport in streams by combining the advection-dispersion process in the stream channel through a hydrologic exchange with an external storage zone. The model equations read (Bencala and Walters, 1983):

$$\begin{cases} \frac{\partial C}{\partial t} = -v\frac{\partial C}{\partial x} + \frac{1}{A}\frac{\partial}{\partial x}\left(AD\frac{\partial C}{\partial x}\right) + \alpha(C_{TS} - C) \\ \qquad \frac{\partial C_{TS}}{\partial t} = -\alpha\frac{A}{A_{TS}}(C_{TS} - C) \end{cases} \qquad \text{Eq.3}$$

where the hydrologic exchange with the transient-storage zone is driven by the exchange coefficient α [1/T] and the area of the transient storage zone, A_{TS} [L^2]. Here, we will refer to A, v, and D as "advection-dispersion parameters" and to A_{TS} and α as "transient storage parameters". The solute concentrations in the main channel and the transient storage zone are C and C_S [M/L^3], respectively. The performances of both ADE and TSM results are evaluated using the Root Mean Squared Error objective function (*RMSE*). *RMSE* is an equivalent form of Residual Sum of Squares (RSS) and Mean Absolute Error (MAE) objective functions that are used in OTIS-P (the most frequently adopted inverse modelling approach for TSM, Runkel, 1998) and by the dynamic identifiability analysis (Wagener et al., 2002). *RMSE* allowed us a comparison of our TSM results with OTIS-P and with dynamic identifiability analysis consistently to previous studies (Wlostowski et al., 2013; Ward et al., 2017).

2.2.3 Random sampling and global identifiability analysis

Several sampling approaches were previously used to estimate parameter identifiability in TSMs, such as Monte Carlo sampling (Wagner and Harvey, 1997; Wagener et al., 2002; Ward et al., 2013), Latin hypercube sampling (LHS, Ward et al., 2018; Kelleher et al., 2019), and Monte Carlo coupled with a behavioural threshold (Kelleher et al., 2013; Ward et al., 2017). Here, we use LHS to sample from the selected parameter range, due to LHS's higher efficiency compared to the classic Monte Carlo approach (Yin et al., 2011). A single combination of model parameters (A, v, and D for ADE and A, v, D, A_{TS}, and α for TSM) obtained from the random sampling approach is herein referred to as "parameter set".

To obtain reliable TSM results, Ward et al. (2017) suggested a minimum amount of parameter sets between 10,000 and 100,000. Thus, in each TSM iteration we simulated 115,000 parameter sets. Results of each TSM iteration include *RMSE* values for the 115,000 parameter sets, and results of identifiability analysis of the model parameters. The identifiability analysis includes parameter vs

Die approbierte gedruckte Originalversion dieser Dissertation ist an der TU Wien Bibliothek verfügbar.
The approved original version of this doctoral thesis is available in print at TU Wien Bibliothek.
TU WIEN Bibliothek Your knowledge hub

Die approbierte gedruckte Originalversion dieser Dissertation ist an der TU Wien Bibliothek verfügbar.
The approved original version of this doctoral thesis is available in print at TU Wien Bibliothek.
TU WIEN Bibliothek Your knowledge hub

RMSE plots (Wagener et al., 2003), parameter distribution plots (Ward et al., 2017), regional sensitivity analysis (Wagener and Kollat, 2007; Kelleher et al., 2019), and parameter distribution plots (Wagener et al., 2002; Ward et al., 2017). Since the above-mentioned identifiability analysis refers to model performance (*RMSE*) evaluated on the entire BTC, we refer to it as "global identifiability analysis." Globally identifiable parameters satisfy the following criteria: a univocal peak of performance in parameter vs *RMSE* plots and in parameter distribution plots (Ward et al., 2017) and cumulative distribution function (CDF) corresponding to the best 0.1% of the results deviating from the 1:1 line and from parameter CDF corresponding to the best 10% of the results (Kelleher et al., 2019). We selected these behavioural thresholds (top 0.1% and top 10%) to assure consistency with previous work (Wagener et al., 2002; Wlostowski, 2013; Ward 2013; Ward 2017; Kelleher 2019). Parameter identifiability is usually evaluated via visual inspection of the plots from the global identifiability analysis (Wagener et al., 2002; Wlostowski et al., 2013; Ward et al., 2017; Ward et al. 2018; Kelleher et al., 2019). To couple visual inspection with a numerical measure able to express the degree of identifiability of a certain parameter, we evaluated the two-sample Kolmogorov-Smirnov (K-S) test that calculates the maximum distance K and the corresponding *p*-value between two cumulative distribution functions, $F(P_{0.1})$ and $F(P_{10})$, by:

$$[K,p] = max|F(P_{0.1}) - F(P_{10})| \qquad \text{Eq. 4}$$

Where $F(P_{0.1})$ and $F(P^{10})$ are the cumulative distribution function of a parameter P respectively for the best 0.1% and the best 10% of the results. Following the approach of Ouyang et al. (2014), we grouped parameter identifiability in four categories: highly identifiable ($K > 0.25$, $p \leq 0.05$), moderately identifiable ($0.1 \leq K \leq 0.25$, $p \leq 0.05$), poorly identifiable ($K < 0.1$, $p \leq 0.05$), and non-identifiable ($p > 0.05$).

2.2.4 Identifiability analysis on specific sections of the BTC

100 best-performing parameter sets for each iteration were analysed with the DYNamic Identifiability Analysis (DYNIA, Wagener et al., 2002) to address the role of model parameters on different sections of the BTC. Compared to the global identifiability analysis, the dynamic identifiability analysis evaluates the identifiability of a parameter on a moving window along the BTC. Following the approach of Wagener et al. (2002), we used a window size of three time steps (~1 min for E1 and E2, and ~15 secs for E3). The dynamic identifiability analysis identifies regions of the observed data that are identifiable (or not) to the investigated model parameter, and it can be used to test model structure, to design specific experiments, and to relate the model parameters to a specific simulated model response (Wagener et al., 2004). The dynamic identifiability analysis yields the distribution of the likelihood (i.e. mean absolute error, Wagener and Kollat, 2007) as a function of the parameter values and the information content of the parameters over time. The information content is expressed as one minus the width of the 90% confidence interval over the entire parameter range (Wagener et al., 2002). A wide 90% confidence interval indicates that various parameter values are associated to equally good performances resulting in low information content. Conversely, narrow 90% confidence intervals and corresponding high information content values suggest that the best-performing parameters are contained in a relatively narrow range compared to the feasible range. To evaluate the degree of identifiability of a certain parameter on

specific sections of the BTC, we grouped parameter identifiability in three categories: highly identifiable (information content ≥ 0.66), moderately identifiable ($0.33 \leq$ information content < 0.66), and poorly identifiable (information content < 0.33). We also specified sections of the BTC as follows: "peak" of the BTC is the section of the BTC corresponding to a neighbourhood interval of three time steps (± ~1 min for E1 and E2, and ± ~15 secs for E3) around the maximum observed concentration; "rising limb" and the "tail" are respectively the BTC sections before and after the peak. A detailed description of how to read the plots used to address the global identifiability analysis and the description of the dynamic identifiability analysis algorithm are reported in Appendix D.

2.2.5 Iterative approach to achieve model identifiability

We simulated our tracer experiments with the ADE to avoid initial assumptions on advection-dispersion parameters that could affect the identifiability of transient storage parameters (Figure 2.1). The *RMSE* value of the best-performing ADE parameter set is referred to as $RMSE_{ADE}$. After obtaining identifiable advection-dispersion parameters, we simulated the observed BTC with the TSM by sampling advection-dispersion parameters from a parameter range defined based on the ADE results, while the transient storage parameters were based on literature values (Table 2.1). This first TSM simulation over 115,000 parameter sets is referred as to first TSM iteration.

Similar to the Monte Carlo approach coupled with behavioural thresholds (Kelleher et al., 2013; Ward et al., 2017) starting from the result of the first TSM iteration, we simulated the three tracer experiments through a step-wise approach with n TSM iterations (n is the number of iterations, Figure 2.1). The n TSM iterations sampled 115,000 parameter sets via LHS over parameter ranges defined by the results of the previous TSM iteration. Namely, if the global identifiability analysis from the previous TSM iteration indicated that the investigated parameter is identifiable, the best 10% of the results were used to define its parameter range in the successive TSM iteration (Figure 2.1). When the identifiability criteria were not met, the parameter range investigated in the successive TSM iteration was increased or, for the case of A_{TS} and α, it was reduced based on the dynamic identifiability analysis result (information content above 0.66 on the BTC tail). This condition was chosen by the evidence that transient storage parameters A_{TS} and α are often non-identifiable via global identifiability analysis (Camacho and González, 2008; Ward et al., 2013; Ward et al., 2017; Kelleher et al., 2019), but are identifiable on the tail of the BTC (Wagener et al., 2002; Kelleher et al., 2013; Wlostowski et al., 2013).

While the first TSM iteration was conducted to investigate the identifiability of all the possible combinations in the feasible parameter range reported in the literature and from the results of ADE (Table 2.1), the successive iterations excluded pairs of v and A whose product was outside the value of the discharge evaluated via dilution gauging ±10%. This condition was chosen to respect results from Schmadel et al. (2010), who reported that the discharge error from the dilution gauging method is ≃8%. The same approach (Figure 2.1) was used also in the case where v was assumed fixed and equal to $v_{peak} = L/t_{peak}$, where t_{peak} is the arrival time of the concentration peak. This choice was motivated by the fact that v_{peak} is commonly adopted as a value for velocity in many transient storage studies (Ward et al., 2013; Kelleher et al., 2013; Wlostowski et al., 2017; Ward et

Die approbierte gedruckte Originalversion dieser Dissertation ist an der TU Wien Bibliothek verfügbar.
The approved original version of this doctoral thesis is available in print at TU Wien Bibliothek.
TU Bibliothek WIEN Your knowledge hub

al., 2017; Ward et al., 2018). The modelling was finalized once every model parameter indicated global identifiability via the enunciated criteria and the Kolmogorov-Smirnov test resulted in K > 0.1 and $p \leq 0.05$ for each model parameter.

Table 2.1. Parameter names, abbreviations, and units together with a summary of publications that address identifiability of model parameters with random sampling approaches. We reported the used number of parameter sets and the parameter ranges, while in parenthesis it is reported the method used for the parameter sampling. "Double step" indicates that the sampling procedure was divided into two steps. In the first step, A varied across a broad range and in the second step, it was varied across a narrower range to cover the most sensitive range of the parameter domain. Each of the two steps investigated a number of parameter sets equal to half of the total number indicated in the table.

Parameters	**Units**	**Symbol**	
Streamflow velocity	[m/s]	v	
Stream channel area	[m^2]	A	
Longitudinal dispersion coefficient	[m^2/s]	D	
Stream-storage zone exchange rate	[1/s]	α	
Transient storage area	[m^2]	A_{TS}	
Authors	**Number of parameter sets**	**Range of TSM parameters**	
Wagner and Harvey, 1997	800 (Monte Carlo)	A	0.02 - 0.6
		D	0.025 - 0.8
		A_{TS}	0.01 - 2
		α	0.000005 - 0.001
Wagener et al., 2002	1,000 (Monte Carlo)	A	0.3 - 1.05
		D	0.1 - 0.225
		A_{TS}	0.1 - 0.5
		α	0.00035 - 0.0025
Wlostowski et al., 2013	2,000 (Monte Carlo)	A	0.5 - 1.0
		D	0.5 - 1.5
		A_{TS}	0.05 - 0.5
		α	10^{-4} - 10^{-3}
Kelleher et al., 2013	42,000 (Double step Monte Carlo)	A	0.01 - 1.0 (in the second step, limits chosen via the top 1,000 results of first step)
		D	0.001 - 1.0
		A_{TS}	0.001 - 0.01
		α	10^{-5} - 10^{-3}
Ward et al., 2013	100,000 (Monte Carlo)	A	±50% A_{peak}
		D	0.0001 - 5
		A_{TS}	0.01 - 10
		α	10^{-8} - 10^{-1}
Ward et al., 2017	100,000 (Double step Monte Carlo)	A	0.1 - 1 (0.3-0.5 in the second step)
		D	0.01 - 10
		A_{TS}	0.01 - 1
		α	10^{-5} - 10^{-1}
Kelleher et al., 2019	27,000 (LHS)	A	1.0 - 3.0
		D	0.001 - 10

Die approbierte gedruckte Originalversion dieser Dissertation ist an der TU Wien Bibliothek verfügbar.
The approved original version of this doctoral thesis is available in print at TU Wien Bibliothek.
TU Bibliothek WIEN Your knowledge hub

Die approbierte gedruckte Originalversion dieser Dissertation ist an der TU Wien Bibliothek verfügbar.
The approved original version of this doctoral thesis is available in print at TU Wien Bibliothek.
TU Bibliothek WIEN Your knowledge hub

		A_{TS}	0.01 - 1	
		α	10^{-6} - 10^{-2}	
This manuscript	Second step ADE – 35,000 (LHS)	v	$v_{peak} \cdot 0.8$ - velocity of the first increase of concentration	
		A	± 20% A_{peak}	
		D	0.0001 - $D_{best} \cdot 1.2$	
This manuscript	First TSM iteration – 115,000 (LHS)	v	± 50% v_{ADE}	
		A	± 50% A_{ADE}	
		D	0.0001 - $D_{ADE} \cdot 2$	
		A_{TS}	0.00001 - 20	
		α	0.00001 - 0.1	

2.2.6 Number of parameter sets, parameter range, and identifiability of model parameters

For each TSM iteration, we randomly extracted N parameter sets and their corresponding results. We then computed the mean and standard deviation of the top 10% of model performance results (*RMSE*) considering only the extracted subset of parameters N instead of the total 115,000. N increased from 1,000 to 115,000 with intervals of 1,000 parameter sets. We then evaluated the change in model performance with the changing number of sampled parameter sets for the different TSM iterations for the three experiments. A continuous decrease of the mean and the standard deviation of the top 10% model performance results (*RMSE*) with increasing N shows that the number of chosen parameter sets clearly affects the performances of the random sampling approach for the investigated parameter range. On the contrary, a constant mean and standard deviation of the top 10% model performance results over increasing N points to the inability of the model and modelling procedure to increase the performances with an increasing number of parameter sets for that investigated parameter range (Pianosi et al., 2015).

2.2.7 Comparison with an inverse modelling scheme and a Monte Carlo random sampling approach

We compared our results with both inverse modelling results (OTIS-P) and the most-common random sampling approach for TSMs (OTIS-MCAT). OTIS-P is an inverse modelling scheme that minimises the residual sum of squares between the modelled and the observed BTC. OTIS-P model estimates the best-fitting model parameter values and their identifiability via the 95% confidence interval. We carried out multiple OTIS-P iterations starting from different initial parameter values to avoid a local minimum and interrupted the iterations when parameter values calibrated via OTIS-P changed less than 0.1% between subsequent runs (Runkel, 1998). OTIS-MCAT solves the TSM for the selected number of parameter sets and addresses their identifiability with a global identifiability analysis (Ward et al., 2017). Compared to our approach, OTIS-MCAT considers Monte Carlo parameter sampling instead of LHS, velocity equal to v_{peak} and it does not foresee iterative parameter sampling from results of dynamic identifiability analysis. Thus, we here indicate as "OTIS-MCAT results" the results we obtained after the first TSM iteration when v was assumed fixed and equal to v_{peak}.

Die approbierte gedruckte Originalversion dieser Dissertation ist an der TU Wien Bibliothek verfügbar.
The approved original version of this doctoral thesis is available in print at TU Wien Bibliothek.
TU Bibliothek Your knowledge hub WIEN

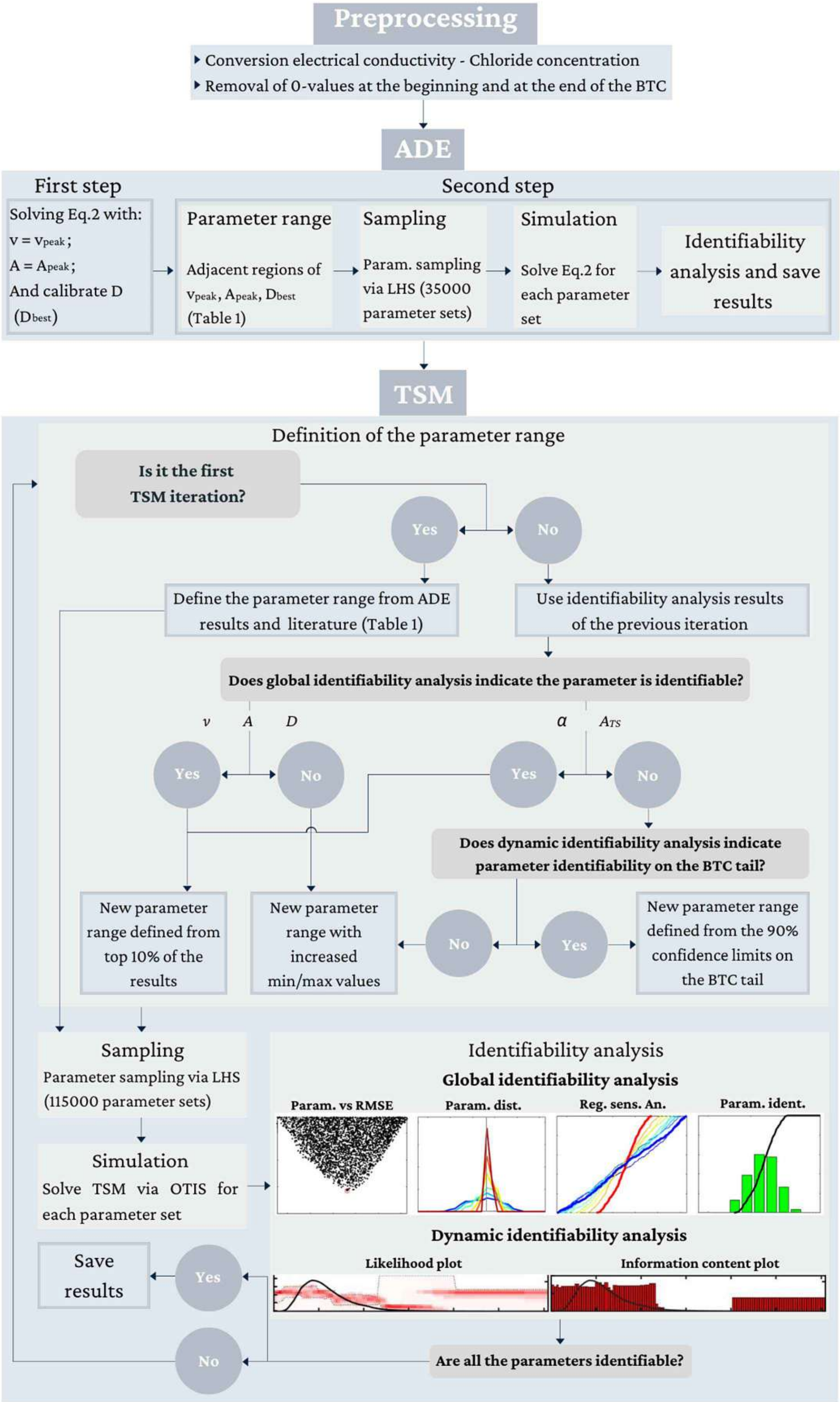
Preprocessing
Conversion electrical conductivity - Chloride concentration
Removal of 0-values at the beginning and at the end of the BTC
ADE
First step
Second step
Solving Eq.2 with:
v = vpeak ;
A = Apeak ;
And calibrate D
(Dbest)
Parameter range
Adjacent regions of vpeak, Apeak, Dbest (Table 1)
Sampling
Param. sampling via LHS (35000 parameter sets)
Simulation
Solve Eq.2 for each parameter set
Identifiability analysis and save results
TSM
Definition of the parameter range
Is it the first TSM iteration?
Yes
No
Define the parameter range from ADE results and literature (Table 1)
Use identifiability analysis results of the previous iteration
Does global identifiability analysis indicate the parameter is identifiable?
v
A
D
α
ATS
Yes
No
Yes
No
Does dynamic identifiability analysis indicate parameter identifiability on the BTC tail?
New parameter range defined from top 10% of the results
New parameter range with increased min/max values
No
Yes
New parameter range defined from the 90% confidence limits on the BTC tail
Sampling
Parameter sampling via LHS (115000 parameter sets)
Simulation
Solve TSM via OTIS for each parameter set
Identifiability analysis
Global identifiability analysis
Param. vs RMSE
Param. dist.
Reg. sens. An.
Param. ident.
Dynamic identifiability analysis
Likelihood plot
Information content plot
Save results
Yes
No
Are all the parameters identifiable?

Figure 2.1: Conceptual modelling workflow. The parameters have the following unit of measurements: velocity v [m/s], cross-sectional area A [m^2], longitudinal dispersion coefficient D [m^2/s], exchange coefficient α [1/s], area of the transient storage zone A_{TS} [m^2].

Die approbierte gedruckte Originalversion dieser Dissertation ist an der TU Wien Bibliothek verfügbar.
The approved original version of this doctoral thesis is available in print at TU Wien Bibliothek.
TU Bibliothek WIEN Your knowledge hub

2.2.8 Metrics and hydrologic interpretation of TSM results

The model parameter sets obtained from OTIS-P, OTIS-MCAT, and the proposed iterative TSM approach were used to compute some hydrologic metrics relate to solute transport in streams. Here we computed the average distance a molecule travels in the stream channel before entering the transient storage zone (L_s [L], Mulholland et al., 1997):

$$L_S = \frac{v}{\alpha} \tag{Eq.5}$$

The average time spent by a molecule in the transient storage zone (T_{sto} [T]) is evaluated as (Thackston and Schnelle, 1970):

$$T_{sto} = \frac{A_{TS}}{\alpha A} \tag{Eq.6}$$

We computed the average water flux through the storage zone per unit length of the stream channel to interpret the magnitude of flux between the stream channel and the transient storage zone. Then we multiplied the obtained value by the reach length L to obtain the total water flux through the storage zone for the entire stream reach (q_s [L^3/T], modified from Harvey et al., 1996):

$$q_S = \alpha A L \tag{Eq.7}$$

However, the metrics L_s, T_{sto}, and q_s do not encompass both the role of advective transport and of the transient storage. Thus, we also calculated F_{MED} [-] that accounts for the median travel time due to advection-dispersion and transient storage and for the travel time only due to advection-dispersion (Runkel, 2002):

$$F_{MED} \cong \left(1 - e^{\left(-L\frac{\alpha}{v}\right)}\right)\frac{A_{TS}}{A_{TS}+A} \tag{Eq.8}$$

Increasing values of F_{MED} have to be interpreted as increasing the relative importance of the storage zone in the solute transport downstream (Runkel, 2002; Gooseff et al., 2013).

2.3 Results

2.3.1 ADE parameters

The global identifiability analysis showed a clear peak of performance toward univocal values for v, A, and D for all three tracer experiments (E1, E2, E3, cfr. paragraph 2.1, plots reported in figure D3). The model performances varied between $RMSE_{ADE}$ equal to 0.989 mg/l (E3, Q = 22.79 l/s) and $RMSE_{ADE}$ equal to 1.942 mg/l (E1, Q = 2.52 l/s).

2.3.2 TSM parameters

2.3.2.1 Identifiability of model parameters when velocity is considered as a calibration parameter

After the first TSM iteration, the global identifiability analysis indicated that v, D, and α parameters are identifiable with a unique performance peak (K of K-S test always > 0.22 and $p <$ 0.05 for each tracer experiment). However, A and A_{TS} appeared non- or poorly identifiable for the three investigated BTCs (Figure 2.2, green dots, p-value of the K-S test for A_{TS} > 0.05 for each tracer experiment).

The global identifiability of model parameters increased with increasing iterations. In the TSM iterations where A_{TS} or α were poorly or non-identifiable (p-value of the K-S test for $A_{TS} > 0.05$), TSM performances approached at best $RMSE_{ADE}$ (Figure 2.2, green, yellow and blue dots). After four (for E1 and E2) or five (for E3) TSM iterations, the parameter values plotted against the corresponding $RMSE$ values showed a univocal increase in performance toward unique values for v, A, D, α, and A_{TS} (Figure 2.2, orange dots), and the $RMSE$ of the best-performing parameter sets decreased below $RMSE_{ADE}$ (Figure 2.2, black horizontal line). Also, the CDF corresponding to the best 0.1% of the results deviated both from the 1:1 line and from the parameter CDF corresponding to the best 10% of the results (results not shown). These conditions, coupled with the K of K-S test always larger than 0.1 (average K for all the model parameters equal to 0.36, and p-value < 0.05) indicated parameter identifiability and the finalization of the iterative TSM approach.

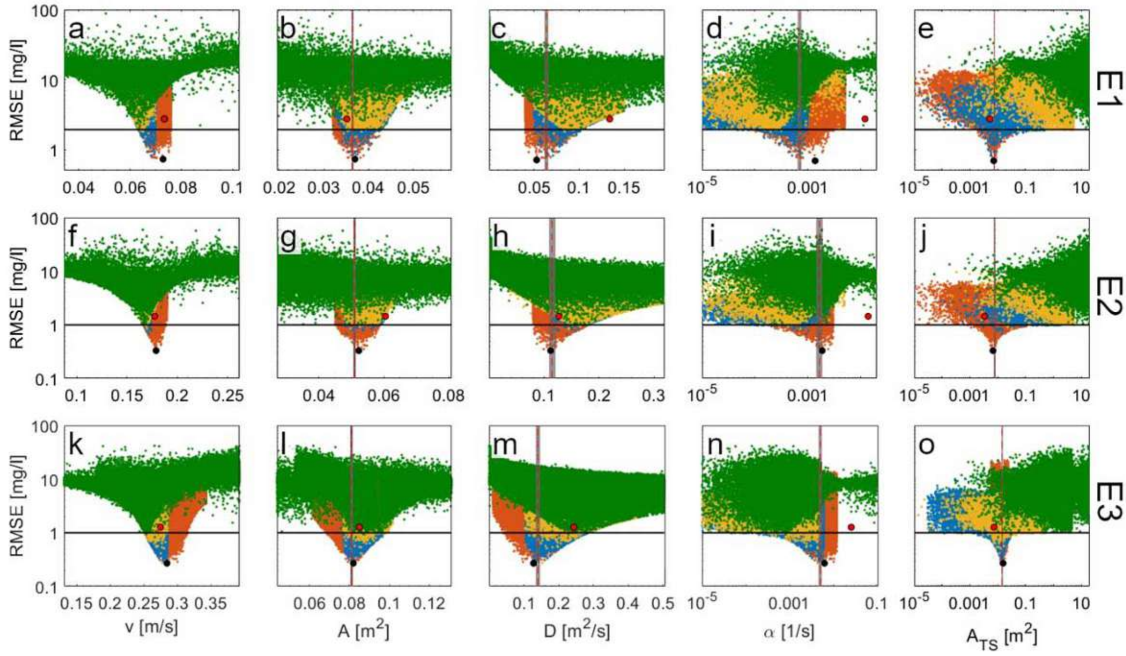

Figure 2.2. Parameter values plotted against the corresponding RMSE values for the TSM results conducted for the tracer injections (a-e) E1, (f-j) E2, and (k-o) E3. (a-j) Green, yellow, blue and orange dots indicate results respectively for the first, second, third, and fourth TSM iterations. (k-o) Green dots indicate results for the first and second TSM iterations, while yellow, blue and orange dots indicate results respectively for the third, fourth, and fifth TSM iterations. Each TSM iteration was conducted via 115,000 parameter sets. The red dots indicate OTIS-MCAT results (best parameter set after the first TSM iteration for v equals vpeak) while the black dots indicate the best-performing parameter value after the used iterative TSM approach. The horizontal black line indicates the RMSEADE (Table 2.2). Vertical dashed red line indicates OTIS-P results, while the 95% confidence range for OTIS-P results are indicated via vertical grey areas.

2.3.2.2 Identifiability of model parameters when velocity is set equal to v_{peak}

The global identifiability of model parameters increased considerably through the iterative model approach also when velocity was not considered a calibration parameter. After the third TSM iteration, the best-performing parameter sets approached unique parameter values (Figure 2.3, blue dots) and the CDF corresponding to the best 0.1% of the results deviated from 1:1 line and from the CDF of the best 10% of the results (results not shown). These conditions, together with K of K-S test always > 0.25 and p-value < 0.05 for each model parameter and tracer experiment, showed a clear increase in identifiability compared to the results after the first iteration (Figure 2.3, green dots). The increase in parameter identifiability was followed by a sharp increase in model performance, with the best-performing parameter sets at the end of the iterative approach having $RMSE$ values below $RMSE_{ADE}$ for all the investigated BTCs (Figure 2.3, blue dots and black line).

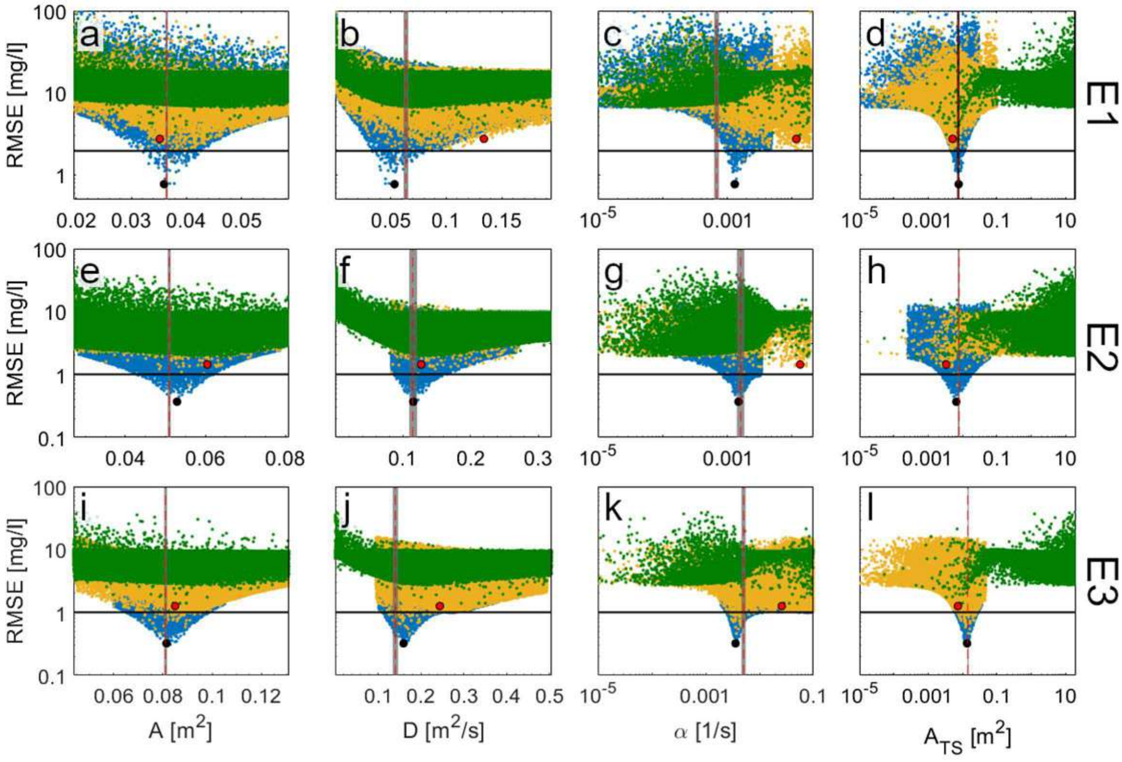

Figure 2.3. Same as Figure 2.2, but reporting TSM results when velocity was considered equal to v_{peak}.

2.3.3 Dynamic identifiability analysis

2.3.3.1 Dynamic identifiability analysis when velocity is considered as a calibration parameter

The dynamic identifiability analysis provided clearer insights into the identifiability of the model parameters for different sections of the BTC compared to the global identifiability analysis (plots shown only for E1). After the first TSM iteration, v and α proved to be the most identifiable and informative parameters on the rising limb, the peak, and the tail of the BTC (information content > 0.66; Figure 2.4a, b, g, h). A and D were mostly identifiable and informative during the rising limb and the tail of the BTC (Figure 2.4c-f). A_{TS} was non-identifiable and poorly informative in most sections of the BTC (information content < 0.33; Figure 2.4i, j). However, the identifiability of A_{TS} increased on the tail of the BTC, where the information content was above 0.66 for A_{TS} between 0.77 m^2 and 5.35 m^2 (Figure 2.4i, j). Results from E2 and E3 showed that α and A_{TS} were highly identifiable (information content > 0.66) for smaller sections of the tail of the BTC when the experiments were conducted at higher discharge stages (information content of $A_{TS} > 0.66$ for 51% of the tail of the BTC for E1, for 23% for E2, and for 19% for E3, results not shown).

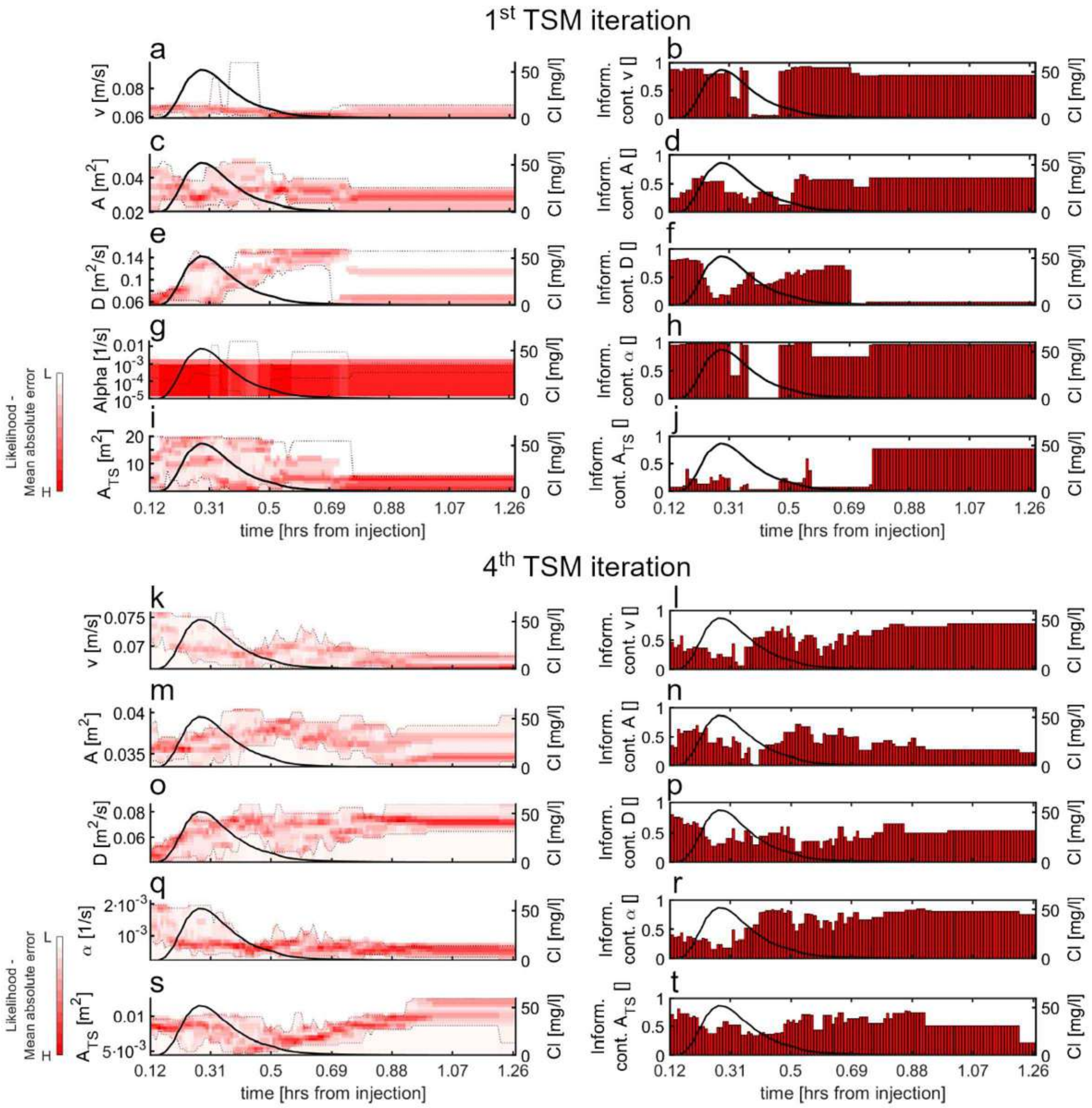

Figure 2.4. Dynamic identifiability analysis of model parameters for E1 when *v* was considered as a varying model parameter. Results report for the (a-j) first TSM iteration and the (k-t) last TSM iteration. (a), (c), (e), (g), (i), (k), (m), (o), (q), (s) likelihood distribution as a function of parameter values at each time step. Black lines indicate the observed BTC, and dashed black lines indicate the 90% confidence limits. (b), (d), (f), (h), (j), (l), (n), (p), (r), (t) indicate parameter information content (red bars) at each time step while the black lines indicate the observed BTC.

The dynamic identifiability analysis for the last TSM iteration showed that the advection-dispersion parameters were important in controlling the rising limb and the tail of the BTC (Figure 2.4k-p), while α was particularly important for controlling the tail (Figure 2.4q, r) and A_{TS} for controlling the rising limb and the tail of the BTC (Figure 2.4s, t). Dynamic identifiability analysis after the last TSM iteration for E2 and E3 showed comparable results (not shown).

2.3.3.2 Dynamic identifiability analysis when velocity is set equal to v_{peak}

After the first TSM iteration, the dynamic identifiability analysis indicated that *A* was poorly identifiable on the entire BTC (results reported only for E1, Figure 5a, b), while *D* was moderately identifiable (information content between 0.66 and 0.33) on the rising limb and on the tail of the

BTC (Figure 2.5c, d). A_{TS} displayed high information content on the entire BTC (Figure 2.5g, h), with a narrow confidence interval on the tail of the BTC for values between 0.0014 m^2 and 0.43 m^2. α was non-identifiable on the majority of the BTC (Figure 2.5e), however, it showed high information content for values between $7.06 \cdot 10^{-5}$ 1/s and 0.0074 1/s at the tail of the BTC (Figure 2.5f). The dynamic identifiability analysis for the BTC of E2 and E3 yielded similar results, with narrow confidence intervals for both A_{TS} and α on the tail of the BTC and no clear trend between information content and discharge (results not shown).

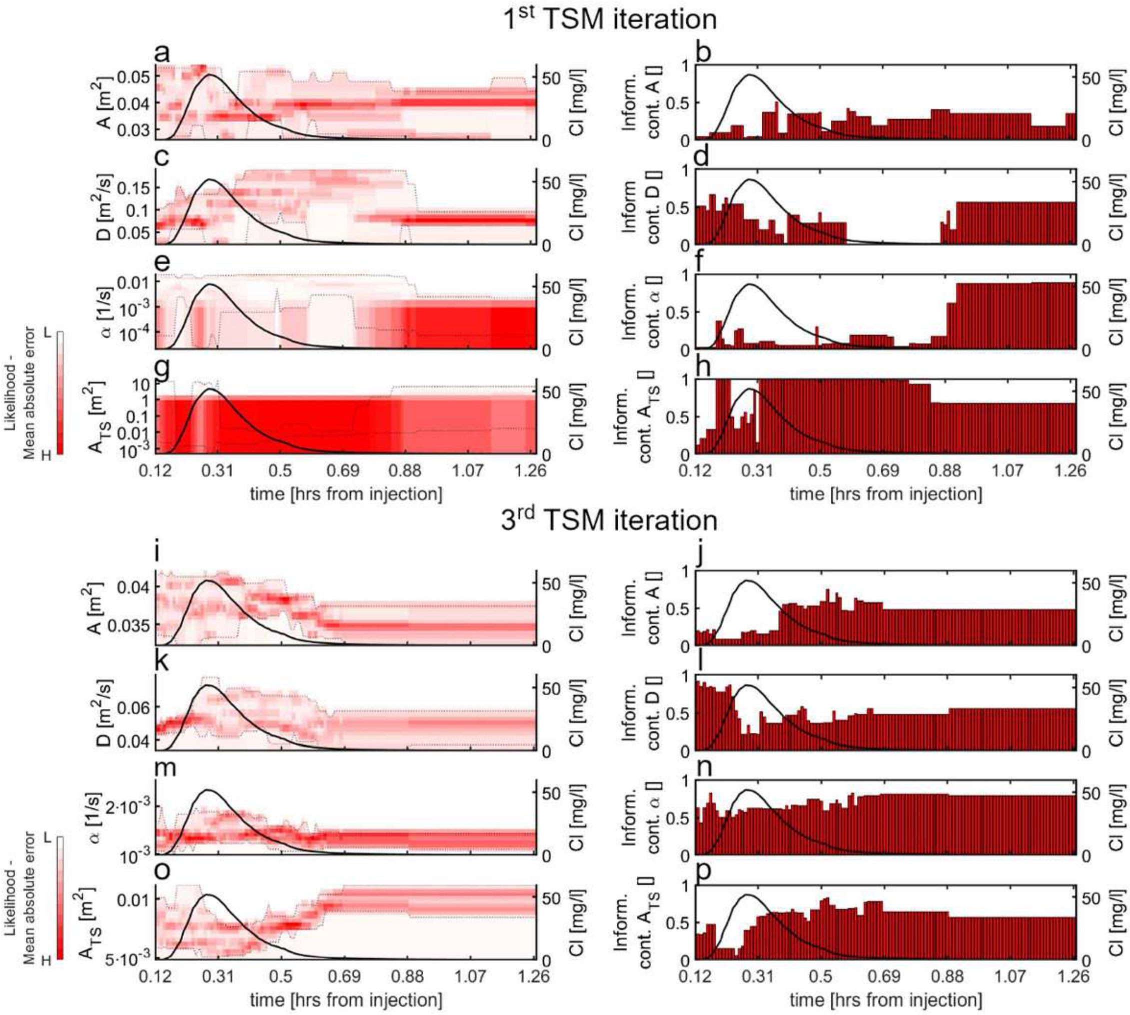

Figure 2.5. Same as Figure 4, but reporting dynamic identifiability results for E1 when velocity was considered equal to v_{peak}.

The dynamic identifiability analysis for the last TSM iteration of E1 indicated that D controls the tail and the rising limb of the BTC while A controls only the tail of the BTC (Figure 2.5i-l). α acted both the rising limb and the tail of the BTC (Figure 2.5m-n) and A_{TS} controlled mostly the tail of the BTC (Figure 2.5o, p). For E2 and E3, results after the last TSM iteration showed lower information content of A_{TS} on the tail of BTC for increasing discharge stages compared to E1, while the information content of α was above 0.33 on the entire BTC (results not shown).

Die approbierte gedruckte Originalversion dieser Dissertation ist an der TU Wien Bibliothek verfügbar.
The approved original version of this doctoral thesis is available in print at TU Wien Bibliothek.
TU Bibliothek, Your knowledge hub, WIEN

2.3.4 Role of the used parameter range and the number of parameter sets for the identifiability of model parameters

When a rather wide parameter range was used (first TSM iteration, green dots Figure 2.2), the performance of the global identifiability analysis was strongly dependent on the chosen number of sampled parameter sets. This can be derived from the strong decrease of the mean and the standard deviation of the top model results with the number of sampled parameter sets N (results reported only for E1, Figure 2.6a). Also, for less than 97,000 parameter sets, the error between model performance using N parameter sets and using 115,000 parameter sets was always above 5% (vertical black lines, Figure 2.6a).

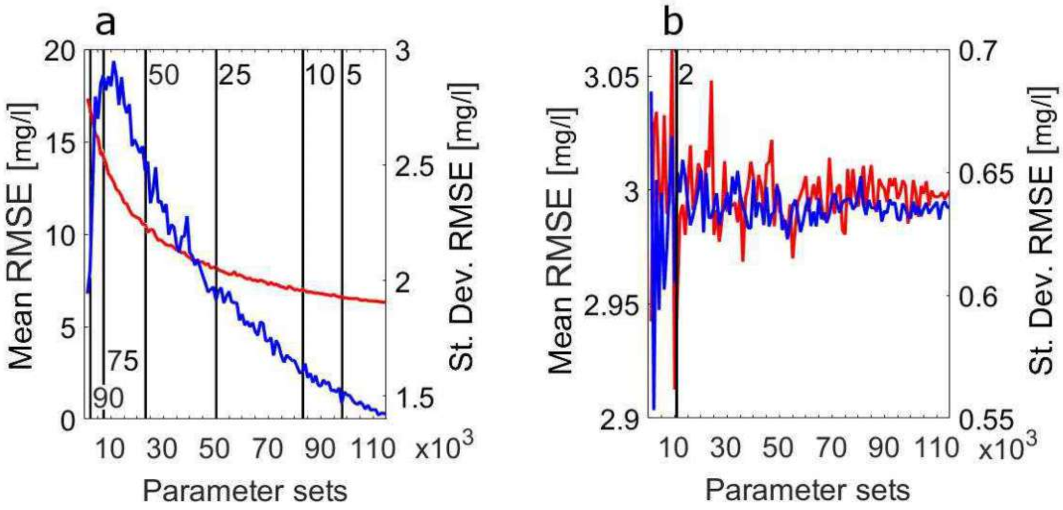

Figure 2.6: Mean (red lines, left axes) and standard deviation (blue lines, right axes) for *RMSE* values relative to the top 10% of the modelling results as a function of the number of parameter sets used in the TSM. The results are reported for the (a) first TSM iteration and the (b) last TSM iteration (E1). Vertical black lines indicate the number of parameter sets needed to have the shown percentage difference between the mean *RMSE* value calculated at the indicated number of parameter sets and at 115,000 parameter sets. Eg: In plot (a) only using at least 50,000 parameter sets there is less than 25% difference in the top 10% *RMSE* values compared to results using 115,000 parameter sets.

Our results showed that TSM results were poorly dependent by the sampled number of parameter sets when the model performance was studied for a narrow parameter range around the peak of performance (last TSM iteration, orange dots Figure 2.2). This was derived by the rather constant mean and standard deviation of the top model results with the number of subset N. Also, for a number of parameter sets N above 11,000 the error between model performance using N parameter sets and using 115,000 parameter sets was always below 2% (vertical black line, Figure 2.6b).

2.3.5 Comparison with OTIS-P and OTIS-MCAT results

Compared to results from our identifiability analysis, outcomes of OTIS-P were consistent with the best parameter sets obtained at the end of the iterative modelling approach (Table 2.2). The parameter sets obtained via OTIS-P (Figure 2.2, 2.3, red vertical dashed line) were approaching the best fitting results obtained at the end of the used iterative approach, regardless of whether flow velocity was considered as a calibration parameter (Figure 2.2) or was considered equal to v_{peak} (Figure 2.3, Table 2.2).

The results of OTIS-MCAT showed low p-values for each model parameter after the K-S test ($p < 0.05$, $K > 0.12$) indicating parameter identifiability. However, compared to our results at the end of the iterative modelling approach, the global identifiability analysis of the OTIS-MCAT showed that the distribution of model parameters did not converge towards univocal and optimal parameter values suggesting that model parameters were rather non-identifiable with the TSM performing less than the ADE (Figure 2.3, green dots).

Table 2.2. Summary of the TSM results. OTIS-MCAT results refer to the case v = vpeak without any successive modification of the parameter via dynamic identifiability analysis results. "Iterative TSM" indicates the best parameter sets obtained after the iterative TSM approach presented in Figure 2.1 and applied for the cases v considered as a calibrated parameter (v = calib.) and when it was considered fixed and equal to vpeak (v = vpeak). The best TSM results are indicated in bold font.

			v [m/s]	A [m^2]	D [m^2/s]	α [1/s]	A_{TS} [m^2]	*RMSE*
E1	ADE		0.0681	0.0395	0.0965	-	-	1.942
	OTIS-P		0.0739	0.0364	0.0637	0.006	0.0074	**0.616**
	OTIS-MCAT		0.0739	0.0351	0.1339	0.0119	0.0051	2.742
	Iterative TSM	$v =$ calib.	0.0728	0.0369	0.0522	0.0013	0.0073	0.723
		$v = v_{peak}$	0.0739	0.0359	0.0534	0.0013	0.0077	0.768
E2	ADE		0.1746	0.054	0.1599	-	-	0.998
	OTIS-P		0.1774	0.0509	0.1151	0.0016	0.0077	0.415
	OTIS-MCAT		0.1774	0.0604	0.1271	0.0137	0.0033	1.443
	Iterative TSM	$v =$ calib.	0.179	0.0526	0.1131	0.0018	0.0067	**0.338**
		$v = v_{peak}$	0.1774	0.0528	0.1154	0.0015	0.0065	0.369
E3	ADE		0.262	0.0874	0.2525	-	-	0.989
	OTIS-P		0.275	0.081	0.1404	0.005	0.0144	**0.254**
	OTIS-MCAT		0.275	0.0849	0.2441	0.0259	0.0073	1.261
	Iterative TSM	$v =$ calib.	0.2861	0.0818	0.1286	0.0064	0.0145	0.269
		$v = v_{peak}$	0.275	0.083	0.1603	0.0037	0.0123	0.311

2.3.6 Variation of transport metrics with increasing identifiability of model parameters

The evaluated transport metrics showed high uncertainty as long the model parameters were poorly or non-identifiable (Figure 2.2, 2.3, green and yellow dots). This was particularly evident after the first and second TSM iterations, when the 100 best-performing parameter sets showed T_{sto} values spanning over nine orders of magnitude (Figure 2.7d-f), while both L_s and q_s spanned over three orders of magnitude (Figure 2.7a-c, g-i). When the model parameters were poorly identifiable, the values of the transport metrics showed clear differences between simulations that were obtained with streamflow velocity as a calibration parameter (Figure 2.7, blue boxplots, first TSM iteration) and between simulations with streamflow velocity set equal to v_{peak} (OTIS-MCAT, Figure 2.7, orange boxplots, first TSM iteration). When v was considered as a calibration parameter, the best-performing parameter sets after the first TSM iteration showed a non-negligible role of transient storage in solute transport for the investigated tracer experiments. This was indicated by the values of L_s (from ~2 km for E1 to ~69 m for E3), by the simulated exchange flux q_s (from 0.06 l/s for E1 to 8.8 l/s for E3), and by the solute residence time in the storage zone T_{sto} (ranging from ~ 140 days for E1 to ~ 15 hrs for E3). Clearly different values for the transport metrics were obtained when v was set equal to v_{peak}. In this case, the results after the first TSM iteration showed a non-negligible exchange flux of the active stream with the transient storage zone (q_s ranged from ~23 l/s for E1 to ~121 l/s for E3), a rather similar L_s for the three tracer experiments (~10 m), and that T_{sto} decreased between the experiments with increasing discharge (from ~12 sec for E1 to ~3 sec for E3).

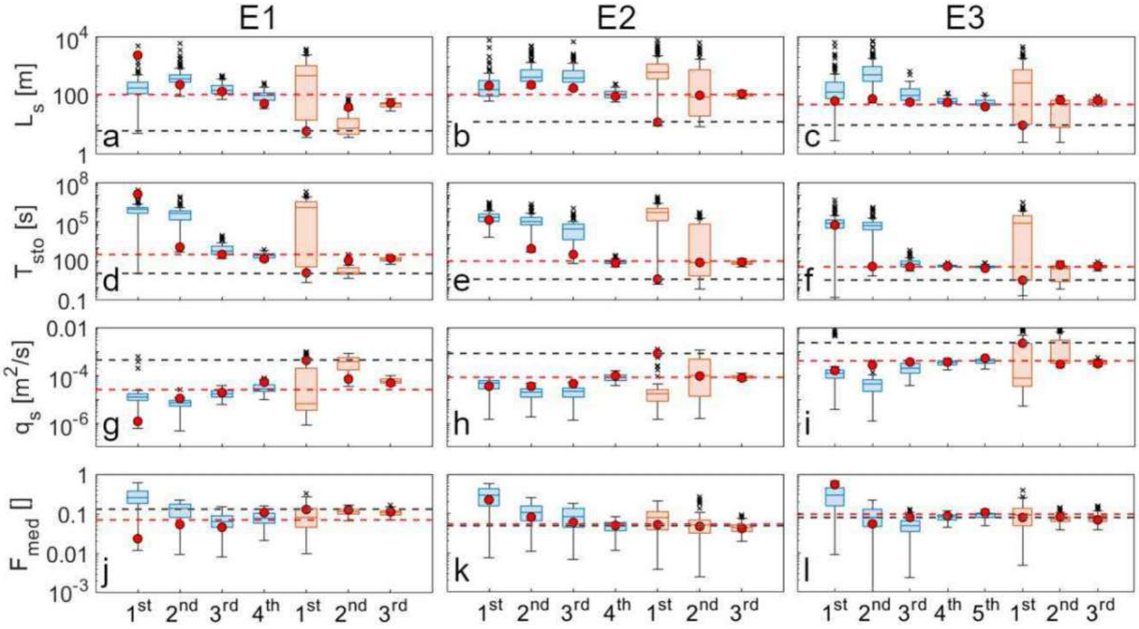

Figure 2.7. Boxplots of the investigated transport metrics for the best 100 parameter sets for the three simulated experiments. (a-c) L_s, (d-f) T_{sto}, (g,i) q_s, (j-l) F_{med}. Results are reported for (a, d, g, j) E1, (b, e, h, k) E2, and (c, f, i, l) E3. On the x-axis, we indicated the n-th TSM iteration. Blue and orange boxplots indicate results when velocity was a varying model parameter and when it was kept fixed and equal to v_{peak}, respectively. Red dots indicate the transport metric values obtained via the parameter sets with lower *RMSE*. The red and the black horizontal dashed lines indicate respectively the transport metric obtained using the OTIS-P results and OTIS-MCAT results (first TSM simulation when velocity was kept fixed and equal to v_{peak}).

However, when the model parameters were identifiable, the transport metrics converged toward constrained values and were consistent with OTIS-P results (Figure 2.7). This was achieved with a calibrated and a fixed (as in the OTIS-MCAT model) streamflow velocity. Results of the last TSM iteration showed that the investigated transport metrics have low dispersion around the median and that the median almost coincides with the result of the best-performing parameter set for the majority of the experiments and of the investigated metrics (Figure 2.7, red dots). The only exception is L_s for E1 when velocity was a varying model parameter, where the median of the best 100 parameter sets reported an L_s 46m higher than the one obtained considering the best-performing parameter set. When all model parameters were identifiable for each of the three tracer experiments, the transport metrics showed increasing q_s (from ~2.7 l/s for E1 to ~23 l/s for E3), increasing L_s (from ~50 m for E1 to ~100 m for E3), and decreasing T_{sto} (from ~150 s for E1 to ~33 s for E3) with increasing mean discharge of the experiments (from E1 to E3). F_{MED} did not change widely

Die approbierte gedruckte Originalversion dieser Dissertation ist an der TU Wien Bibliothek verfügbar.
The approved original version of this doctoral thesis is available in print at TU Wien Bibliothek.
TU Bibliothek WIEN Your knowledge hub

between the TSM iterations since the median of the best-performing 100 parameter sets varied always between 0.04 and 0.2 (Figure 2.7j-l). However, together with q_s, L_S, and T_{sto} transport metrics, the dispersion of F_{MED} values around the median decreased with increasing identifiability of model parameters.

2.4 Discussion

2.4.1 The role of velocity in random sampling approaches for TSM

Our results showed that v interacts with α and A_{TS} in transient storage models. This was particularly evident when v was considered as a calibration parameter, and the non-identifiability of A_{TS} was coupled with identifiable v and α (Figure 2.2, green and yellow dots). On the contrary, A_{TS} was found to be identifiable and α to be non-identifiable when v was fixed equal to v_{peak} (Figure 2.3, yellow dots). It is known that a separate evaluation of the advection-dispersion parameters from the transient storage parameters can result in misestimation of transient storage parameters due to the high parameter interaction (Knapp and Kelleher, 2020). Several studies addressed the identifiability of model parameters, yet, no study so far investigated the role of the flow velocity on the identifiability of α or A_{TS}, and studies rely on a flow velocity equal to v_{peak} in random sampling approaches for TSMs (Ward et al., 2013; Kelleher et al., 2013; Wlostowski et al., 2017; Ward et al., 2017; Ward et al., 2018). The practice of setting v equal to v_{peak} in past studies was justified by the notion that v_{peak} can be considered as a reasonable good approximation for the advection process in the stream channel (Ward et al., 2013; Wlostowski et al., 2017) and by the modelling advantage that assuming v equals v_{peak} would reduce model dimensionality (Knapp and Kelleher, 2020). While reducing the number of model parameters is advantageous for reduced model dimensionality, considering v as a calibration parameter is a needed testing strategy in TSMs. This is because measurement uncertainty is inevitable in determining discharge or flow velocity, thus we don't know how big the effect of measurement uncertainty is on model performance, especially considering parameter interaction. Also, constraining the advection-dispersion parameters A and D already proved to affect the identifiability of the other model parameters (Lees et al., 2000; Kelleher et al., 2013; Ward et al., 2017), but no study assessed the role of velocity on parameter identifiability.

Our results provide valuable guidance for future studies addressing parameter identifiability in TSM. Specifically, our results support the current praxis of considering velocity fixed and equal to v_{peak}, especially when research aims at evaluating the distribution of "behavioural" parameter sets in TSMs (i.e. parameter sets satisfying certain performance thresholds). This is due to the fact that using velocity as calibration parameter leads to the same parameter identifiability compared to the case when velocity is considered fixed at the end of iterative modelling approach (Figure 2.2, 2.3, Table 2.2). Yet, setting velocity equal to v_{peak}, requires a considerably lower amount of computational power due to the lower degrees of freedom of the TSM. However, when research aims to evaluate the control of the model parameters on the shape of the BTC, our results suggest that increasing the model complexity by considering velocity as a varying model parameter can offer more detailed insights into the role of advection-dispersion processes on the tail of the BTC and of the transient storage parameters on the rising limb and peak of the BTC (Figure 2.4, 2.5).

Indeed, our dynamic identifiability analysis underestimated the role of A and A_{TS} on the rising limb and peak of the BTC and overestimated the role of D and α on the rising limb of the BTC for the case v equals v_{peak} compared to the case when v was a calibration parameter (Figures 2.4, 2.5).

The assumption used in previous work of streamflow velocity equalling A_{TS} implies that v_{peak} should encompass the effect of advection on the entire BTC or at least in the rising limb and peak of the BTC (Ward et al., 2013; Kelleher et al., 2013; Wlostowski et al., 2017; Ward 2018). However, when v was used as a calibration parameter, our results showed that v is one of the least meaningful parameters for simulating the peak of the BTC at low discharge (Figure 2.4k, i), while higher information content for v is obtained at higher discharge rates for values larger than v_{peak} at the peak of the BTC (dynamic identifiability plots not shown).

2.4.2 Control of model parameters on the rising limb, the peak, and the tail of the BTC

The results of our dynamic identifiability analysis showed that both the advection-dispersion and the transient storage parameters control solute arrival-time and solute retention in stream channels. This outcome is in contradiction with the common interpretation of model parameters, where it is assumed that the advection-dispersion parameters control the solute arrival time, while transient-storage parameters are assumed to control the tail of the BTC (Bencala, 1983; Bencala and Walters, 1983; Runkel, 2002; Smith, 2005; Bencala et al., 2011). Following this common interpretation of the role of model parameters on the BTC, some authors decomposed the BTC into an advective part and a transient storage part (Wlostowski et al., 2017; Ward et al., 2019). This decomposition allowed them to quantify the role of advection-dispersion and transient storage embedded in the BTC. However, this modelling strategy also implicitly assumes a negligible role of advection-dispersion parameters on the tail of the BTC and of transient-storage parameters on the rising limb and peak of the BTC, which is in not consistent with our findings (Figures 2.4, 2.5, 2.8).

Several studies addressed how different model parameters affect the shape of the BTC and showed partly similar but also contrasting outcomes to our findings (Figure 2.8g-l, Wagner and Harvey, 1997; Wagener et al., 2002; Scott et al., 2003; Wlostowski et al., 2013; Kelleher et al., 2013). Past studies found that the rising limb of the BTC was controlled by the stream channel area A alone (Wagener et al., 2002), by the combination of A and the longitudinal dispersion coefficient D (Wagner and Harvey, 1997; Wlostowski et al., 2013; Kelleher et al., 2013), or by A, D, and A_{TS} (Scott et al., 2003). The peak of the BTC was found to be controlled by advection-dispersion parameters in most past TSM applications (Wagener et al., 2002; Wlostowski et al., 2013; Scott et al., 2003; Kelleher et al., 2013). However, Wagner and Harvey (1997) reported a non-negligible role of the transient storage parameters α and A_{TS} in controlling the arrival time of the peak concentration (Figure 2.8g). Eventually, while the majority of the studies found the transient storage parameters α and A_{TS} to control the tail of the BTC (Wagner and Harvey, 1997; Scott et al., 2003; Wlostowski et al., 2013), results reported by Wagener et al., (2002) and by Kelleher et al. (2013) highlight the role of the stream channel area A on controlling a large portion of the tail of the BTC.

Die approbierte gedruckte Originalversion dieser Dissertation ist an der TU Wien Bibliothek verfügbar.
The approved original version of this doctoral thesis is available in print at TU Wien Bibliothek.
TU Bibliothek Your knowledge hub WIEN

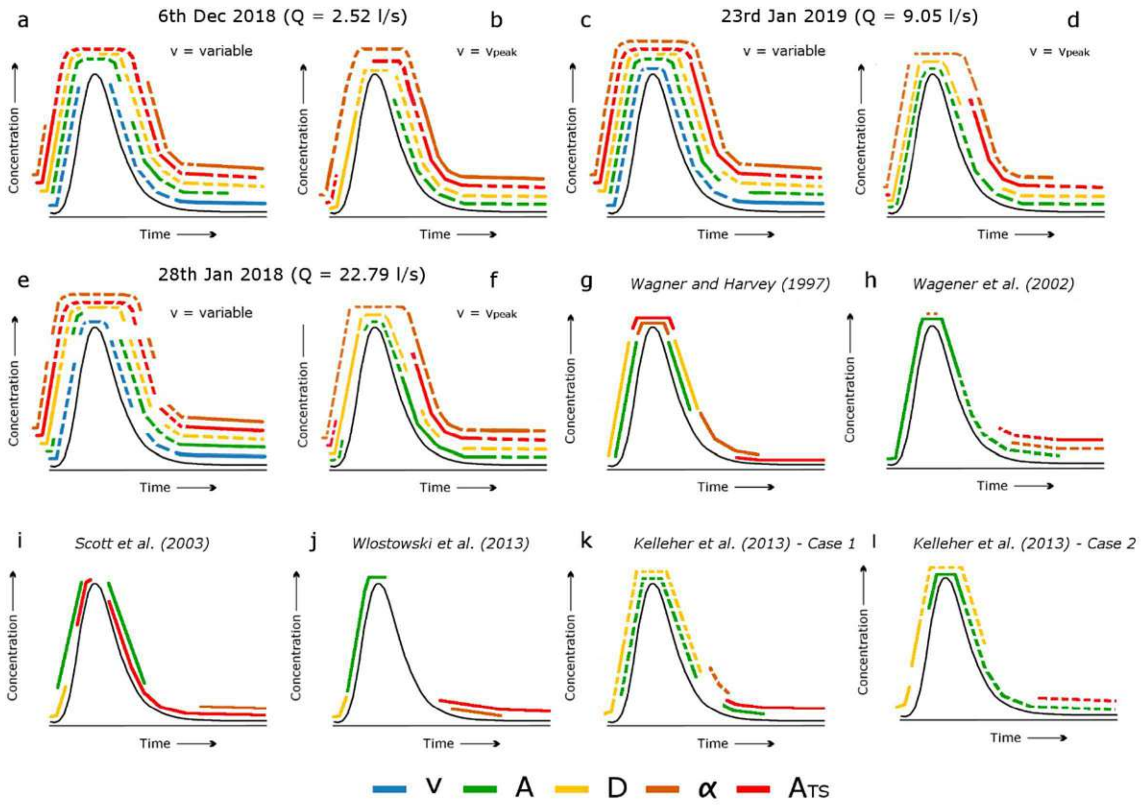

Figure 2.8. Qualitative plots of the TSM parameter influence on different sections of the BTC. (a) and (b) qualitative parameter information content on the BTC for E1, (c, d) E2, and (e, f) E3. In plots (a-f) solid lines indicate an information content above 0.66 while dashed lines indicate an information content between 0.33 and 0.66. (g) Wagner and Harvey, 1997; parameter influence described via sensitivity evaluation (cfr. p. 1733, Wagner and Harvey, 1997), therefore the parameter influence is described using only solid lines. (h) Wagener et al., (2002); Plot (h) has been modified from Figure 7 in Wagener et al., (2002) in order to fit our 0.66 and 0.33 threshold classification in term of information content. (i) Scott et al., (2003); parameter influence described via dimensionless sensitivity (cfr. Table 1 in Scott et al., 2002), therefore the parameter influence is described using only solid lines. (j) Wlostowski et al., 2013; Plot (j) describes the parameter influence after the dynamic identifiability analysis, however information content plots were not reported by the authors, therefore the solid lines indicate the areas for the best-performing parameters as indicated in Figure 2 of Wlostowski et al. (2013). (k) Kelleher et al., (2013) for the case of a dispersive mountain stream (Case 1) and (l) Kelleher et al., (2013) for the case of a small low-flow mountain stream (Case 2); Plots (k) and (l) indicate by solid and dashed lines if the parameters influence the model output by itself or through interactions (cfr. Section 6.1 Kelleher et al., 2013).

The observed identifiability of model parameters in different sections of the BTC in past work and the differences compared to our findings (Figure 2.8a, c, e) might be driven by different physical settings or discharge conditions of the study sites, by the methods used to account for parameters identifiability, by the parameter sampling procedure, or by the strategy used to obtain the best-fitting parameter sets (Wagner and Harvey; 1997; Scott et al., 2003; Kelleher et al., 2013). For example, the identifiability of the TSM to α and A_{TS} is expected to increase for dispersive streams and alluvial stream channels, compared to mountain reaches with low or null hydrologic exchange with the hyporheic zone (Kelleher et al., 2013). However, our analysis also suggests that the different results on the importance of model parameters for certain sections of the BTC (Figure

2.8) could be driven by the selected random sampling approach and the non-identifiability of model parameters.

Plots of the parameter values against the corresponding objective function in Wagener et al. (2002) and the regional sensitivity analysis in Wlostowski et al. (2013) do not indicate parameter identifiability for A_{TS}, D and α. These results together with our identifiability plots when model parameters were poorly identifiable (Figures 2.2, 32., green and yellow plots) suggest that the range and the number of the parameter sets chosen in different studies could have been insufficient to obtain global sensitivity and identifiability of D, A_{TS}, and α parameters. Similar to the results by Wagener et al. (2002) and Wlostowski et al. (2013), our dynamic identifiability analysis showed no influence of A_{TS} on the majority of the BTC, when A_{TS} was non-identifiable (Figure 2.4i, j).

Compared to our results, the different roles of the model parameters in controlling the shape of the BTC in previous studies (e.g. Kelleher et al., 2013) could be driven by the different approaches used for evaluating the sensitivity (i.e. Sobol' sensitivity analysis). However, our results suggest that the number of parameter sets (42,000) selected by Kelleher et al. (2013) might not have been sufficient to obtain identifiability of the model parameters with the rather wide parameter range chosen for their Monte Carlo sampling (Table 2.1). Results by Kelleher et al., (2013) are very similar to our TSM iterations for cases where α was non-identifiable (v equals to v_{peak}, Figure 2.3 yellow dots, dynamic identifiability plots not shown). We also demonstrated that our results after the first and second TSM iterations are not sufficient for interpreting the transient storage process, because of the non-identifiability of the model parameters and the low model performances ($RMSE \geq RMSE_{ADE}$ (Figure 2.3a-l, green and yellow dots).

This study offers significant insights in understanding which model parameter influence the shape of the BTC, suggesting that only behavioural parameter sets should be considered in models aiming to understand the control of model parameters on the rising limb, peak, and tail of the BTC. Future work should address the interaction of model parameters on controlling different sections of the BTC for more complex model formulations (e.g. TSM with two or several transient storage zones, Choi et al., 2002; Bottacin-Busolin et al., 2011).

2.4.3 On the importance of parameter range, parameter sets, and challenges associated to parameter identifiability in TSM

The applied iterative approach was effective in drastically improving parameter identifiability with the increase of TSM iterations. The identifiability of parameters in TSMs is commonly studied via random sampling approaches using between 800 and 100,000 parameter sets sampled from a parameter range spanning several orders of magnitude (Table 2.1). Despite a large number of parameter sets used in previous studies, model parameters were found identifiable only in a few studies (Ward et al., 2017, 2018), while at least one model parameter was found to be non-identifiable in the majority of current TSM studies. Many authors found identifiable A_{TS} coupled with non-identifiable α (Camacho and González, 2008; Kelleher et al., 2013; Wagener et al., 2002; Wlostowski et al., 2013), while other TSM applications found α to be identifiable coupled with non-identifiability for A_{TS} (Kelleher et al., 2019), or α and A_{TS} to be both non-identifiable

Die approbierte gedruckte Originalversion dieser Dissertation ist an der TU Wien Bibliothek verfügbar.
The approved original version of this doctoral thesis is available in print at TU Wien Bibliothek.
TU Bibliothek WIEN Your knowledge hub

Die approbierte gedruckte Originalversion dieser Dissertation ist an der TU Wien Bibliothek verfügbar.
The approved original version of this doctoral thesis is available in print at TU Wien Bibliothek.
TU Bibliothek Your knowledge hub WIEN

(Camacho and González, 2008; Ward et al., 2013; Ward et al., 2017). Our results offer a possible explanation for the observed non-identifiability of model parameters in published work. Our study demonstrated that it is unlikely to reach parameter identifiability via a random sampling approach using less than 100,000 parameter sets when a rather wide range of model parameters is used (Table 2.1, Figure 2.6a). While the range and the order of magnitude of advection-dispersion parameters can be estimated by using the ADE, the ranges where α and A_{TS} are identifiable are not known a-priori and random sampling approaches need to target a parameter range wide enough to capture the distribution of transient storage parameters on their entire feasible range (Ward et al., 2013; Kelleher et al., 2013; Ward et al., 2017). We here proved that using multiple iterations to calibrate TSM parameters is more effective in achieving identifiable TSM parameters than just having a single sampling a large number of parameter sets on a wide parameter range (Figure 2.6). The peak of performance for the transient storage parameters can be so narrow that it can be missed by the random sampling approach or by only a low number of selections when the sampled parameter range spans many orders of magnitude. Similar conclusions have been obtained by Ward et al. (2017), who found by using the OTIS-MCAT model via 100,000 parameter sets that the model parameters were identifiable only for one of the three investigated BTCs. Other studies coupled random sampling approaches with behavioural thresholds to reduce parameter non-identifiability, yet this was done to constrain only the range of A (Kelleher et al., 2013; Ward et al., 2017). Here, we demonstrated the importance of the parameter range over the number of parameter sets in random sampling approaches for TSMs (Figure 2.6). The adopted identifiability analysis was effective in finding behavioural parameter sets after a few iterations regardless of the modelling approach used (OTIS-MCAT as well as considering v as a calibration parameter). Of particular interest is our finding that high information content (> 0.66, e.g. Figure 2.4j. 2.5f) of α and A_{TS} on the tail of the BTC after the dynamic identifiability analysis can be used to reduce the parameter range in successive TSM iterations. This result is in agreement with the recent findings of Rathore et al (2021), who found the tail of the BTC to contain fundamental information for transient storage processes and the parameters describing it.

The adopted iterative approach allowed us to achieve parameter identifiability and to obtain physically realistic transport metrics. However, this approach is based on the specific objective function used (*RMSE*) and on the subjective thresholds to control the refinement of the parameter range for successive iterations (top 10% results for the global identifiability analysis, and information content > 0.66 for the dynamic identifiability analysis). Future work should explore the impact of the selection of the thresholds and different objective functions on the physical realism of the modelling results and the identifiability of the parameters.

Our simulations with OTIS-P resulted in excellent model performances for the investigated BTCs, with low *RMSE* values and with calibrated model parameters comparable to the behavioural parameter populations obtained via our global identifiability analysis (Figure 2.2, 2.3). While the obtained performances of the OTIS-P calibration are certainly specific to the investigated BTCs, the use of OTIS-P alone would have not provided enough information to address the reliability of the obtained model parameters. This, in turn, would have raised concerns about the credibility of the transport metrics obtained, eventually compromising the robustness of the derived physical process involved at the study site. Compared to random sampling approaches coupled with global identifiability analysis, inverse modelling approaches are often considered not as meaningful for interpreting modelling outcomes (Ward et al., 2013; Knapp and Kelleher, 2020). This is because parameters calibrated via inverse modelling might be non-identifiable despite an overall good model performance (Kelleher et a., 2019) and because identifiability analysis informs on a behavioural parameter set which is a preferable and more informative outcome for hydrological models than a single set of parameter values (Beven, 2001; Wagener et al., 2002). Thus, our identifiability analysis over different investigated parameter ranges can offer an explanation about why in past studies identifiability analysis over a probably too large parameter range indicated non-identifiability and lack of convergence with OTIS-P results (Ward et al., 2017).

Eventually, even if random sampling approaches are generally considered more informative than the inverse-modelling approach (Ward et al., 2013; Ward et al., 2017; Ward et al., 2018; Knapp and Kelleher, 2020), our results indicate that random sampling outcomes that show non-identifiability of transient storage parameters should not be used for process interpretation in TSM. This was evident from TSM iterations showing non-identifiability of α and A_{TS}, with the best model performances approaching the $RMSE_{ADE}$ (Figure 2.2, 2.3, black line) indicating an underestimation of the transient storage process with the optimal modelled BTCs having the same (or worse) performances of the ADE.

2.4.4 Implications of identifiable model parameters for hydrologic interpretation of modelling results

Our results demonstrated that poor or non-identifiability of model parameters can result in a wrong hydrological interpretation of the processes controlling solute transport in streams. Additionally, our results showed that with increasing discharge conditions L_s and q_s increased, T_{sto} decreased, and F_{MED} was rather stable for simulations where the model parameters were identifiable (cfr. paragraph 3.2). The low uncertainty and the values of the investigated transport metrics suggested that the transient storage at the experimental site was most probably controlled by in-stream dead zones (Boano et al., 2014; Smettem et al., 2017). Our modelling outcomes are also in line with the physical understanding of the studied stream reach. The study site is equipped with a dense network of groundwater monitoring wells that showed that the stream channel is almost entirely in gaining conditions for the investigated tracer injections with the groundwater gradients pointing toward the stream channel (Bonanno et al., 2021). This is in line with the obtained TSM transport metrics that indicate a very limited or even a lack of hyporheic exchange (e.g. T_{sto} between 33s and 150s, cfr. 2.3.6). Other modelling and experimental studies also outlined that the stream above the study section is dominated by inflow of groundwater or surface water from wetlands (Antonelli et al. 2020a; Glaser et al., 2016, 2020). The observed link of L_s, q_s, and T_{sto} values with discharge (Figure 2.7) also suggested that the transient storage at our site became less important in controlling solute transport with increasing discharge. The decrease of A_{TS} and T_{sto} with increasing discharge has been argued to indicate an increase of groundwater gradients toward the stream channel with a consequent decrease in the hyporheic zone at different study sites (Morrice et al., 1997; Fabian et

Die approbierte gedruckte Originalversion dieser Dissertation ist an der TU Wien Bibliothek verfügbar.
The approved original version of this doctoral thesis is available in print at TU Wien Bibliothek.
TU Bibliothek WIEN Your knowledge hub

Die approbierte gedruckte Originalversion dieser Dissertation ist an der TU Wien Bibliothek verfügbar.
The approved original version of this doctoral thesis is available in print at TU Wien Bibliothek.
TU WIEN Bibliothek Your knowledge hub

modelling approach. Our results showed that the value of stream velocity interacts with the transient storage parameters. Namely, when stream velocity was a randomly sampled calibration parameter (within a physically reasonable range), we found non-identifiable A_{TS} and identifiable α. On the contrary, when stream velocity was assumed to be equal to v_{peak}, A_{TS} was found identifiable and α non-identifiable. We proved that such a non-identifiability of transient storage parameters can result in the modelled BTC having the same performances as the ADE. Our work demonstrates that both transient storage and advection dispersion parameters control the shape of the BTC, when these model parameters are identifiable. This is contrary to previous studies that reported that advection-dispersion parameters control the rising limb and the peak of the BTC and that the transient storage parameters control the tail of the BTC. We also showed that non-identifiable model parameters could severely misestimate the solute retention time in the transient storage zone (T_{sto}) and the exchange flux between the stream channel with the transient storage zone (q_s). The differences of T_{sto} and q_s between identifiable and non-identifiable parameters were up to four and two orders of magnitude, respectively.

The modelling approach in this study constrained the parameter range iteratively. This strategy successfully reduced model dimensionality and allowed us to obtain identifiable model parameters for the three tracer experiments. As a complement to the existing body of literature, our work shows that the non-identifiability of model parameters in past studies might be related to the rather small number of sampled parameter sets compared to the investigated parameter range. The low uncertainty of the model parameters and the derived transport metrics were pivotal for obtaining a robust assessment of the hydrological processes driving the solute transport at the study site. On the contrary, using non-identifiable model parameters, or relying on OTIS-P results alone, would have led to uncertain (in the case of OTIS-P) or rather different (in the case of non-identifiable random-sampled parameters) process interpretation at the study site.

Our study provides enhanced understanding on the relevance of identifiable parameters of TSM models. We also provide insights how parameter calibration without an assessment of their identifiability likely results an unrealistic conceptualization of processes and unrealistic values for different solute transport metrics.

2.6 Acknowledgements

This work was supported by funding from the Luxembourg National Research Fund (FNR) for doctoral training (PRIDE15/10623093/HYDRO-CSI). We would like to acknowledge the financial support of the Austrian Science Fund (FWF) as part of the Vienna Doctoral Programme on Water Resource Systems (DK W1219-N28). We thank Ginevra Fabiani, Adnan Moussa, Laurent Pfister, Rémy Schoppach for their fruitful input and discussions.

Poscia che i cari e lucidi lapilli
ond'io vidi ingemmato il sesto lume
puoser silenzio a li angelici squilli,
udir mi parve un mormorar di fiume
che scende chiaro giù di pietra in pietra,
mostrando l'ubertà del suo cacume.

– Dante Alighieri - Divina Commedia, Paradiso, Canto XX

Die approbierte gedruckte Originalversion dieser Dissertation ist an der TU Wien Bibliothek verfügbar.
The approved original version of this doctoral thesis is available in print at TU Wien Bibliothek.
TU Bibliothek WIEN Your knowledge hub

Chapter 3: Discharge, groundwater gradients, and streambed micro-topography control the temporal dynamics of transient storage in a headwater reach

The present chapter corresponds to the following scientific publication in its original form:
Bonanno, E., Blöschl, G., and Klaus, J.: Discharge, groundwater gradients, and streambed micro-topography control the temporal dynamics of transient storage in a headwater reach, Water Resources Research, in review, 2022.

Key Points:

1. Integrating groundwater data and streambed micro-topography can improve the interpretation of transient storage model results;
2. Parameter interaction in transient storage models increases with discharge;
3. The hyporheic zone and in-stream dead-zone have a decreasing influence on transient storage with higher discharge.

3.1 Abstract

Contradicting interpretations of transient storage modeling (TSM) results in past studies hamper the understanding of how hydrologic conditions control the transport of solutes in streams. In this study, we estimate transient storage model parameters from 31 tracer experiments in the Weierbach stream in Luxembourg. We interpret the change of the parameters with discharge in terms of changing size of the hyporheic zone and the submerged area of streambed sediments. During low discharge, transient storage at the study site is controlled by both in-stream transient storage and hyporheic exchange processes. This is because of the large extent of the hyporheic area receiving water from the stream channel and the relatively low water level compared to the measured size of the slate fragments on the streambed. The hyporheic zone has a decreasing influence on transient storage with increasing discharge due to the relatively lower localized water losses from the stream channel to the adjacent groundwater. The higher stream water level causes the in-stream dead-zones to get submerged and become part of the advective channel. However, higher stream water levels and water velocities also caused an increase of turbulence in the water column, suggesting that transient storage is mainly controlled by eddies generated by the water friction with the streambed sediments under high discharge conditions. The understanding of the relative importance of hyporheic area and dead zones for transient storage obtained here assists in clearer process interpretations and in estimating TSM parameters more accurately.

The need to understand how different hydrological processes can influence water chemistry, biological activity, and the ecological richness of stream networks has motivated a range of studies over the past 30 years (Boulton et al., 2010; Stanford & Ward, 1988; Ward, 2016). Here, TSMs have been adopted to characterize hyporheic exchange and in-stream water storage in a multitude of streams (Bencala et al., 2011; Bencala & Walters, 1983; Butturini & Sabater, 1999; Gooseff et al., 2005, 2008; Hart et al., 2002; Ward et al., 2018; Wörman, 1998). TSM assumes a uniform, steady-state, 1-D flow modeled via the advection-dispersion equation (ADE) with a first-order mass transfer exchange α between the advective flow channel and a finite-sized storage zone with A_{TS} dimensions (Bencala & Walters, 1983). Knowing how the transient storage parameters α and A_{TS} change with different hydrologic conditions is crucial as larger transient storage zones and longer residence times are key factors in enhancing nutrient cycling (Argerich et al., 2011) and degrading pollutants (Moser et al., 2003) in stream networks. The simplified, yet informative structure of the TSM can thus offer valuable insights into the potential development of hot spots and hot moments that control water quality in surface waters (Krause et al., 2017; Smith, 2005).

Despite the pressing need to decipher the role of different hydrological processes and conditions on solute transport in streams, current research led to a collection of idiosyncratic studies with conflicting model predictions and interpretations (Ward & Packman, 2019). Higher discharge have been linked to higher (Bencala & Walters, 1983; Lees et al., 2000; Schmid et al., 2010; Ward et al., 2018; Wlostowski et al., 2013) and lower (Harvey et al., 1996; Karwan & Saiers, 2009; Martí et al., 1997; Morrice et al., 1997; Valett et al., 1996; Ward et al., 2017; Wondzell, 2006) values of the transient storage area A_{TS}, or to show no clear relationships (Edwardson et al., 2003; Fabian et al., 2011; Hall et al., 2002; Jin & Ward, 2005; McKnight et al., 2004; Ward, Payn, et al., 2013; Zarnetske et al., 2007). Similarly, the rate of exchange α between the advective flow channel with the transient storage zone was higher (Fabian et al., 2011; Gooseff et al., 2003; Hart et al., 1999; Harvey et al., 1996; Lees et al., 2000; Schmid et al., 2010; Ward et al., 2018; Wondzell, 2006), lower (González-pinzón et al., 2015; Karwan & Saiers, 2009; Ward, Kelleher, et al., 2017), or showed no clear relationship with discharge (Bencala et al., 1990; Bencala & Walters, 1983; Butturini & Sabater, 1999; D'Angelo et al., 1993; Edwardson et al., 2003; Gooseff et al., 2013; Hall et al., 2002; Jin & Ward, 2005; Legrand-Marcq & Laudelout, 1985; Martí et al., 1997; McKnight et al., 2004; Morrice et al., 1997; Scott et al., 2003; Ward, Payn, et al., 2013).

The inconsistency in the relation between the values of TSM parameters with discharge in previous studies (Table 3.1) might derive from the specific characteristics of the different study sites. For example, stream channels with a relatively high hydraulic conductivity of the streambed material (sand and gravel) would allow the inflow of water from the stream toward the adjacent groundwater with higher discharge (Dudley-Southern & Binley, 2015), leading to a more pronounced tail of the BTC (Schmadel et al., 2016). In contrast, stream channels confined by fresh bedrock or characterized by material with low hydraulic conductivity would exhibit a rather reduced hyporheic zone area at high discharge and are thus more likely to show a reduction in transient storage area with higher discharge (Wondzell, 2011). Nevertheless, conflicting or absent relationships between TSM parameters and stream discharge could also be due to limitations that are common in studies

Die approbierte gedruckte Originalversion dieser Dissertation ist an der TU Wien Bibliothek verfügbar.
The approved original version of this doctoral thesis is available in print at TU Wien Bibliothek.
TU Bibliothek WIEN Your knowledge hub

investigating solute transport in streams with tracer experiments (Table 3.1). First, the calibration of parameters in TSM has been performed iteratively to visually fit the modeled BTC over the observed BTC (Bencala et al., 1990; Bencala & Walters, 1983; D'Angelo et al., 1993; Legrand-Marcq & Laudelout, 1985; Valett et al., 1996), or by inverse modeling (Edwardson et al., 2003; Fabian et al., 2011; Gooseff et al., 2013; Jin & Ward, 2005; Lees et al., 2000; McKnight et al., 2004; Schmid et al., 2010; Wondzell, 2006). However, the identifiability of model parameters has generally not been taken into account in most TSM studies (Table 3.1), leading to a lack of certainty about the modeling results and their physical interpretation. (Knapp & Kelleher, 2020). When TSM parameters are non-identifiable, they are highly interdependent, meaning that changes in one parameter would be balanced by a proportional change of one or more other parameters leading to the same model performances (Camacho & González, 2008; Kelleher et al., 2013; Wagener et al., 2002). Identifiability is a crucial issue for the interpretation of TSM results, as most studies that have addressed the identifiability of TSM parameters have found that they were non-identifiable (Kelleher et al., 2019; Wagener et al., 2002; Camacho & González, 2008; Ward, Kelleher, et al., 2017; Wlostowski et al., 2013). Non-identifiability of TSM parameters does not only affect model performance, but it can result in the modeled BTC mimicking the advection-dispersion equation, leading to a misinterpretation of the processes governing transient storage at the study site (Bonanno et al., 2022). A growing number of studies addressed parameter identifiability in TSMs via random sampling approaches (Kelleher et al., 2019; Ward et al., 2017, 2018; Knapp & Kelleher, 2020; Table 3.1). However, no study to date has directly investigated the identifiability of the TSM parameters under multiple hydrologic conditions, which may improve our understanding of why TSM parameters were identifiable in some studies (Ward et al., 2018; Ward, Kelleher, et al., 2017) and not in others (Camacho & González, 2008; Kelleher et al., 2013; Wagener et al., 2002; Wlostowski et al., 2013; Ward, Kelleher, et al., 2017).

There is also a second limitation that may cause an unclear correlation between TSM parameters and discharge, thus hindering the physical interpretation of the model results, namely the scarcity of information about the stream reach and the relatively small number of tracer experiments. Studies analyzing a section of a stream under different hydrological conditions, or studying higher stream discharge at successive monitoring stations, rarely investigated more than four stages of discharge (Table 3.1) with the tracer experiments being mostly conducted at baseflow conditions (Ward, 2016). A relatively low number of investigated discharge stages hampers the ability to observe a robust relationship between discharge and α and A_{TS}, resulting in a poor understanding of the processes controlling transient storage in stream reaches (Ward & Packman, 2019). Investigating the link between TSM parameters across different discharge stages is also not enough for associating specific hydrological processes with certain hydrologic conditions. This is because higher discharge can cause larger and lower hyporheic exchange and in-stream transient storage depending on the stream morphology and the groundwater gradients at the study site (Jin & Ward, 2005; Bonanno et al., 2021; Dudley-Southern & Binley, 2015; Gooseff, Bencala, et al., 2008; Martí et al., 1997; Schmid et al., 2010). A clearer perception of the physical processes of stream reaches fosters a robust interpretation of TSM results. As an example, the measurements of the groundwater levels adjacent to the stream channel can be used to infer if the near-stream groundwater is receiving stream water, thus offering valuable information on the potential development of hyporheic zones at the study site (Bonanno et al., 2021; Voltz et al., 2013; Wondzell, 2006). Likewise, the size and distribution of the sediments making the streambed topography can be a crucial resource for the interpretation of TSM results, since streambed sediments and in-stream obstructions can create recirculation zones resulting in a non-negligible role for in-stream transient storage (Hart et al., 1999; Montgomery & Buffington, 1997; Jackson et al., 2013). Without a comprehensive knowledge of the groundwater levels and the streambed topography, it is difficult to distinguish whether a certain transient storage area can be related to a specific transient storage process or whether it is simply the result of a mathematical fit of the TSM parameters without a realistic role for solute transport at the study site.

In this manuscript we address the following research questions:

i. Does the identifiability of TSM parameters change with discharge?
ii. How do transient storage processes change under different hydrologic conditions?

To answer these questions and to overcome the limitations mentioned above in TSM studies we performed 31 in-stream tracer experiments and we: (i) investigated the identifiability of TSM parameters by combining global identifiability analysis with dynamic identifiability analysis in an iterative approach obtaining identifiable TSM parameters (cf. Bonanno et al., 2022); (ii) we recorded the groundwater elevation at the study site through a groundwater monitoring network of 43 wells that allowed us to infer the extent of the hyporheic zone during each experiment; (iii) we obtained the micro-topography of the streambed via a laser scan and we compared the distribution of the height of the slate fragments in the streambed to the surface water level to infer the role of in-stream transient storage in different hydrologic conditions.

Table 3.1. Relationships between transient storage parameters α and ATS and stream discharge Q in published literature. (+) and (–) symbols indicate respectively positive and negative relationships between stream discharge with the transient storage parameters α and ATS. The "unclear" term means that both positive and negative relationships have been observed between discharge and α and ATS. The slash symbol (/) indicates no results, due to non-reported results or a null evaluation of the parameter. When a study investigated multiple stream reaches, we reported only the reaches investigated at different hydrologic conditions. We here also reported studies using only one tracer injection, but where higher discharge was studied via multiple reaches with tracer measurement location located at increasing distance from the tracer injection point.

Study	**Site name**	**Number and/or name of the sub-reaches**	**Number of experiments per reach**	**A_{TS} vs Q**	**α vs Q**	**Fitting**	**Identifiability analysis**
Legrand-Marcq & Laudelout, 1985	Rieu d'Ostenne	1	13	(–)	Unclear	Visual	No
Bencala & Walters, 1983	Uvas Creek	5	1	(+)	Unclear	Visual	No

Bencala et al., 1990	Snake river (upstream Deer creek)	5	1	Unclear	Unclear	Visual	No
	Snake river (downstream Deer creek)	3	1	Unclear	Unclear	Visual	No
D'Angelo et al., 1993	Artificial streams	2 (Dogwood and Oak)	2 (summer - winter)	/	/	Visual	No
	1st-order site	2 (Pine and Hardwood)	2 (summer - winter)	(+)	(+)		
	Gradient site	4 (from 1st to 4th order)	1 (summer)	Unclear	Unclear		
	5th Order site - unconstrained	2 (reaches 4 and 7)	2 (summer - winter)	(–)	Unclear		
	5th Order site - constrained	2 (reaches 1, 2, 3, 5, 6)	1 (summer)	Unclear	Unclear		
Valett et al., 1996	Gallina creek	1	4	(–)	/	Visual	No
Harvey et al., 1996	St. Kevin Gulch	1	2	(–)	(+)	Nonlinear least squares regression	No
Morrice et al., 1997	Gallina Creek	1	4	(–)	Unclear	Visual	No
Martí et al., 1997	Sycamore Creek	1	8	(–)	Unclear	Visual	No
Butturini & Sabater, 1999	Riera Major stream	1	15	Unclear	Unclear	Direct fitting (sensu Hart, 1995)	No
Hart et al., 1999	West Fork of Walker Branch	1	11 (^{3}H) and 9 (Cl$^-$)	Unclear	(+)	Direct fitting (sensu Hart, 1995)	No
Lees et al., 2000	Mimram River	2	1	(+)	(+)	OTIS-P (sensu Runkel, 1998)	Non-unique convergence of α and A_{TS} parameters.
Hall et al., 2002	Hubbard Brook Experimental Forest	1 (Bear brook)	4	Unclear	Unclear	Direct fitting (sensu Hart, 1995)	No
		1 (Cone Pond Outlet)	2	(+)	(+)		
		1 (Hubbard brook)	3	Unclear	Unclear		
		1 (Paradise brook)	2	(+)	(+)		
		W2 stream	3	(+)	Unclear		

		W3 stream	6	Unclear	Unclear		
		W4 stream	3	Unclear	Unclear		
		W5	3	(+)	Unclear		
		W6	5	Unclear	Unclear		
		West inlet to mirror lake	3	Unclear	Unclear		
Edwardson et al., 2003	Imnavait creek	Site 1	2	(+)	(–)	OTIS-P (sensu Runkel, 1998)	No
		Site 2	2	(–)	(+)		
	Blueberry Creek	Site 1	4	Unclear	(+)		
		Site 2	4	Unclear	Unclear		
	Toolik Inlet Stream	Site 1	2	(+)	(+)		
	Oksrukuyik Creek	Site 1	2	(–)	(+)		
	Kuparuk River	Site 1	6	Unclear	Unclear		
		Site 2	6	Unclear	Unclear		
Gooseff et al., 2003	Lookout Creek watershed	LO411	2	(–)	(+)	UCODE plus manual modification of the parameters to visually match the tail of the BTC.	No
Scott et al., 2003	Uvas Creek	5	1	(–)	Unclear	UCODE (unable to calibrate α and A_{TS} for two over five BTCs)	No
McKnight et al., 2004	McMurdo Dry Valleys (Green Creek)	4	1	Unclear	Unclear	OTIS-P (sensu Runkel, 1998)	No
Jin & Ward, 2005	Payne Creek	1	9 (constant-rate)	Unclear	Unclear	OTIS-P (sensu Runkel, 1998)	No
			6 (slug)	Unclear	Unclear		
Wondzell, 2006	WS1	1 (Upper)	2	(–)	(+)	OTIS-P (sensu Runkel, 1998)	No
		1 (Lower)	2	(–)	(+)		
	WS3	1 (Upper)	2	(–)	(–)		
		1 (Lower)	2	(–)	(+)		
Zarnetske et al., 2007	Northern foothills of Alaska's Brooks Range	1 (A2)	3	(+)	(+)	STAMMT-L (sensu Haggerty et al., 2002)	No
		1 (P1)	4	Unclear	(+)		
		1 (AP)	4	Unclear	(+)		

Karwan & Saiers, 2009	Wangum Brook	1	3 (2)	(–)	(–)	Levenberg-Marquardt nonlinear least squares algorithm (unable to calibrate α and A_{TS} under high discharge stages)	No
Schmid et al., 2010	Mödlingbach	1	12	(+)	(+)	OTIS-P (sensu Runkel, 1998)	No
	Torrente Lura	S-I	4	(+)	(+)		
		S-II	7	(+)	(+)		
		D-G	5	(+)	(+)		
Fabian et al., 2011	Prieta Creek	1	3	Unclear	(+)	OTIS-P (sensu Runkel, 1998)	No
Mason et al., 2012	Silver Bow Creek	1	58	/	/	/	Identifiability analysis – α and A_{TS} non-identifiable
Ward et al., 2013	Stringer Creek	28	4	Unclear	Unclear	OTIS + Monte Carlo simulations (100'000)	Identifiability analysis – α and A_{TS} non-identifiable
Gooseff et al., 2013	Uvas Creek	5 (+10 sub-reach combinations)	1	(+)	Unclear	OTIS + UCODE (sensu Scott et al., 2003)	No (suspected non-identifiability for some results)
González-pinzón et al., 2015	Shaver Creek	2	1	(+)	(–)	OTIS + Shuffled Complex Evolutionary algorithm	No
Wlostowski et al., 2017	Alaska's North Slope	I8 inlet	4	Unclear	Unclear	OTIS + Shuffled Complex Evolutionary algorithm	No
		Peat inlet	3	(+)	(+)		
Ward et al., 2017	Tenderfoot Creek	2 (100 m – 2500 m)	1	(–)	(–)	OTIS + Monte	Identifiability analysis –

	Experimental Forest					Carlo simulations (100'000)	D, A, α and A_{TS} non-identifiable
Ward et al., 2018	Fawn River	Unrestored reach	4	(+)	(+)	OTIS + Monte Carlo simulations (100'000)	Identifiability analysis – D, A, α and A_{TS} identifiable
		Restored reach	4	(+)	(+)		

3.4 Methods

3.4.1 Study site

The study reach is located in western Luxembourg, downstream of the Weierbach experimental catchment (49°49'38''N, 5°47'44''E) (Hissler et al., 2021). The stream reach is 55 m long and it is characterized by a riffle morphology, has an average slope of ≃6%, is unvegetated, and consists of deposited colluvium of fragmented slates over a fractured bedrock layer (Bonanno et al., 2021, Figure 3.1). Previous work outlined the occurrence of several hydrological processes controlling stream water generation in the Weierbach catchment. The hillslopes at the study site are characterized by a regolith layer with a relatively high hydraulic conductivity compared to the fractured bedrock layer beneath (Glaser et al., 2016, 2020). The subsurface structure does not promote shallow lateral flow toward the stream channel (Klaus & Jackson, 2018), and precipitation water percolates vertically toward the groundwater table in the fractured bedrock (Rodriguez & Klaus, 2019). The water movement through and above the fractured bedrock from the hillslopes maintains a rather steady and shallow groundwater level in the near-stream domain throughout the year (Fabiani et al., 2021), and the organic soil areas composing part of the riparian area are almost constantly saturated (Bonanno et al., 2021). Discharge is thus generated by both a fast- and a slow-response to precipitation events. The fast-response is controlled by the surface runoff of event-water over the saturated organic soil in the riparian zone toward the stream channel (Wrede et al., 2015; Antonelli et al., 2020a; Bonanno et al., 2021). The slow-response occurs when the amount of water from precipitation events exceeds the storage capacity at the hillslope. When this happens, the groundwater is laterally redistributed over the fractured bedrock from the hillslopes toward the stream channel causing an increase in discharge and a double-peak behavior in the hydrograph (Martínez-Carreras et al., 2016; Bonanno et al., 2021).

3.4.2 Tracer experiments

We performed a total of 31 in-stream instantaneous tracer experiments between December 2018 and June 2021. For each experiment, we prepared a NaCl solution using 2 l of stream water and an amount of NaCl between 50 g and 250 g (Table 3.2). We selected slug injections over constant-rate injections to minimize the influence of varying discharge on the BTC measurements (Ward, Gooseff, et al., 2013) and because they contain the same information as a constant-rate injection for conservative tracers (Gooseff, Payn, et al., 2008; Payn et al., 2008). We injected the tracer

Die approbierte gedruckte Originalversion dieser Dissertation ist an der TU Wien Bibliothek verfügbar.
The approved original version of this doctoral thesis is available in print at TU Wien Bibliothek.
TU Bibliothek WIEN Your knowledge hub

solution in a turbulent pool at the beginning of the study reach, assuring complete mixing. We measured electric conductivity (EC) at the end of the investigated reach (55 m from the injection point) via a portable conductivity meter (WTW TetraCon 3310) providing a resolution of 0.1 µS/cm from 0 µS/cm to 199 µS/cm and 1 µS/cm from 200 µS/cm to 1999 µS/cm (accuracy ± 0.5% of the value and temperature automatically compensated). Calibration of EC to chloride concentration was conducted in the laboratory using a known volume of water sampled at the measurement location before the tracer injection.

Table 3.2. List of the in-stream instantaneous tracer injections, date, discharge from dilution gauging, and amount of injected NaCl.

ID number	Date	Discharge Q [l/s]	Amount of NaCl [g]
E01	06th December 2018	2.5	100
E02	11th December 2018	14.0	100
E03	08th January 2019	4.5	100
E04	11th January 2019	3.8	100
E05	23rd January 2019	9.0	100
E06	24th January 2019	7.9	100
E07	28th January 2019	22.8	100
E08	04th February 2019	17.0	100
E09	05th February 2019	17.1	100
E10	08th February 2019	15.9	100
E11	25th February 2019a	5.3	100
E12	25th February 2019b	4.9	100
E13	25th February 2019c	4.7	100
E14	08th March 2019	28.6	100
E15	11th March 2019	25.2	100
E16	05th February 2020	75.0	100
E17	14th February 2020	36.7	250
E18	06th May 2020	1.3	150
E19	18th June 2020	0.9	100
E20	22nd June 2020	0.4	100
E21	06th November 2020	4.7	100
E22	29th March 2021a	5.1	100
E23	29th March 2021b	5.0	100
E24	30th March 2021a	4.8	100
E25	30th March 2021b	4.7	100
E26	31st March 2021a	4.7	50
E27	31st March 2021b	4.6	100
E28	31st March 2021c	4.6	150
E29	31st March 2021d	4.1	200
E30	11th June 2021a	2.8	100
E31	11th June 2021b	2.5	100

Die approbierte gedruckte Originalversion dieser Dissertation ist an der TU Wien Bibliothek verfügbar.
The approved original version of this doctoral thesis is available in print at TU Wien Bibliothek.
TU Bibliothek WIEN Your knowledge hub

Die approbierte gedruckte Originalversion dieser Dissertation ist an der TU Wien Bibliothek verfügbar.
The approved original version of this doctoral thesis is available in print at TU Wien Bibliothek.
TU Bibliothek WIEN Your knowledge hub

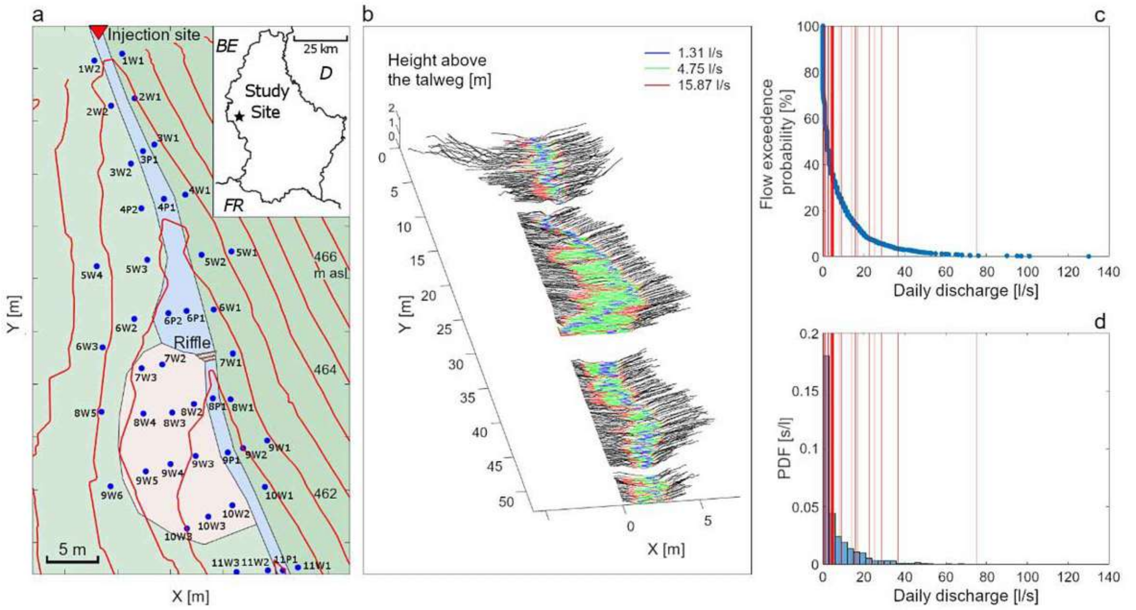

Figure 3.1. (a) Study reach and location of the wells and piezometers. The Y direction corresponds to the direction of the geographic north; thus the stream reach defines an "east footslope" on the right side of the map, and a "west footslope", on the left side of the map. (b) Transects of the stream channel were extracted from four LIDAR scans at a 1 cm resolution and at 15 cm distance between each other. The white areas between the scans are missing data due to the local presence of water and shadow zones. Blue, green, and red lines indicate the length of the wetted perimeter in each transect for the three reported discharge stages. (c) Flow duration curve and (d) probability density function for the recorded discharge at the Weierbach outlet for the period January 2018 – December 2021, 55 m upstream of the study site. The vertical red lines indicate the discharge stages investigated during the slug tracer injections.

3.4.5 Formulation of the Transient Storage Model

The formulation of the TSM reads (Bencala & Walters, 1983):

$$\left\{\frac{\partial C}{\partial t} = -v\frac{\partial C}{\partial x} + \frac{1}{A}\frac{\partial}{\partial x}\left(AD\frac{\partial C}{\partial x}\right) + \alpha\left(C_{TS} - C\right) \quad \frac{\partial C_{TS}}{\partial t} = -\alpha\frac{A}{A_{TS}}\left(C_{TS} - C\right)\right.$$

Eq. 1

where t is time [T], x is the distance from the injection point along the stream reach [L], A [L^2] is the stream discharge cross-sectional area, v [L/T] is the flow velocity, D [L^2/T] is the longitudinal dispersion coefficient, C and C_{TS} are the concentration of the observed tracer in the stream channel and in the storage zone, respectively [M/ L^3], α [1/T] is the exchange coefficient between the stream channel and the storage zone and A_{TS} [L^2] is the area of the transient storage zone. Three primary assumptions are associated with the formulation of the TSM (Harvey et al., 1996): (i) negligible transport in the hyporheic zone parallel to the stream, (ii) exponential residence time distribution (RTD) in the transient storage zone, and (iii) in-stream water storage and hyporheic exchange are jointly described by the transient storage parameters α and A_{TS}.

3.4.6 Calibration and identifiability of Transient Storage Model parameters

TSM parameters are usually obtained via visual fitting or inverse modeling approaches, such as OTIS-P (Table 3.1). Despite the good model performances that can be obtained from inverse modeling approaches, the parameters might be non-identifiable (Kelleher et a., 2019) and may not capture the underlying processes well. Thus, several authors advocated the identification of a "behavioral" parameter population in TSMs via identifiability analysis (i.e. parameter sets satisfying certain performance thresholds) since this is a preferable and more informative outcome than a singular best set of parameter values (Beven, 2001; Kelleher et al., 2019; Wagener et al., 2002; Wagener et al., 2002; Ward et al., 2017, 2018; Wlostowski et al., 2013).

The "identifiability" term is used to indicate how certain a parameter is in a model application. If a good model performance occurs in only a relatively narrow parameter interval compared to the distribution of its possible values, then the parameter can be considered identifiable. On the contrary, if a good model performance is distributed across a relatively large parameter interval compared to the distribution of its possible values, then the parameter can be considered non-identifiable (Ward et al., 2017). In studies where the identifiability of TSM parameters has been investigated via random sampling approaches, α and A_{TS} have proved to be rarely identifiable (Kelleher et al., 2013; Ward et al., 2013, 2017).

We obtained TSM parameters and their identifiability via a novel iterative modeling approach that combines random sampling with global identifiability analysis and dynamic identifiability analysis (Bonanno et al., 2022). The used iterative modeling approach requires a certain number of parameter sets and the corresponding model performance when compared to the observed BTC. By "parameter set" we refer to a specific combination of v, A, D, α, and A_{TS} parameter values, while by "parameter space" we refer to the range of a parameter between the selected lower and the upper bounds in the random parameter sampling. Model performance was evaluated with the Root Mean Squared Error objective function (*RMSE*) commonly used in solute-transport studies (Liao et al., 2013; Ward, Payn, et al., 2013; Ward, Schmadel, et al., 2017; Wlostowski et al., 2017). We selected *RMSE* because it allows consistency between the dynamic identifiability analysis and global identifiability analysis used in the iterative modeling approach (Wagener et al., 2002; Bonanno et al., 2022). Global identifiability analysis addresses the identifiability of the TSM parameters using as model performances the *RMSE* evaluated on the entire BTC, while the dynamic identifiability analysis addresses the identifiability of the TSM parameters over time, meaning that identifiability is studied along a moving window over the BTC (Wagener et al., 2002).

Global identifiable parameters satisfy the following criteria (Ward et al., 2017; Kelleher et al., 2019; Bonanno et al., 2022): (i) univocal peak of performance in parameter vs objective function plots; (ii) cumulative distribution function (CDF) corresponding to the best 0.1% of the model results deviating from the 1:1 line and from parameter CDF corresponding to the best 10% of the model results; (iii) the two-sample Kolmogorov-Smirnov (K-S) test indicating a statistically relevant difference in the CDF corresponding to the bets 0.1 and 10% results ($p \leq 0.05$):

$$[K,p] = max|F(P_{0.1}) - F(P_{10})| \qquad \text{Eq. 2}$$

Where $F(P_{0.1})$ and $F(P_{10})$ are the cumulative distribution function of a parameter P respectively for the best 0.1% and the best 10% of the model results. Dynamic identifiability analysis indicates the 90% confidence interval of a parameter compared to the considered parameter space over different sections of the BTC. The evaluation of one minus the width of the 90% confidence interval over the entire parameter range indicates the "information content" of a certain parameter over the BTC. Information content values close to 1 indicate stronger parameter identifiability in that investigated section of the BTC compared to lower information content values (Wagener et al., 2002; Wagener et al., 2002; Bonanno et al., 2022).

Our approach is iterative, meaning that a successive TSM iteration depends on the results of the identifiability analysis of the previous iteration. This is similar to previous studies that used a random sampling approach combined with behavioral thresholds (Kelleher et al., 2013; Ward, Kelleher, et al., 2017). For each iteration, we randomly sample 35,000 parameter sets via Latin Hypercube sampling. This number of parameter sets was chosen because 35,000 parameter sets were proven to have always less than 2% error in the mean and standard deviation of the top 10% results compared to 115,000 parameter sets, when the identifiability conditions are met (Bonanno et al., 2022). The first TSM iteration evaluated the TSM performance over a relatively large parameter space initially defined by literature values and the result of the best-fitting ADE against the observed BTC (Table 3.1, Bonanno et al., 2022). The following iterations rely on a constrained parameter space depending on the best-performing upper and lower bound obtained by the results of the global and dynamic identifiability analysis. The dynamic identifiability analysis is used to provide information for reducing the upper or lower bound for α and A_{TS} since it indicates the parameter limits with high identifiability (information content > 0.66) on the BTC tail (Bonanno et al., 2022).

We finalized the iterative modeling procedure once all model parameters (v, A, D, α, and A_{TS}) satisfied the global identifiability conditions defined above in their selected parameter space. We repeated the sampling of 35,000 parameter sets over the parameter space that indicated parameter identifiability until we obtained at least 1,000 parameter sets that perform better than the ADE ($RMSE < RMSE_{ADE}$). This was done to: (i) obtain a statistically relevant number of parameter sets with satisfactory model performances; and (ii) only TSM parameter sets with $RMSE < RMSE_{ADE}$ should be used for the interpretation of model results (Bonanno et al., 2022). The successive analysis of the transient storage process and transport metrics were conducted only on the behavioral parameter sets ($RMSE < RMSE_{ADE}$).

After every model iteration, we evaluated the mean and standard deviation of the top 10% *RMSE* for all the modeling results and behavioral parameter sets only. This is because the top 10% of the results are often used as a behavioral threshold in several studies addressing the identifiability of TSM parameters (Kelleher et al., 2019; Wagener et al., 2002; Ward, Kelleher, et al., 2017). Following Pianosi et al. (2015) and Bonanno et al. (2022), we interpreted a decrease in the mean and standard deviation of *RMSE* with an increasing number of TSM iterations as an increase in model identifiability. On the contrary, the constant mean and standard deviation of *RMSE* with an increasing number of iterations have been interpreted as the model is unable to increase TSM performances with increasing TSM iterations.

Die approbierte gedruckte Originalversion dieser Dissertation ist an der TU Wien Bibliothek verfügbar.
The approved original version of this doctoral thesis is available in print at TU Wien Bibliothek.
TU Bibliothek Your knowledge hub WIEN

Die approbierte gedruckte Originalversion dieser Dissertation ist an der TU Wien Bibliothek verfügbar.
The approved original version of this doctoral thesis is available in print at TU Wien Bibliothek.
TU Bibliothek WIEN Your knowledge hub

We here compared our results to the more traditional inverse modeling approach, OTIS-P. OTIS-P uses a non-linear regression scheme to minimize the residual sum of squares between the modeled BTC and the observed BTC and returns the 95% confidence interval for the estimated TSM parameters. Following Runkel (1998), we carried out multiple OTIS-P iterations starting from different initial parameter values ($A = A_{ADE}$, $D = D_{ADE}$ and $\alpha = A_{TS} = 0.1$; $\alpha = A_{TS} = 0.01$; $\alpha = A_{TS} = 0.001$, where *ADE* subscript indicates the best-fitting model parameter obtained after the BTC fitting using the advection-dispersion equation; see Bonanno et al., 2022). This was done to avoid false model convergence to a local minimum. We applied OTIS-P in consecutive steps, setting the results obtained from the previous modeling output as starting parameter values of the successive software application. We finalized the use of OTIS-P when parameter values changed less than 0.1% between subsequent runs (Ward, Kelleher, et al., 2017). When OTIS-P was not able to converge to a unique set of parameter values or indicated convergence errors, we discarded its results.

Table 3.3. List of calibration parameters and used initial ranges for the first iteration of the random sampling of TSM parameters. The subscript ADE indicates the best-fitting model parameter obtained after the BTC fitting using the advection-dispersion equation

Abbrev.	Parameter	Lower bound	Upper bound
v [m/s]	Flow velocity	$0.5v_{ADE}$	$2v_{ADE}$
A [m^2]	Advective channel cross-sectional area	$0.5A_{ADE}$	$2A_{ADE}$
D [m^2/s]	Longitudinal dispersion coefficient	10^{-4}	$2D_{ADE}$
α [1/s]	Transient storage exchange rate	10^{-5}	0.1
A_{TS} [m^2]	Transient storage cross-sectional area	10^{-5}	1

3.4.7 Metrics characterizing solute transport in stream

We computed several metrics from the best-performing parameter sets ($RMSE < RMSE_{ADE}$) related to solute transport and storage in the study reach. The average distance a molecule needs to travel in the stream channel before entering the transient storage zone L_s [L] (Mulholland et al., 1997) is:

$$L_S = \frac{v}{\alpha} \qquad \text{Eq.3}$$

The average residence time of a tracer molecule in the transient storage zone (RT_s [T]) and the average time a tracer molecule remains in the stream channel before passing into the storage zone (RT_Q [T]) were evaluated (Thackston and Schnelle, 1970, Runkel, 2002):

$$RT_Q = \frac{L_S}{v} \qquad \text{Eq.4}$$

$$RT_S = \frac{A_{TS}}{\alpha \cdot A} \qquad \text{Eq.5}$$

We obtained the total water flux exchanged between the stream channel and the storage zone by multiplying the average water flux through the storage zone per unit length of the stream channel by the reach length L (q_s [L^3/T], modified from Harvey et al., 1996):

$$q_S = \alpha \cdot A \cdot L \qquad \text{Eq.6}$$

Die approbierte gedruckte Originalversion dieser Dissertation ist an der TU Wien Bibliothek verfügbar.
The approved original version of this doctoral thesis is available in print at TU Wien Bibliothek.
TU Bibliothek WIEN Your knowledge hub

We evaluated the hydrological retention factor (R_H [T/L]), which is a useful metric to compare transient storage among reaches and under different discharges, since it quantifies the storage zone residence time of water per unit of stream reach traveled (Morrice et al., 1997):

$$R_H = \frac{A_{TS}}{A \cdot v} \qquad \text{Eq.7}$$

We evaluated F_{MED} [-] which incorporates the role of advective transport and transient storage processes (Runkel, 2002):

$$F_{MED} \cong \left(1 - e^{\left(-L\frac{\alpha}{v}\right)}\right)\frac{A_{TS}}{A_{TS}+A} \qquad \text{Eq.8}$$

F_{MED} indicates the relative influence of transient storage on the median transport time of solute along a reach, thus increasing values of F_{MED} have to be interpreted as relatively larger importance of the transient storage processes on the solute transport.

From the measured water depth in the stream channel and other streambed characteristics we evaluated the Darcy-Weisbach friction factor (f [-]), which has been related to streambed complexity and in-stream transient storage zones (Thackston and Schnelle, 1970; Bencala and Walters, 1983; Hart et al., 1999):

$$f = \frac{8g \cdot d \cdot S}{v^2} \qquad \text{Eq.9}$$

Where g [L/T^2] is the gravitational constant, S [L/L] is the slope of the energy grade line estimated from the stream channel slope (Zarnetske et al., 2007), d [L] is the average water depth measured in the stream channel.

We evaluated Manning's roughness coefficient n [-] to evaluate if an increase in transient storage area could be linked to an increase of friction with in-stream sediments due to a larger contact area with the streambed fractured slate:

$$n = \frac{R^{\frac{2}{3}} \cdot S^{\frac{1}{2}}}{v} \qquad \text{Eq.10}$$

3.5 Results

3.5.1 Transient storage model parameters and their identifiability

The iterative modeling approach was effective in identifying the model parameter for the 31 tracer experiments regardless of the hydrologic conditions (Figure 3.2). The best-fitting parameter sets obtained at the end of the TSM iterations outperformed results from OTIS-P for 20 of the 31 experiments (Appendix F). OTIS-P also proved ineffective in calibrating the TSM parameters for four tracer experiments, due to convergence errors in the inverse modeling scheme.

Die approbierte gedruckte Originalversion dieser Dissertation ist an der TU Wien Bibliothek verfügbar.
The approved original version of this doctoral thesis is available in print at TU Wien Bibliothek.
TU Bibliothek WIEN Your knowledge hub

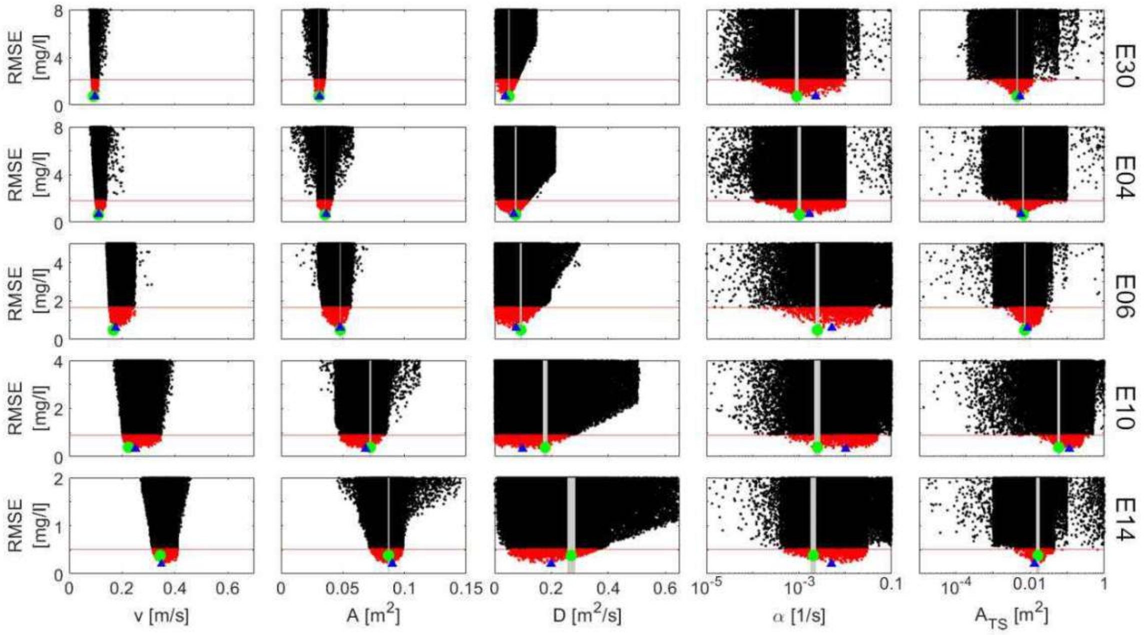

Figure 3.2. Results of the iterative modeling approach are reported as parameter values plotted against the corresponding *RMSE* values. Black and red dots indicate parameter sets and corresponding model performances with lower (black) and higher (red) performance than the ADE. Green dots indicate calibration results via OTIS-P and the grey areas indicate the corresponding 95% parameter confidence limits. The blue triangles indicate the best-performing parameter set obtained via the iterative modeling approach. The horizontal red line indicates the adopted behavioral threshold ($RMSE_{ADE}$). Results are reported for five different experiments with higher values of discharge: E30 = 2.8 l/s; E04 = 3.8 l/s; E06 = 7.9 l/s; E10 = 15.9 l/s; E14 = 28.6 l/s.

The distribution of the model errors for the top 10% of model results with $RMSE < RMSE_{ADE}$ indicates that higher discharge during an experiment is linked to a better performance of the TSM compared to experiments with lower discharge (boxplots, Figure 3.3). This is observable in the results from the iterative modeling approach and OTIS-P (blue triangles and green dots in Figure 3.3). The difference in performance between the TSM results and the $RMSE_{ADE}$ is smaller for experiments with higher discharge compared to experiments with low discharge (red squares, Figure 3.3). Our results also show that after four or five TSM iterations the mean and standard deviation of the model errors for the top 10% of model results and for the top 10% of model results with $RMSE < RMSE_{ADE}$ are constant with the increasing number of iterations (Figure 3.4). This outcome shows that the high number of iterations only matters for obtaining the best-fitting parameter sets (red dots in Figure 3.2; blue triangles in Figures 3.2 and 3.3) but does not control the distribution of the behavioral parameter sets. This is because model performances for the top 10% of model outcomes converge toward unique values after a few TSM iterations and do not decrease considerably with the number of iterations (Figure 3.4).

Our iterative modeling approach also shows that under low discharge there is a sharp decrease in model errors with the number of TSM iterations, and that the behavioral threshold of obtaining at least 1000 parameter sets with $RMSE < RMSE_{ADE}$ is satisfied after a few iterations (< 10 iterations, blue lines Figure 3.4). On the contrary, under higher discharge, the iterative modeling approach shows a smoother decrease of model performances with the increasing number of model iterations,

Die approbierte gedruckte Originalversion dieser Dissertation ist an der TU Wien Bibliothek verfügbar.
The approved original version of this doctoral thesis is available in print at TU Wien Bibliothek.
TU WIEN Bibliothek Your knowledge hub

and the behavioral threshold of obtaining at least 1000 parameter sets with $RMSE < RMSE_{ADE}$ is satisfied only after a large number of iterations (> 10 iterations, red lines Figure 3.4).

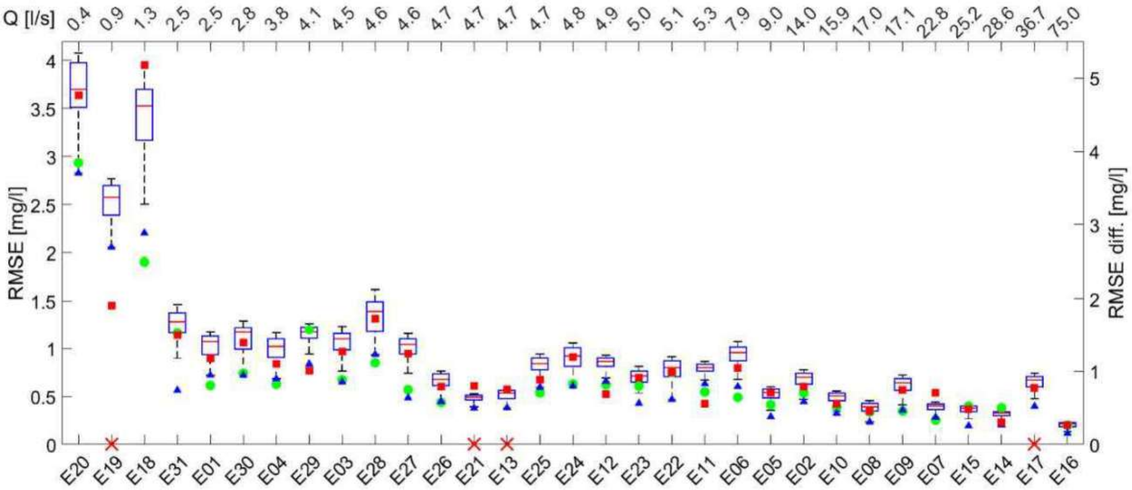

Figure 3.3. Left y-axis: Boxplot of the distributions of model error for the 10% best-performing parameter sets ($RMSE < RMSE_{ADE}$). Blue triangles and green dots indicate model performances obtained via the iterative modeling approach and OTIS-P respectively. The bottom x-axis reports the ID code of the tracer experiments, while the upper x-axis indicates the corresponding discharge conditions [l/s]. Right y-axis: the red squares indicate the difference between $RMSE_{ADE}$ and the $RMSE$ of the best-performing parameter sets via the iterative modeling approach. Red crosses on the bottom x-axis indicated ineffective application of OTIS-P (false convergence).

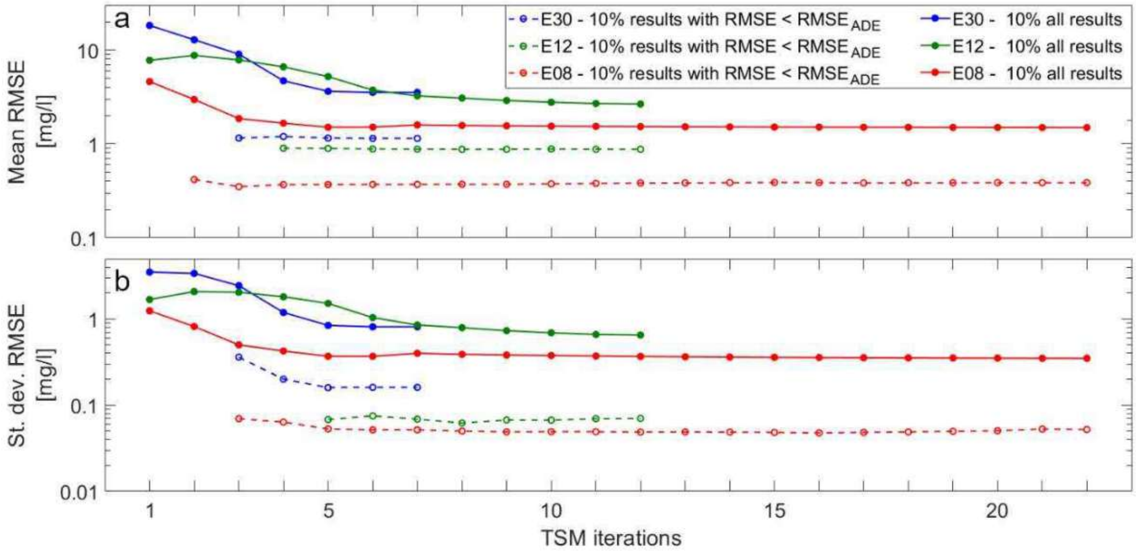

Figure 3.4. Dependency of (a) mean and (b) standard deviation of model error for the top 10% of the modeling results on the number of TSM iterations. Results have been shown for three experiments (E30 = 2.78 l/s; E12 = 4.88 l/s; E08 = 16.97 l/s). Each TSM iteration includes model performances for 35,000 parameter sets. An increase in TSM iterations has to be interpreted as an increase in the total number of parameter sets considered for the evaluation of mean and standard deviation of $RMSE$ values (e.g. 10 TSM iterations include model results for 350,000 parameter sets).

Die approbierte gedruckte Originalversion dieser Dissertation ist an der TU Wien Bibliothek verfügbar.
The approved original version of this doctoral thesis is available in print at TU Wien Bibliothek.
TU WIEN Bibliothek Your knowledge hub

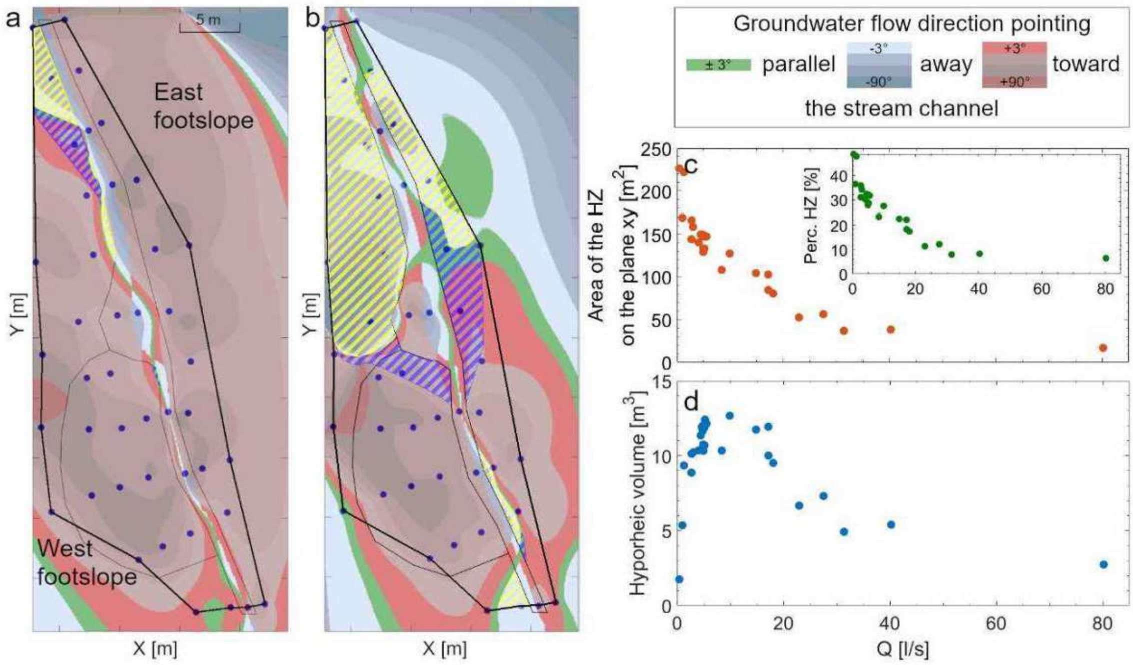

Figure 3.5. Contraction and extension of the size of the hyporheic zone exemplified for two experiments with (a) 75.0 l/s (E16) and (b) 0.4 l/s (E20). Colors of (a) and (b) indicate the groundwater flow direction normalized with the respect to the direction of the stream channel on the xy plane (flow direction of 0o equal to -72o on the xy plane). Green areas indicate groundwater flow direction flowing parallel to the stream channel; blue areas indicate groundwater pointing away from the stream channel; red areas indicate groundwater pointing toward the stream channel; dashed yellow areas indicate area of the hyporheic zone receiving stream water, while dashed blue areas indicate the area od the hyporheic zone returning water to the stream channel. The black line indicates the perimeter of the maximum size of the hyporheic zone conditional to the well network. (c) Orange dots, dependency of the evaluated size of the hyporheic zone with discharge. The subplot (green dots) reports the dependency of the percentage of the near-stream groundwater area pointing away and returning to the stream channel with discharge. (d) Dependency of the evaluated volume of the hyporheic zone with discharge.

Die approbierte gedruckte Originalversion dieser Dissertation ist an der TU Wien Bibliothek verfügbar.
The approved original version of this doctoral thesis is available in print at TU Wien Bibliothek.
TU Bibliothek Your knowledge hub WIEN

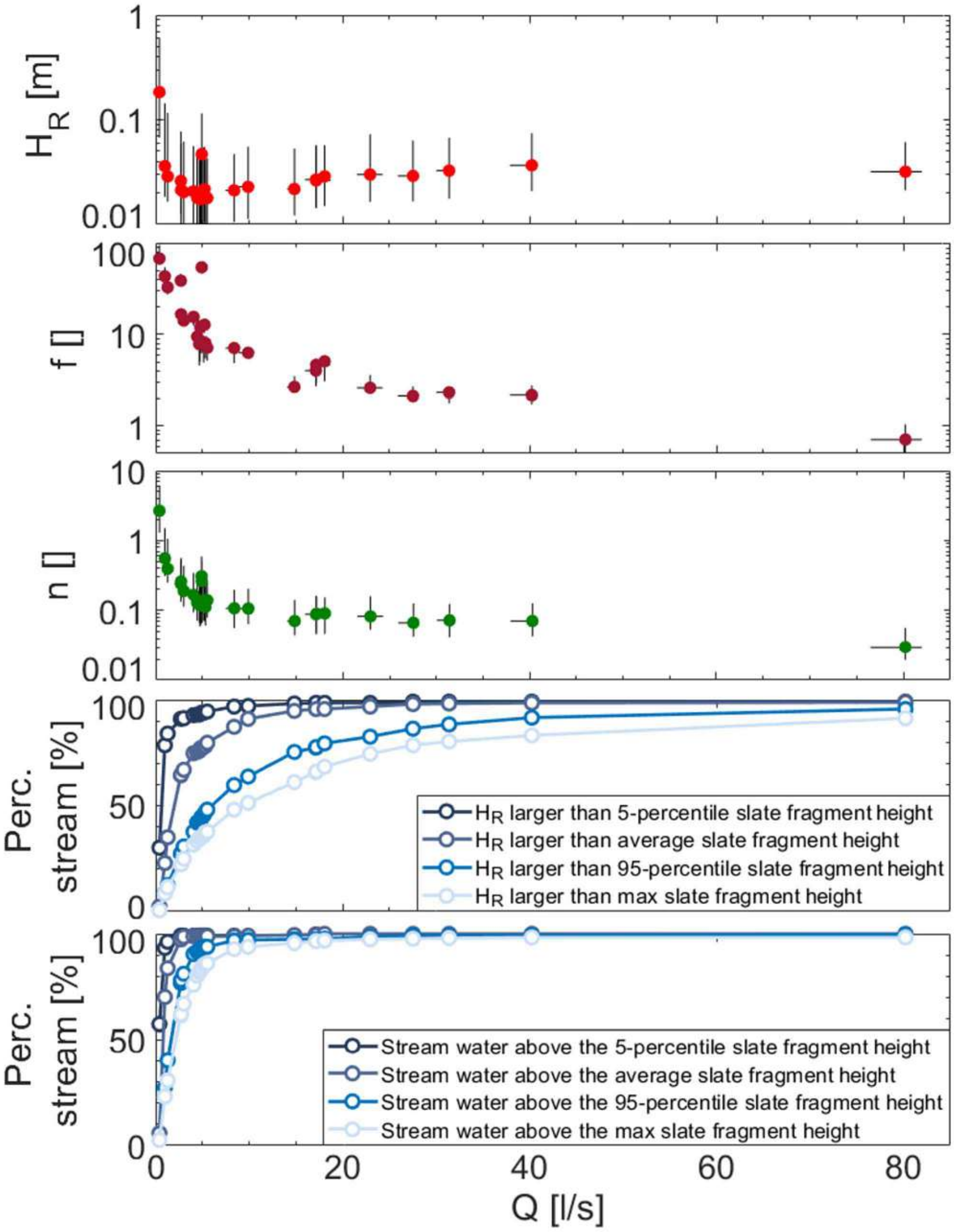

Figure 3.6. Evaluation of (a) hydraulic radius H_R, (b) Darcy-Weisbach friction factor *f*, (c) Manning's roughness coefficient *n*, and percentage of the stream reach where the (d) hydraulic radius or the (e) stream water level was higher than the 5-percentile, average, 95-percentile and maximum height of the slate fragment that makes up the streambed against discharge for the 31 tracer experiments. Horizontal black lines indicate the 5- and 95-percentile limits of discharge for the top 10% TSM results with $RMSE < RMSE_{ADE}$. Vertical black lines indicate the 5 and 95 percentile limits of H_R, *f*, and *n* evaluated for the total LIDAR transects.

3.5.3 How does transient storage change between experiments?

Results from the iterative modeling approach show that advection-dispersion parameters increase with discharge (Figure 3.7a, c, e). The increase of *v* with discharge follows a linear and quadratic function ($R^2 = 0.967$, $R^2 = 0.968$, respectively; p-value < 0.01), the increase of *A* and *D* with discharge follows a quadratic function ($R^2 = 0.807$ and $R^2 = 0.862$, for *A* and *D* respectively; p-value < 0.01). The TSM parameters also increase with discharge. α (Figure 3.7b) follows a linear

(R^2 of 0.872, p-value < 0.01) and a quadratic fitting function ($R^2 = 0.94$, p-value < 0.01) and A_{TS} (Figure 3.7d) show high variability ($R^2 < 0.377$ for a quadratic and linear fit despite the statistical relevance (p-value < 0.01). For discharge stages lower than 4.9 l/s the A_{TS} parameter is poorly correlated to discharge ($R^2 = 0.005$, p-value > 0.9 on 16 experiments), while for values above 4.9 l/s A_{TS} parameter linearly and significantly increases with discharge ($R^2 = 0.88$, p-value < 0.01 on 15 experiments). The correlation of A_{TS} with discharge results in a similar behavior of A_{TS}/A (Figure 3.7f). The ratio A_{TS}/A shows a sharp decrease with discharge for values lower than ~ 4 l/s (linear $R^2 = 0.796$, p-value < 0.01), no clear pattern for values between ~ 4 and ~ 5 l/s (scattering around the median value of 0.161, $R^2 = 0.007$, p-value $= 0.82$), and significantly increases with discharge for values above ~ 5 l/s ($R^2 = 0.552$, p-value < 0.01).

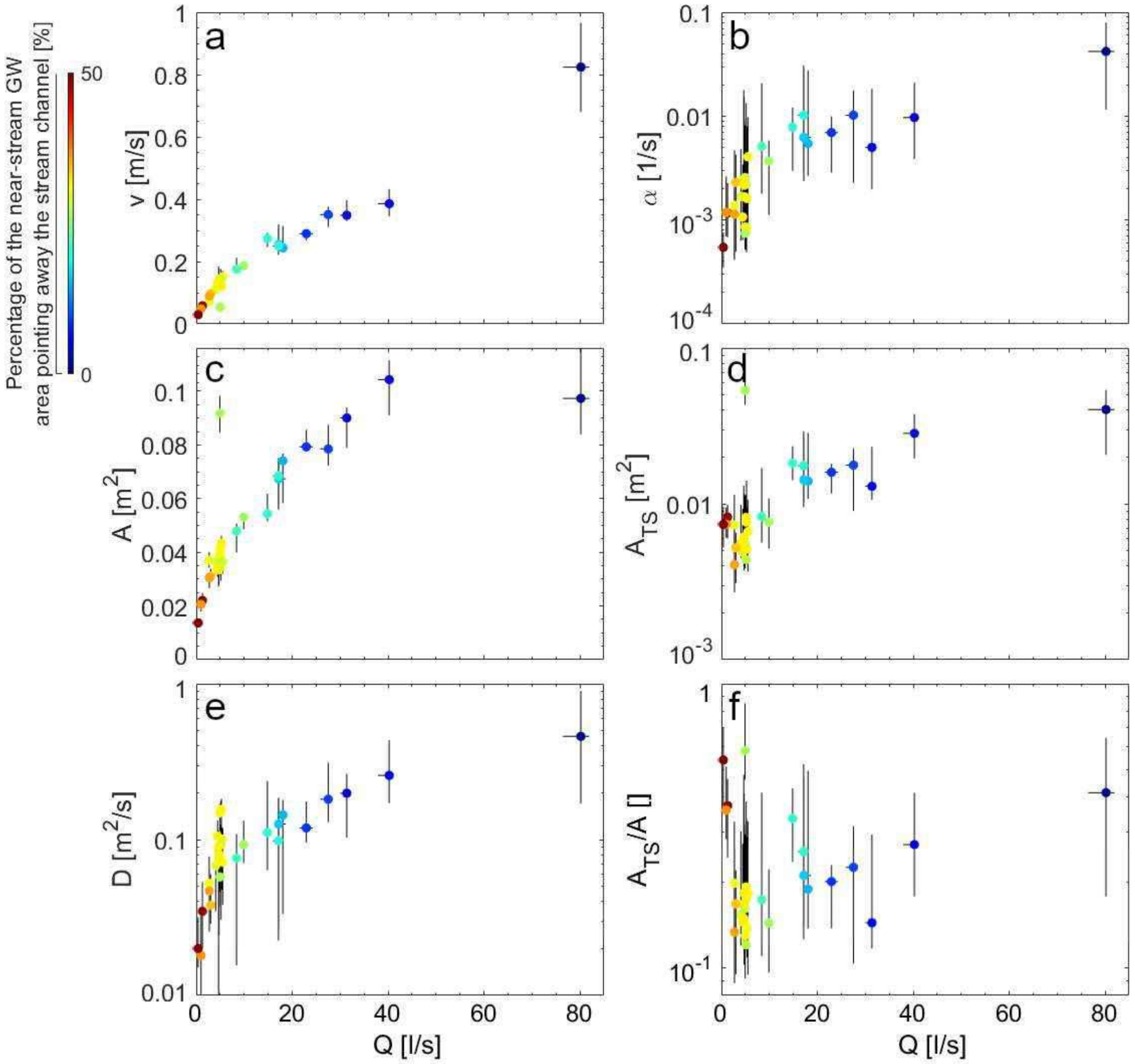

Figure 3.7. TSM parameters in relation to discharge during the experiments. Plots are reported for (a) flow velocity, (c) advective channel cross-sectional area, (e) longitudinal dispersion coefficient, (b) transient storage exchange rate, (d) transient storage cross-sectional area, and (f) ratio between transient storage cross-sectional area and advective channel cross-sectional area. Dots show the best parameter set obtained from the iterative modeling approach. Vertical and horizontal black lines indicate 5 and 95 percentile limits of the top 10% results with $RMSE < RMSE_{ADE}$. Gradient colors indicate the percentage of the near-stream groundwater area pointing away from the stream channel (cfr. Figure 3.5).

Die approbierte gedruckte Originalversion dieser Dissertation ist an der TU Wien Bibliothek verfügbar.
The approved original version of this doctoral thesis is available in print at TU Wien Bibliothek.
TU Bibliothek WIEN Your knowledge hub

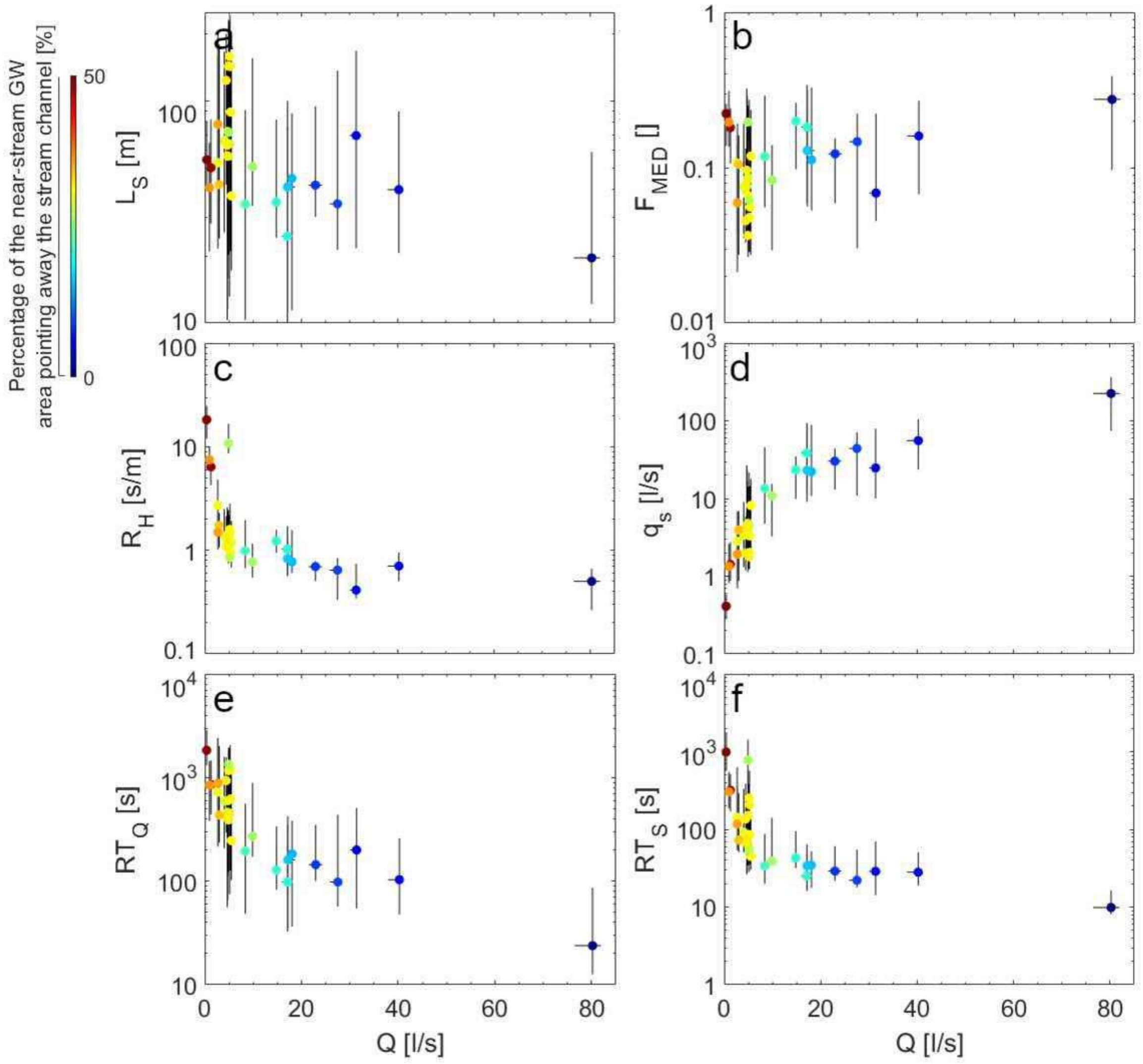

Figure 3.8. Same as Figure 3.7, but reporting (a) the average distance a water molecule needs to travel in the stream channel before entering the transient storage zone, (b) the fraction of median travel time due to transient storage, (c) the hydrological retention factor, (d) the total water flux exchanged between the stream channel and the storage zone, (e) the average residence time of a tracer molecule in the stream channel, and (f) in the transient storage zone transport metrics as a function of discharge.

The transport metrics show different patterns against discharge (Figure 3.8). The average distance a molecule traveled downstream the main channel before entering the storage zone (L_S) shows a linear decrease with discharge (R^2 = 0.139, p-value = 0.04, Figure 3.8a). The F_{MED} metric shows high variability (R^2 = 0.236 for a linear fit) despite the statistical significance (p-value < 0.01, Figure 3.8b). The hydrologic retention factor (R_H) decreases with increasing discharge (Figure 3.8c) following an exponential decrease function (R^2 = 0.71, p-value < 0.001). The total water flux exchanged between the stream channel and the storage zone (q_s) increases with discharge and was well approximated by both a linear and a cubic function (R > 0.894 and p-value < 0.01, Figure 3.8d). The average residence time in the stream channel (RT_Q) and the transient storage zone (RT_S) are negatively correlated with discharge (Figure 3.8e, f). The decrease of RT_Q with Q can be approximated by both linear (R^2 = 0.284), quadratic (R^2 = 0.451), and exponential (R^2 = 0.541) decrease (p-value < 0.001). However, the decrease of RT_S with discharge is satisfactorily simulated (p-value < 0.01) by exponential decrease only ($R^2 = 0.471$).

3.6 Discussion

3.6.1 Parameter identifiability in the Transient Storage Model depends on discharge during the tracer experiments

When TSM parameters are non-identifiable they are interdependent and a change of a certain parameter would be balanced by a proportional change of other parameters, eventually leading to the same model performances (Camacho & González, 2008; Kelleher et al., 2019; Wagener et al., 2002; Wlostowski et al., 2013). Our results indicate that the interdependency of TSM parameters increases with higher discharge during the experiment. This is visible from the less pronounced peak of performances of v, A, and D (red dots, Figure 3.2) and the limited increase of TSM performance compared to ADE performance with higher discharge (red squares, Figure 3.3). Also, the space of the advection-dispersion parameters showing satisfactory model performances ($RMSE < RMSE_{ADE}$) increased with the discharge (Figure 3.2) resulting in a larger 5- and 95-percentile limits of the top 10% TSM results compared to experiments with low discharge, where advection-dispersion parameters showed a rather narrow peak of performances (Figure 3.2; black lines, Figure 3.7). These results corroborate the interpretation that greater parameter interactions cause poorer parameter identifiability and model performances (Kelleher et al., 2013; Ward, Payn, et al., 2013). As addition to the existent body of literature, our outcomes also show the predominant role of the advection-dispersion process on the BTC under high discharge stages that hampers the identification of a clear peak in model performance, due to the proportionally greater importance of v, A, and D in controlling the BTC compared to lower discharge.

Compared to previous studies, our study shows that the difference between $RMSE_{ADE}$ and $RMSE$ obtained via the iterative modeling approach decreases with discharge (red dots, Figure 3.3). This result means that the advection-dispersion parameters explain largely the shape of BTC during high discharge and that the transient storage process added to the advection-dispersion equation contributes to a modest improvement of model performances compared to the ADE. No previous study directly addressed the identifiability of TSM parameters for a set of tracer experiments across a wide range of discharges. Our results are consistent with studies that reported that the advection-dispersion process becomes predominant over the transient storage processes during higher discharge. For example, Wagner and Harvey (1997) were the first to point toward the role of the advection-dispersion process for the identifiability of the transient storage parameters while Kelleher et al., (2013) and Bonanno et al., (2022) demonstrated advection-dispersion parameters control progressively larger portions of the BTC under higher discharge, while transient-storage parameters control progressively larger portions of the BTC under lower discharge.

Our results offer an explanation on why the identifiability analysis in previous studies was sometimes effective and sometimes ineffective for achieving parameter identifiability for TSMs. We believe that the advection-dispersion process was not predominant at study sites with relatively low discharge meaning that α and A_{TS} were explanatory of large portions of the BTC. As a result,

Die approbierte gedruckte Originalversion dieser Dissertation ist an der TU Wien Bibliothek verfügbar.
The approved original version of this doctoral thesis is available in print at TU Wien Bibliothek.
TU WIEN Bibliothek Your knowledge hub

the TSM improved substantially performances compared to ADE due to the pronounced tail of the BTC, and the identifiability of TSM parameters was achieved via two iterative random sampling for a total of 100,000 parameter sets (Ward et al., 2018; first BTC in Ward, Kelleher, et al., 2017). On the other hand, headwater reaches characterized by steep channel gradients and relatively short investigated reaches indicated non-identifiability of TSM parameters (Kelleher et al., 2013; Ward, Payn, et al., 2013; second and third BTCs in Ward, Kelleher, et al., 2017). This is probably because the advection-dispersion process at these study sites dominated the tracer transport and the investigated parameter space and/or the used number of parameter sets (often ≤ 100,000) did not allow to target $RMSE < RMSE_{ADE}$ for a sufficient number of parameter sets to show identifiability.

The iterative modeling approach used in this work can also demonstrate that selecting a narrow (< two orders of magnitude) parameter interval in a random-sampling approach can cause an "apparent" non-identifiability in TSM. If we had sampled a parameter from a narrow space around the peak of performance (e.g. α between 0.001 and 0.003 1/s, E06, results not shown), the identifiability analysis results would lead us to the conclusion that the parameter was non-identifiable. However, this same interval shows optimal performances when a wider parameter space is sampled (Figure 3.2). This can explain why previous studies investigating a narrow range of TSM parameters have never achieved parameters identifiability (Wagener et al., 2002; Camacho & González, 2008; Wlostowski et al., 2013) precisely because a narrow parameter space does not allow for a clear increase of model performances. This, in turn, would "hide" the identifiability of a parameter, especially when not enough parameter sets are sampled (< 100,000, Ward et al., 2017; Bonanno et al., 2022). We here proved that the iterative modeling approach introduced by Bonanno et al (2022) can address model performances and parameter identifiability regardless of the discharge during the tracer experiment and over a parameter space spanning several orders of magnitudes, which is in agreement with recent recommendations for identifiability analysis (Pianosi et al., 2016) and previous work (Kelleher et al., 2019; Ward, Payn, et al., 2013; Kelleher et al., 2013; Ward, Kelleher, et al., 2017).

Our OTIS-P simulations showed good model performance, as the calibrated TSM parameters were in the same parameter space as the results of the iterative modeling approach (Appendix F, Figure 3.2). However, the best-fitting parameter sets obtained from our iterative modeling approach outperformed the OTIS-P results for most tracer experiments and allowed us to obtain identifiability of TSM parameters even for those BTCs where the OTIS-P failed to converge. The performances of OTIS-P and the iterative modeling approach used in this study are certainly typical of the study site. Future research is needed to apply the used iterative modeling approach in other stream reaches as well, since tracer experiments conducted in different geomorphological settings proved to have a strong influence on the shape of the BTC and TSM performances (D'Angelo et al., 1993; Edwardson et al., 2003; Hall et al., 2002; Zarnetske et al., 2007). Furthermore, the obtained identifiability of model parameters could be controlled by the simplistic formulation of the model, which characterizes transient storage as a single storage area with a solute residence time that follows an exponential decay. Future work is needed to test this iterative modeling approach using numerical modifications of TSM that would increase the number of TSM

Die approbierte gedruckte Originalversion dieser Dissertation ist an der TU Wien Bibliothek verfügbar.
The approved original version of this doctoral thesis is available in print at TU Wien Bibliothek.
TU WIEN Bibliothek Your knowledge hub

parameters, thus their interaction and non-identifiability (Knapp & Kelleher, 2020). Among the diverse TSM formulations aiming for a more realistic description of solute transport in streams, the used iterative modeling approach should be used in TSMs with multiple transient storage areas (Choi et al., 2000; Fabian et al., 2011), in TSMs with different residence time distribution laws (Bottacin-Busolin & Marion, 2010; Gooseff et al., 2005; Haggerty et al., 2002), or for BTCs of non-conservative solutes (Kelleher et al., 2019).

3.6.2 Dynamics of transient storage processes under different hydrologic conditions

The significant correlations between v and A and discharge are not surprising in TSM and it has been observed in previous work (Hall et al., 2002; Hart et al., 1999; Schmid et al., 2010). The higher longitudinal dispersion coefficients D in experiments with higher discharge are also in line with the TSM formulation and with the observed increase of the Reynolds number with discharge (between $2.99 \cdot 10^3$ and $2.22 \cdot 10^5$, linear and quadratic function fit with $R > 0.99$, p-value < 0.01, plots not shown). D is responsible for the longitudinal spreading of the tracer above and behind the center of the solute pulse, thus it is expected to increase with increasing streambed roughness and channel complexity (Gooseff, Bencala, et al., 2008).

The trend of the A_{TS}/A ratio for discharge below ~ 5 l/s (Figure 3.7f), together with the high values of the hydrologic retention factor R_H (> 1 s/m Figure 3.8c), *FMED* (> 0.1, Figure 3.8b), and the negative correlation of RT_S and RT_Q with discharge (Figure 3.8e, f) suggest a non-negligible contribution of hyporheic exchange to transient storage for experiments with low discharge (< 5 l/s) compared to experiments with higher discharge. This interpretation is supported by the large potential size of the hyporheic zone assessed through groundwater measurements (Figure 3.5c) and by the increasing volume of the hyporheic zone volume for discharge lower than 5 l/s (Figure 3.5d). This is consistent with previous studies where gradients from the stream channel toward the adjacent groundwater have been linked to hyporheic transport (González-Pinzón et al., 2015; Harvey & Bencala, 1993; Kasahara & Wondzell, 2003). However, our findings also indicate a significant role of in-stream transient storage during low discharge (< 5 l/s). This can be deduced from the high values of the friction factor f and the roughness coefficient n obtained for experiments with low discharge and the fact that the hydraulic radius H_R was at its minimum at $Q = 5.1$ l/s. These results indicate that the wetted perimeter increases more than the wet stream area for higher discharge between 0.41 and 5.1 l/s. This in turn causes a greater proportion of the streambed material to be submerged, but not completely (Figure 3.6d, e). This partial submergence of larger areas of the streambed material causes the development of secondary flowpaths among the slate fragments and turbulences in the shaded area immediately downstream causing an increase in the in-stream transient storage. Our results show that transient storage during experiments under low discharge at the study site ($Q < 5$ l/s) cannot be explained by hyporheic exchange or in-stream transient storage alone, but as a combination of both.

Higher discharge at the study site is characterized by an increase in gradients from the adjacent groundwater toward the stream channel, indicating hillslope-stream connectivity on the west and the east hillslopes (Bonanno et al., 2021). This is consistent with our results indicating a decrease of the size of the groundwater area and volume receiving water from the stream channel (Figure

3.4c, d) for experiments with discharge higher than 5 l/s. These results show that the hyporheic exchange decreases with higher discharge suggesting that transient storage is mainly controlled by in-stream transient storage. However, the observed high percentage of slate fragments in the stream channel that are entirely submerged below the water table with higher discharge (Figure 3.6d, e) indicates that the secondary flowpaths and shadow zones controlling in-stream transient storage at lower discharge are now part of the advective stream channel. Also, the observed trend of the hydraulic radius with discharge shows that the wet area increases more than the wet perimeter for discharge higher than 5 l/s (Figure 3.6a-c). These results provide additional evidence that also in-stream transient storage becomes less important for solute transport with higher discharge at the study site.

The reduction of the groundwater area receiving water from the stream channel and the inclusion of the streambed slate fragments into the advective stream channel show that higher discharge has a lower potential for both hyporheic and dead-zones transient storage compared to lower discharge. However, the decrease of the roughness n and friction factor f (Figure 3.6b, c) indicate that the transient storage at the study site for higher discharge is controlled by increasing spatial heterogeneities of the velocity gradients in the water column mostly due to the increasing wetted area (Figure 3.7c) and the increasing shear velocity u^* on the streambed ($u^* \propto gdS$, as in Eq. 9, see Fisher et al., 1979). This interpretation is also in line with the simulated rapid hydrologic exchange α (Figure 3.7b) causing a solute retention time in the transient storage zone no longer than a few seconds (Figure 3.8f). This outcome is consistent with research at other sites characterized by low hyporheic exchange, where higher discharge during tracer experiments resulted in relatively lower in-stream transient storage compared to lower discharge (Martí et al., 1997; Zarnetske et al., 2011), due to a proportionally larger impact of advection-dispersion and due to a lower contact area with the streambed (Gooseff, Payn, et al., 2008; Jackson et al., 2013).

Compared to the extension of the hyporheic zone area and volume (Figure 3.4c, d), the deduced order of magnitude of A_{TS} and q_S (Figure 3.7d, 3.8d) indicates that we were likely unable to capture longer flowpaths and residence time of the stream water into large areas of the hyporheic zone as evaluated via the groundwater measurements. Instantaneous injections are capable of returning model information comparable to that of continuous injections for conservative tracers (Gooseff, Payn, et al., 2008; Payn et al., 2008). However, they are also limited by the available "window of detection", which is biased towards faster transient storage processes and shallow hyporheic exchange (Harvey & Wagner, 2000; Jin & Ward, 2005; Wondzell, 2006). As a result, we only calculated an A_{TS} below 0.1 m^2 and a tracer residence time in the transient storage zone below 10^3 s (Figure 3.8f), despite the large size of the inferred hyporheic zone when discharge was low (Figure 3.4). The obtained TSM metrics are biased toward shorter residence times and shallow hyporheic exchange and are thus unable to capture the full spectrum of available flowpaths at the investigated discharge. The direct observation of groundwater levels from the monitoring well network provided valuable support to bypass the "window of detection" issue typical of tracer experiments. If we would have based our model result on TSM parameters alone we would probably have ruled out

Die approbierte gedruckte Originalversion dieser Dissertation ist an der TU Wien Bibliothek verfügbar.
The approved original version of this doctoral thesis is available in print at TU Wien Bibliothek.
TU WIEN Bibliothek Your knowledge hub

Die approbierte gedruckte Originalversion dieser Dissertation ist an der TU Wien Bibliothek verfügbar.
The approved original version of this doctoral thesis is available in print at TU Wien Bibliothek.
TU WIEN Bibliothek Your knowledge hub

the presence of a hyporheic zone always lower than 0.1 m^2, whereas the groundwater measurement revealed a size of the groundwater area receiving water from the stream of several m^2.

The interpretation of modeling results in tracer studies lacks the combination of data on near-stream groundwater gradients and streambed micro-topography. In addition to the state of the art, our results provide novel insights into the role of the in-stream transient storage generated through streambed micro-topography and of the extension of the hyporheic zone generated through varying near-stream groundwater table. Basing process interpretation on TSM results alone, would have resulted in different conclusions. As an example, the observed increase of exchange rate α with discharge could have been interpreted as an increase of turbulence and eddies in the stream channel (D'Angelo et al., 1993; Elliott & Brooks, 1997; Zarnetske et al., 2007), but also as a higher contribution of the hyporheic flow (Schmid et al., 2010). Conversely, the observed increase of transient storage area A_{TS} with discharge could have been interpreted as both a larger size of the hyporheic zone (Dudley-Southern & Binley, 2015; Heeren et al., 2014), and an increase of in-stream transient storage due to an increase of in-stream dead-zones (Gooseff, Bencala, et al., 2008). Eventually, the trend of A_{TS}/A ratio with discharge could have been explained as the surface water interacts more with the streambed sediments (Martí et al., 1997), but also with the hyporheic zone (Butturini & Sabater, 1999) under lower discharge.

Our study is the first study to our knowledge that is addressing the concurrence of different processes controlling the transient storage via the use of TSM parameters, the near-stream groundwater levels, and the streambed micro-topography under several hydrologic conditions. We recognize that the adopted strategy is not without criticism. As an example, the groundwater monitoring well network is not designed to capture pressure gradients at the surface water–streambed interface that is recognized to be a non-negligible source of hyporheic flowpaths with increasing turbulence and discharge (Cardenas & Wilson, 2007; Packman & Bencala, 2000). In addition, the LIDAR scans might not be representative of the streambed micro-topography and slate distribution above the talweg across the relatively long investigated period (from December 2018 to June 2021) and more scans could have provided more robust results. Despite some limitations, our approach bypassed the "window of detection" problem typical of tracer injections and assessed the dynamic role of hyporheic exchange and in-stream transient storage on water transport across the hydrologic year.

3.7 Conclusion

Answering how and why transient storage processes change with different hydrologic conditions can bring a comprehensive assessment of their spatial and temporal role in regulating water quality in stream networks. In this study, we used an iterative modeling approach to obtain identifiability for the parameters of the transient storage model for 31 tracer breakthrough experiments at different discharges in a headwater stream reach. We combined the model results, groundwater table observations, and measurements of streambed micro-topography to support the interpretation of different processes concurring with the transient storage of streamwater through a wide range of hydrological conditions. Our work showed that the parameter space where advection-dispersion parameters were identifiable was wider under higher discharge, thus increasing the parameter interaction in the TSM. Our outcomes can thus explain the lack of parameter identifiability in several previous TSM studies and open up new challenges to address parameter identifiability in other model formulations implemented with many transient storage areas or with different residence time distributions. The introduction of the streambed micro-topography and groundwater table measurement provided valuable data for interpreting the TSM parameters and the transport metrics describing solute transport at the study site. Our model results showed that hyporheic exchange and in-stream transient storage control the transient storage of stream water during low discharge. Under higher discharge, the hyporheic zone and the in-stream dead zone become progressively less important in controlling transient storage, which is rather driven by eddies and turbulences in the stream water column. Because of the obtained clear trends between TSM parameters and discharge, our results also suggest that it could be possible to predict TSM parameters and the underlying processes at the study site prior to tracer experiments. Future work should combine tracer injections with streambed micro-topography and groundwater measurements in stream reaches characterized by different morphologies and hydrologic regimes. The combination of derived patterns between discharge, hyporheic area, stream water elevation, and streambed microtopography in several study sites would be key for understanding the spatial and temporal variation of transient storage processes in stream networks and across scales.

3.8 Acknowledgments

This work was supported by funding from the Luxembourg National Research Fund (FNR) for doctoral training (PRIDE15/10623093/HYDRO-CSI). We would like to acknowledge the financial support of the Austrian Science Fund (FWF) as part of the Vienna Doctoral Programme on Water Resource Systems (DK W1219-N28). We thank the University of Trier (Department IV - Erdbeobachtung und Klimaprozesse) for borrowing the laser scanner Faro Photon 120 and Christian Bossung for helping in conducting the scanners and for providing the .BIN files of the scans. We thank Jean-François Iffly, Jérôme Juilleret, and Laurent Gourdol for their help in the installation of the monitoring well network. We thank Ginevra Fabiani, and Laurent Pfister for their fruitful input and discussions.

Die approbierte gedruckte Originalversion dieser Dissertation ist an der TU Wien Bibliothek verfügbar.
The approved original version of this doctoral thesis is available in print at TU Wien Bibliothek.
TU WIEN Bibliothek Your knowledge hub

Rivers have always attracted me. The charm is perhaps in their continuous passing while remaining unchanged, in their leaving while remaining, in their being a sort of physical representation of history, which is, as it passes. Rivers are History.

– Tiziano Terzani, Buonanotte, signor Lenin

While the iterative modelling approach proved to be effective in obtaining identifiable model parameters in Chapters 2 and 3, its efficacy depends on the specific objective function used (root mean squared error, RMSE) and on the specific residence time distribution (RTD) used to simulate water retention in the stream corridor. Other objective functions such as normalized RMSE (Kelleher et al., 2019), Nash-Sutcliff efficiency (Fabian et al., 2011), or log-RMSE (Ward et al., 2017) could have returned different interpretations of the model outcomes and the identifiability of the parameters. Also, the choice of the exponential RTD might be inadequate to simulate long-term residence time in the stream corridor, which could be better simulated by a power-law (Haggerty et al., 2002) or a log-normal RTD (Wörman et al., 2002). The iterative modelling analysis introduced in Chapter 2 should be generalized and applied to other model formulations, where the increasing number of parameters can cause higher parameter interaction and non-identifiability, as well as enhance physical realism.

Hydrological models in stream hydrology are an essential tool for understanding the spread of solutes and pollutants in river networks. The iterative modelling approach presented in this thesis can be used to improve awareness of the transient storage of these substances in the stream channel and in the adjacent groundwater. This approach can also be applied in other hydrological models seeking a stronger physical realism, but influenced by the curse of dimensionality derived from an increase in the number of parameters. Also, this thesis improves the understanding of the drivers controlling streamwater-groundwater exchange via the use of spatial-dense and high-frequency measurements. The present work highlights the role of both morphologic and hydrologic drivers on the stream corridor, and their dynamic role in near-stream water flow direction across the hydrologic year. The results reported in this thesis are useful for interpreting the non-identifiability in past studies and for enhancing the understanding of the physical processes controlling water movement in the stream corridor.

TU WIEN Bibliothek Your knowledge hub
Die approbierte gedruckte Originalversion dieser Dissertation ist an der TU Wien Bibliothek verfügbar.
The approved original version of this doctoral thesis is available in print at TU Wien Bibliothek.

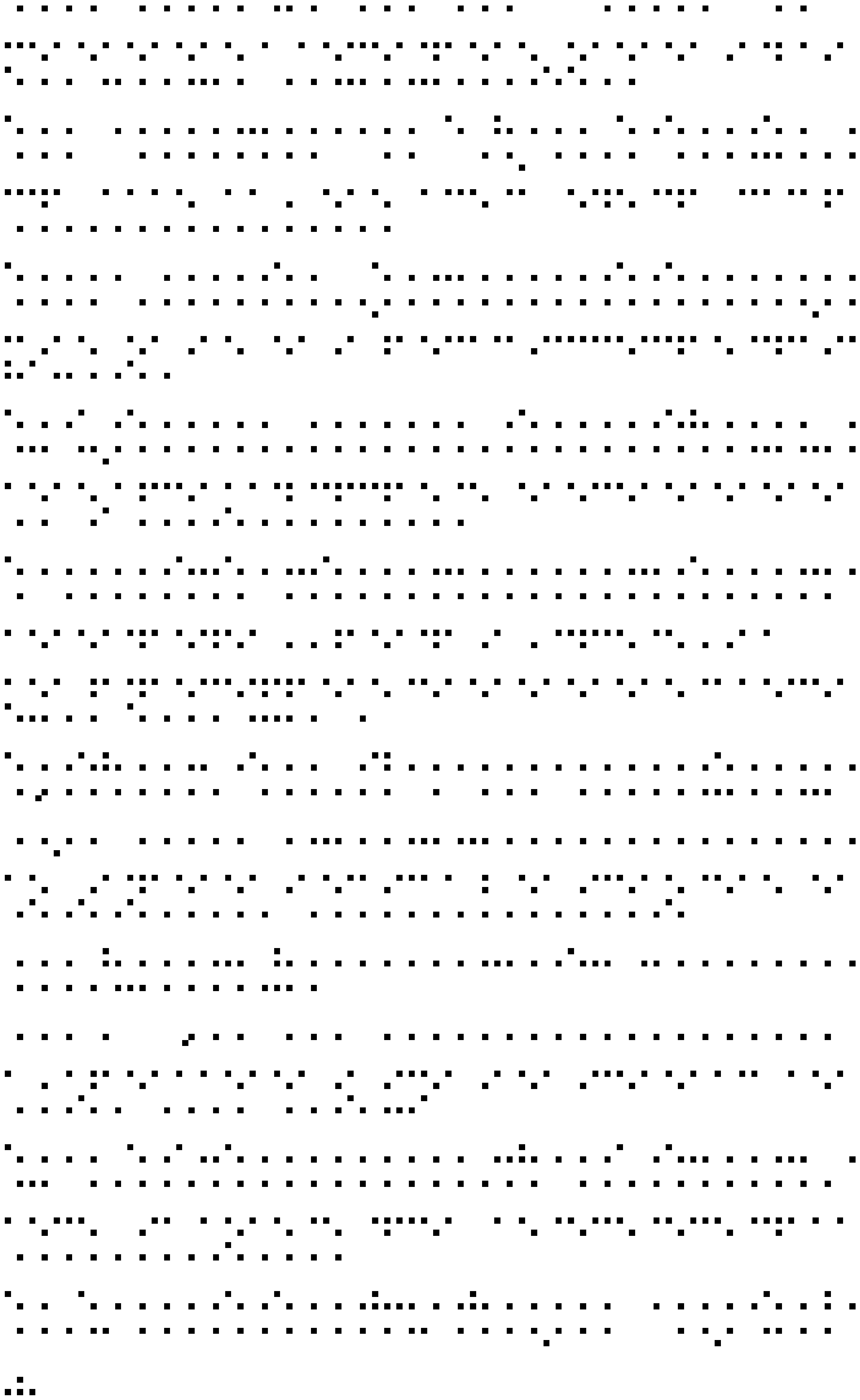

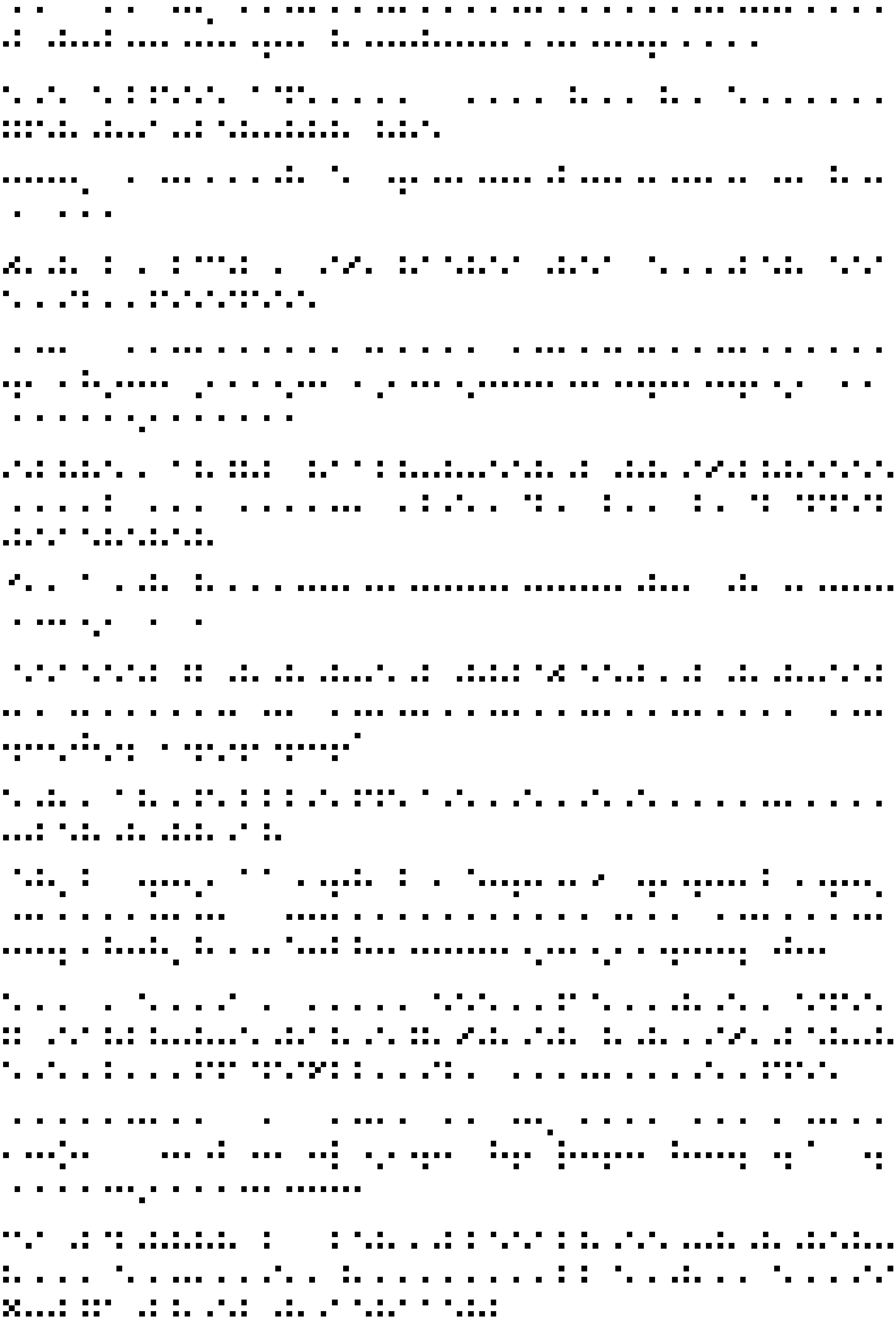

Zaramella, M., Marion, A., and Packman, A. I. (2006). Applicability of the Transient Storage Model to the hyporheic exchange of metals. Journal of Contaminant Hydrology, 84(1–2), 21–35. https://doi.org/10.1016/j.jconhyd.2005.12.002.

Zaramella, M., Marion, A., Lewandowski, J., and Nützmann, G. (2016). Assessment of transient storage exchange and advection-dispersion mechanisms from concentration signatures along breakthrough curves. Journal of Hydrology, 538(May), 794–801. https://doi.org/10.1016/j.jhydrol.2016.05.004.

Zarnetske, J. P., Gooseff, M. N., Brosten, T. R., Bradford, J. H., McNamara, J. P., & Bowden, W. B. (2007). Transient storage as a function of geomorphology, discharge, and permafrost active layer conditions in Arctic tundra streams. Water Resources Research, 43(7), 1–13. https://doi.org/10.1029/2005WR004816.

Zarnetske, J. P., Haggerty, R., Wondzell, S. M., & Baker, M. A. (2011). Dynamics of nitrate production and removal as a function of residence time in the hyporheic zone. Journal of Geophysical Research: Biogeosciences, 116(1), 1–12. https://doi.org/10.1029/2010JG001356.

Zarnetske, J. P., Haggerty, R., & Wondzell, S. M. (2015). Coupling multi- scale observations to evaluate hyporheic nitrate removal at the reach scale. Freshwater Science, 34(1), 172–186. https://doi.org/10.1086/ 680011.

Die approbierte gedruckte Originalversion dieser Dissertation ist an der TU Wien Bibliothek verfügbar.
The approved original version of this doctoral thesis is available in print at TU Wien Bibliothek.
TU WIEN Bibliothek Your knowledge hub

Appendix A

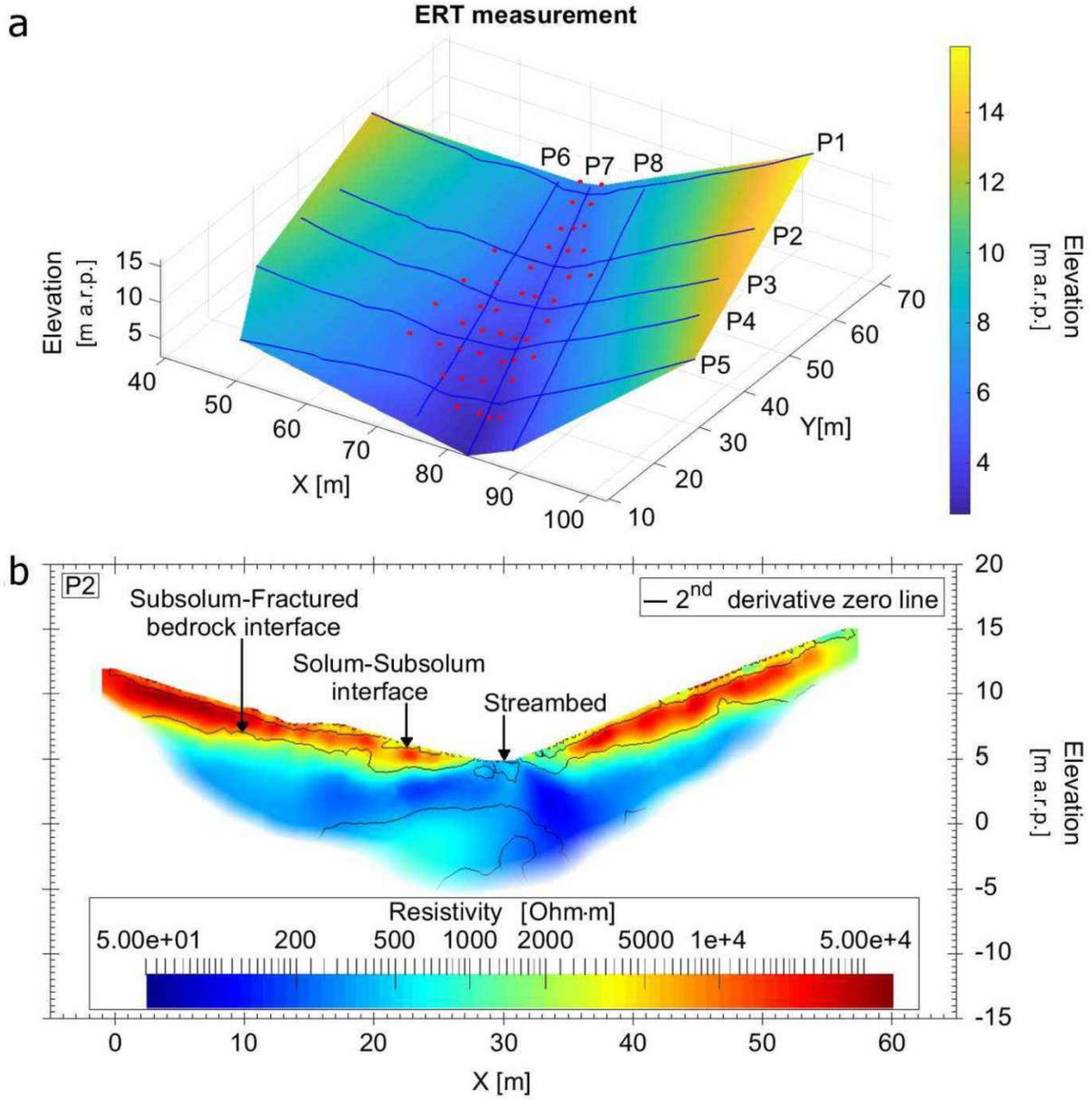

Figure A1. (a) Location of the electrical resistivity tomography (ERT) transects and position of the wells (red dots) and (b) resistivity of the ERT transect P2 with the indication of regolith interfaces by the use of the maximum resistivity change following Gourdol et al. (2021).

Die approbierte gedruckte Originalversion dieser Dissertation ist an der TU Wien Bibliothek verfügbar.
The approved original version of this doctoral thesis is available in print at TU Wien Bibliothek.
TU Bibliothek, WIEN, Your knowledge hub

Electrical resistivity tomography (ERT) measurements have been carried out along eight transects in the stream corridor and on the adjacent footslopes (Figure A1a, blue lines) that allowed to identify the subsurface structure. ERT measurements were carried on following the protocol of Gourdol et al. (2021) using an IRIS Instruments resistivity meter (Syscal Pro 120, ten-channel) with multicore cables equipped with 120 stainless steel rod electrodes using 50 cm spacing increments and obtained the precise location of every electrode using a Trimble DR3300 Total station. The subsurface regolith interfaces were assumed to be located at the maximum change in the resistivity in space (Figure A1b).

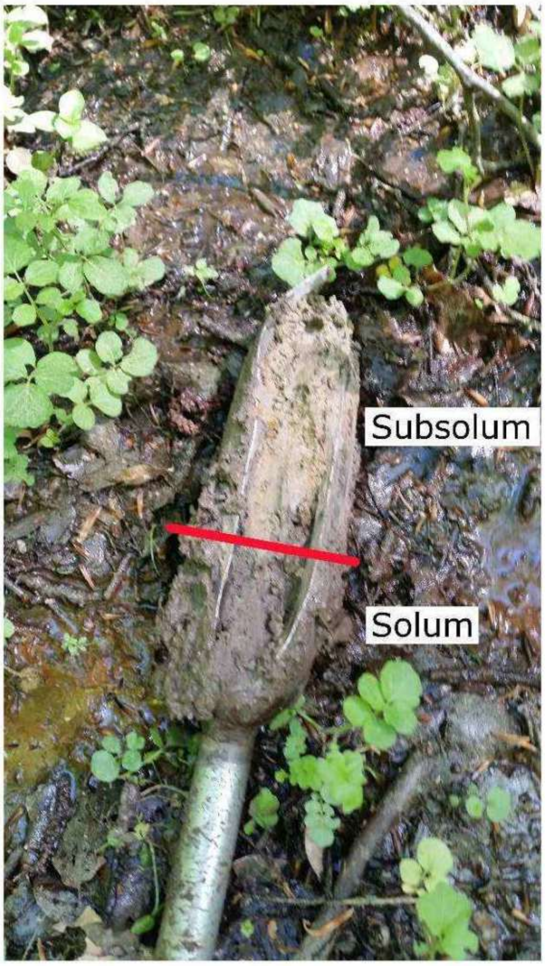

Figure A2. Visual determination of the interface between subsolum and solum in the riparian wetland by the use of a hand-drilling probe.

In-situ inspections and a hand-drilling campaign have been carried out to determine subsurface layers in the riparian zone. The interface between solum and subsolum has been derived by visual inspections (brown vs grey texture, indicating intermittent saturation for the solum and an almost persistent saturation in the subsolum, Figure A2) of drill cores. Subsolum was identified by hand drilling and is characterized by an increase of tangential resistance during drilling due to the higher presence of rock fragments compared to solum. The interface between subsolum and fractured bedrock has been assigned to a depth where hand-drilling was not able to proceed.

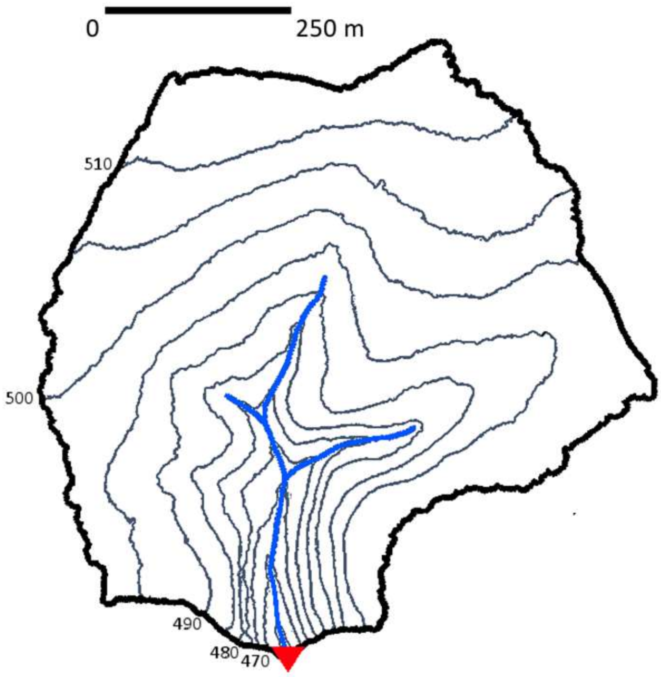

Figure A3. Map of the Weierbach catchment. The red triangle indicates the location of the stream gauge, and coincides with the beginning of the investigated stream reach (red triangle in Figure 1.1) at coordinates 49°49’38” N, 5°47’44” E. The elevation lines go by increments of 5 m from 460 to 510 m.a.s.l.

Appendix B

Table B. Details for the groundwater and piezometer network at the study site.

Well/piezometer	Topographical elevation (m a.r.p.)	Well depth from the topographical surface (m)	Solum-subsolum interface elevation (m a.r.p.)	Subsolum-fractured bedrock interface elevation (m a.r.p.)	Depth surface-subsolum (m)	Depth surface-fractured bedrock (m)	Screened well length (m)
1W1	6.23	0.71	6.15	6.09	0.08	0.14	0.50
1W2	6.12	0.56	6.10	6.0	0.02	0.12	0.50
2W1	5.96	0.67	5.96	5.69	0.00	0.27	0.50
2W2	5.87	0.7	5.86	5.69	0.01	0.18	0.50
3W1	5.72	0.77	5.70	5.24	0.02	0.48	0.50
3P1	5.33	0.29	5.33	5.33	/	/	/
3W2	5.56	0.69	5.44	5.18	0.12	0.38	0.50
4W1	5.59	1.1	5.59	5.00	0.00	0.59	1.00
4P1	5.12	0.39	5.12	5.12	/	/	/
4W2	5.39	0.76	5.22	4.85	0.17	0.54	0.50
5W1	6.21	2.29	5.50	4.60	0.71	1.61	2.00
5W2	5.26	1.38	5.10	4.60	0.16	0.66	1.00
5W3	5.15	0.75	5.00	4.51	0.15	0.64	0.50
5W4	6.30	2.6	5.90	4.20	0.40	2.10	2.00
6W1	4.85	0.81	4.70	4.30	0.15	0.55	0.50
6P1	4.7	0.53	4.70	4.70	/	/	/
6P2	4.72	0.63	4.72	4.72	/	/	/
6W2	5.42	1.38	5.15	4.35	0.27	1.07	1.00
6W3	6.22	2.08	5.77	4.16	0.45	2.06	2.00
7W1	4.71	1.24	4.50	4.15	0.21	0.56	1.00
7W2	4.63	0.68	4.57	4.25	0.06	0.38	0.50
7W3	4.67	0.69	4.65	4.35	0.02	0.32	0.50
8W1	4.24	0.97	4.10	3.87	0.14	0.37	0.80
8P1	3.82	0.39	3.82	3.82	/	/	/
8W2	4.23	0.80	4.15	3.88	0.08	0.35	0.50
8W3	4.38	0.96	4.05	3.70	0.33	0.68	0.60
8W4	4.59	0.81	4.15	4.00	0.44	0.59	0.50
8W5	5.95	2.53	5.56	4.10	0.39	1.85	2.00
9W1	4.86	2.29	4.25	3.70	0.61	1.16	2.00
9W2	4.04	1.06	3.80	3.55	0.24	0.49	0.70
9P1	3.61	0.46	3.61	3.61	/	/	/
9W3	3.96	0.88	3.90	3.65	0.06	0.31	0.60
9W4	4.21	0.92	4.02	3.55	0.19	0.66	0.70

TU Bibliothek Your knowledge hub WIEN
Die approbierte gedruckte Originalversion dieser Dissertation ist an der TU Wien Bibliothek verfügbar.
The approved original version of this doctoral thesis is available in print at TU Wien Bibliothek.

9W5	4.49	0.97	3.90	3.80	0.59	0.69	0.80
9W6	5.59	2.32	5.35	4.15	0.24	1.44	2.00
10W1	3.79	0.90	3.63	3.33	0.16	0.46	0.70
10W2	3.56	0.64	3.53	3.35	0.03	0.21	0.50
10W3	3.68	0.77	3.40	3.10	0.28	0.58	0.60
10W4	3.99	1.01	3.30	3.00	0.69	0.99	0.80
11W1	3.31	1.13	3.21	2.88	0.10	0.43	0.80
11P1	2.95	0.39	2.95	2.95	/	/	/
11W2	3.25	0.64	3.17	2.86	0.08	0.39	0.50
11W3	3.32	0.83	3.22	2.85	0.10	0.47	0.70

Die approbierte gedruckte Originalversion dieser Dissertation ist an der TU Wien Bibliothek verfügbar.
The approved original version of this doctoral thesis is available in print at TU Wien Bibliothek.
TU WIEN Bibliothek Your knowledge hub

Appendix C

Spearman Rank correlation coefficients (in time) between the groundwater increase (ΔGW_H, Table C1) and groundwater rising time (ΔGW_t, Table C2) after a precipitation event of a specific well (e.g. 5W1, 5W2) with precipitation characteristics (depth and intensity), and the initial hydrological status of the system (antecedent dry days and initial groundwater level at the same well). Bold font: significant correlation (*p*-values of Mann-Whitney test less than 0.05). Spearman Rank correlation coefficients are evaluated for the whole time series (TOT) and in different hydrologic conditions: dry, intermediate, and wet. Note that precipitation events that did not trigger a groundwater level increase had ΔGW_t=NaN and were discarded for the Spearman correlation.

Table C1.

			Precipitation depth	Precipitation intensity	Antecedent dry days	Initial GW level
5W1	ΔGW_H	TOT	**0.4298**	**0.2033**	**-0.2368**	**-0.2294**
		Dry	**0.7815**	0.2704	-0.2492	-0.1648
		Int	**0.4498**	0.2179	-0.0570	-0.1243
		Wet	**0.4009**	0.1136	**-0.3412**	-0.0919
5W2	ΔGW_H	TOT	**0.5695**	**0.5135**	0.0070	**-0.4100**
		Dry	**0.8077**	0.2606	-0.1464	-0.1801
		Int	**0.7758**	**0.7541**	-0.0763	-0.4476
		Wet	**0.5805**	**0.3214**	-0.1991	-0.1164
5W3	ΔGW_H	TOT	**0.6308**	**0.4105**	-0.0610	**-0.2561**
		Dry	**0.6543**	**0.3622**	-0.0684	**-0.3307**
		Int	**0.9037**	**0.6541**	-0.0346	-0.3053
		Wet	**0.6363**	**0.3210**	-0.0860	-0.1146
5W4	ΔGW_H	TOT	**0.5644**	**0.3023**	**-0.1688**	-0.0972
		Dry	**0.7771**	0.2219	-0.1347	-0.3049
		Int	**0.8798**	**0.6991**	-0.1441	-0.2330

		Wet	**0.4935**	**0.2052**	**-0.2805**	0.0060
6W1	ΔGW_H	TOT	**0.5105**	**0.3893**	-0.0293	**-0.3585**
		Dry	**0.6310**	0.0802	-0.2022	-0.2133
		Int	**0.8148**	**0.6379**	0.0507	-0.2650
		Wet	**0.5393**	**0.3336**	-0.1480	-0.0813
6W2	ΔGW_H	TOT	**0.5531**	**0.4064**	0.0083	**-0.4566**
		Dry	**0.8224**	0.2140	-0.0777	-0.2412
		Int	**0.8789**	**0.7009**	0.0071	-0.3265
		Wet	**0.5741**	**0.3098**	-0.1392	**-0.2461**
6W3	ΔGW_H	TOT	**0.5535**	**0.2723**	**-0.2091**	**-0.1414**
		Dry	**0.7567**	0.0686	-0.1123	-0.3073
		Int	**0.7877**	**0.6150**	-0.0995	-0.1149
		Wet	**0.5184**	**0.2322**	**-0.2709**	-0.0845
7W1	ΔGW_H	TOT	**0.5384**	**0.3805**	0.0042	**-0.4032**
		Dry	**0.7422**	0.0928	-0.0362	**-0.3249**
		Int	**0.8764**	**0.5870**	0.0533	**-0.4101**
		Wet	**0.5501**	**0.3175**	-0.1446	-0.1433
7W2	ΔGW_H	TOT	**0.4647**	**0.3471**	0.0751	**-0.5693**
		Dry	**0.7987**	0.1885	0.0489	**-0.3956**
		Int	**0.8621**	**0.6513**	0.0259	-0.3230
		Wet	**0.4234**	**0.2347**	-0.0302	**-0.4985**
7W3	ΔGW_H	TOT	**0.4203**	**0.2955**	**-0.1494**	**-0.3689**
		Dry	**0.7776**	**0.4047**	**-0.3341**	-0.1180
		Int	**0.8444**	**0.6830**	-0.0737	0.0363
		Wet	**0.3485**	0.1489	-0.1491	**-0.2193**
8W1	ΔGW_H	TOT	**0.5394**	**0.3465**	-0.0168	**-0.2862**
		Dry	**0.7497**	0.0719	0.1360	**-0.3336**
		Int	**0.8979**	**0.6040**	-0.0496	**-0.3764**
		Wet	**0.4876**	**0.2514**	**-0.1798**	-0.0686
8W2	ΔGW_H	TOT	**0.4490**	**0.3511**	0.0663	**-0.5092**
		Dry	**0.7961**	0.1935	-0.0329	**-0.3337**
		Int	**0.8177**	**0.5795**	0.1712	**-0.5420**
		Wet	**0.4483**	**0.2417**	-0.0935	**-0.2557**

8W5	ΔGW_H	TOT	**0.5859**	**0.3174**	-0.1128	**-0.3179**
		Dry	**0.8359**	0.1866	-0.0424	-0.3338
		Int	**0.8933**	**0.5689**	0.1699	-0.2841
		Wet	**0.5440**	**0.2641**	**-0.2048**	**-0.2258**
9W1	ΔGW_H	TOT	**0.6280**	**0.3792**	-0.0188	**-0.2785**
		Dry	**0.6960**	0.2869	0.0869	-0.2273
		Int	**0.9005**	**0.6602**	0.0301	-0.2722
		Wet	**0.5870**	**0.2771**	-0.1215	**-0.2091**
9W2	ΔGW_H	TOT	**0.6179**	**0.4009**	-0.0254	**-0.2709**
		Dry	**0.7755**	**0.3788**	0.1574	**-0.5172**
		Int	**0.8150**	**0.7610**	-0.0026	-0.2273
		Wet	**0.5778**	**0.2795**	-0.1443	**-0.1798**
9W3	ΔGW_H	TOT	**0.4127**	**0.4276**	**0.1351**	**-0.7218**
		Dry	**0.7736**	0.2816	0.1133	**-0.4225**
		Int	**0.8195**	**0.6568**	-0.0376	-0.1907
		Wet	**0.3660**	**0.3268**	0.0606	**-0.7866**
9W6	ΔGW_H	TOT	**0.7213**	**0.4849**	-0.0629	**-0.1998**
		Dry	**0.8229**	0.2203	-0.1583	-0.1735
		Int	**0.8684**	**0.7051**	-0.0794	-0.2401
		Wet	**0.7015**	**0.4457**	-0.1241	-0.0802
10W1	ΔGW_H	TOT	**0.6159**	**0.3667**	0.0444	**-0.3061**
		Dry	**0.5832**	0.1120	0.1587	**-0.5110**
		Int	**0.8649**	**0.6849**	0.0080	-0.2289
		Wet	**0.5997**	**0.3103**	-0.0463	**-0.2951**
10W2	ΔGW_H	TOT	**0.3480**	**0.3336**	**0.2436**	**-0.7617**
		Dry	**0.7814**	0.2432	0.1178	**-0.4913**
		Int	**0.8316**	**0.5144**	0.2623	**-0.5817**
		Wet	**0.3887**	**0.2265**	**0.1790**	**-0.5699**
11W1	ΔGW_H	TOT	**0.5791**	**0.3990**	0.0038	**-0.3615**
		Dry	**0.5510**	0.1193	0.2181	**-0.5416**
		Int	**0.8475**	**0.6743**	-0.0175	-0.1678
		Wet	**0.5933**	**0.2972**	**-0.1771**	**-0.1612**
11W2	ΔGW_H	TOT	**0.7208**	**0.5152**	0.1127	**-0.2638**

		Dry	**0.4790**	0.0775	**0.3445**	**-0.6901**
		Int	**0.8933**	**0.6472**	0.0239	-0.3232
		Wet	**0.7803**	**0.4893**	-0.0095	-0.0543
11W3	ΔGW_H	TOT	**0.8007**	**0.5148**	0.0455	**-0.1619**
		Dry	**0.7124**	0.2760	0.0018	-0.1611
		Int	**0.8995**	**0.6708**	0.0020	-0.2242
		Wet	**0.8143**	**0.4768**	0.0049	-0.0907

Table C2.

			Precipitation depth	Precipitation intensity	Antecedent dry days	Initial GW level
5W1	ΔGW_t	TOT	-0.0879	-0.1328	**0.3423**	**0.1935**
		Dry	-0.2283	-0.1157	0.3021	0.1248
		Int	-0.2386	**-0.4572**	**0.5768**	-0.0445
		Wet	-0.0714	-0.0549	**0.4268**	0.0221
5W2	ΔGW_t	TOT	**-0.2870**	**-0.3843**	-0.0298	**0.2680**
		Dry	-0.1526	**-0.6086**	0.3857	**-0.5936**
		Int	-0.4286	-0.7143	-0.1160	0.4554
		Wet	**-0.4327**	-0.2089	0.0887	-0.0593
5W3	ΔGW_t	TOT	**-0.2659**	**-0.3684**	**0.1942**	-0.0293
		Dry	**-0.3934**	**-0.4711**	**0.4153**	-0.1452
		Int	-0.1427	**-0.4789**	0.1789	0.1839
		Wet	**-0.2863**	**-0.3640**	0.1125	-0.0559
5W4	ΔGW_t	TOT	-0.0317	**-0.1852**	**0.2145**	0.0247
		Dry	-0.1089	-0.1612	**0.4551**	-0.0449
		Int	-0.4616	-0.4819	**0.5034**	0.0901
		Wet	-0.0032	-0.1081	**0.2625**	**-0.2280**
6W1	ΔGW_t	TOT	-0.0330	**-0.4192**	0.0007	**0.1972**
		Dry	-0.0437	-0.2573	0.1318	-0.1578
		Int	-0.2205	-0.3835	-0.0178	-0.0168
		Wet	-0.0879	**-0.4487**	0.0803	-0.0709
6W2	ΔGW_t	TOT	-0.0771	**-0.4388**	0.0112	**0.4044**
		Dry	-0.0834	**-0.4572**	**0.3639**	-0.2186
		Int	-0.1592	-0.3298	0.3117	0.2272

Die approbierte gedruckte Originalversion dieser Dissertation ist an der TU Wien Bibliothek verfügbar.
The approved original version of this doctoral thesis is available in print at TU Wien Bibliothek.
TU Bibliothek WIEN Your knowledge hub

		Wet	-0.1684	**-0.4290**	0.0798	**0.1907**
6W3	ΔGW_t	TOT	0.0454	**-0.1794**	**0.2061**	0.1570
		Dry	0.1378	-0.1094	**0.6958**	0.1071
		Int	0.5571	0.3088	**0.6837**	-0.1522
		Wet	-0.0425	-0.1804	**0.1856**	-0.0733
7W1	ΔGW_t	TOT	-0.0947	**-0.3023**	-0.0664	**0.3824**
		Dry	-0.0051	-0.2608	-0.0434	-0.0732
		Int	-0.1797	-0.2831	-0.1400	0.1362
		Wet	**-0.2120**	**-0.2413**	0.1208	0.0216
7W2	ΔGW_t	TOT	-0.0782	**-0.3539**	-0.0568	**0.3600**
		Dry	-0.3005	-0.2607	-0.0619	0.3076
		Int	-0.3309	**-0.5402**	0.2024	-0.1207
		Wet	-0.0439	**-0.3032**	-0.0048	**0.3819**
7W3	ΔGW_t	TOT	**-0.1647**	**-0.3577**	**0.2817**	0.1115
		Dry	**-0.3918**	**-0.4978**	**0.5676**	-0.1286
		Int	0.1559	-0.2447	**0.6432**	**-0.5746**
		Wet	-0.1504	**-0.3136**	0.1544	-0.0099
8W1	ΔGW_t	TOT	-0.1316	**-0.2912**	0.0473	**0.3210**
		Dry	-0.2568	-0.3185	0.0241	0.3215
		Int	-0.2774	-0.2809	0.1972	**0.5499**
		Wet	-0.1016	**-0.2347**	0.0998	0.1601
8W2	ΔGW_t	TOT	**-0.1471**	**-0.3450**	0.0330	**0.2029**
		Dry	-0.1300	**-0.3816**	0.0860	-0.0450
		Int	**-0.4503**	**-0.5029**	0.1081	**0.4134**
		Wet	-0.1161	**-0.2650**	0.1234	0.0971
8W5	ΔGW_t	TOT	0.0150	**-0.2307**	**0.1817**	**0.1938**
		Dry	-0.2137	**-0.6076**	0.1846	0.0151
		Int	0.0718	-0.4586	**0.6777**	-0.0572
		Wet	-0.0050	-0.1532	**0.1900**	0.0796
9W1	ΔGW_t	TOT	**-0.1933**	**-0.3412**	-0.0189	**0.3092**
		Dry	-0.1920	-0.2616	0.0478	**0.4134**
		Int	-0.3793	**-0.4364**	0.0413	0.3697
		Wet	**-0.1973**	**-0.3062**	0.0098	**0.2607**

Die approbierte gedruckte Originalversion dieser Dissertation ist an der TU Wien Bibliothek verfügbar.
The approved original version of this doctoral thesis is available in print at TU Wien Bibliothek.
TU Bibliothek
Your knowledge hub
WIEN

Die approbierte gedruckte Originalversion dieser Dissertation ist an der TU Wien Bibliothek verfügbar.
The approved original version of this doctoral thesis is available in print at TU Wien Bibliothek.
TU WIEN Bibliothek Your knowledge hub

9W2	ΔGW_t	TOT	-0.0718	**-0.4329**	-0.1122	**0.3048**
		Dry	-0.1642	-0.3000	-0.2350	**0.3539**
		Int	-0.4474	**-0.5983**	0.2895	0.1007
		Wet	-0.0772	**-0.3583**	-0.0250	0.1640
9W3	ΔGW_t	TOT	0.0384	**-0.3818**	-0.0702	**0.3247**
		Dry	-0.0497	-0.1052	-0.2453	0.0662
		Int	0.0426	-0.1832	0.2381	**-0.3919**
		Wet	0.0317	**-0.4144**	-0.0348	**0.4677**
9W6	ΔGW_t	TOT	-0.1455	**-0.4532**	0.0825	**0.1662**
		Dry	-0.1149	-0.2056	0.0033	0.1902
		Int	**-0.4762**	**-0.6497**	0.3189	-0.0384
		Wet	-0.1779	**-0.4760**	**0.2064**	-0.1144
10W1	ΔGW_t	TOT	-0.0667	**-0.1999**	0.0543	**0.1658**
		Dry	-0.0734	0.1472	0.0096	**0.4517**
		Int	-0.2594	-0.4543	0.0805	-0.1819
		Wet	-0.0597	**-0.2170**	0.1109	0.1079
10W2	ΔGW_t	TOT	0.0109	**-0.3087**	-0.1520	**0.5055**
		Dry	-0.0228	**-0.4176**	-0.1048	0.0627
		Int	-0.3114	-0.2370	-0.1421	0.3116
		Wet	0.0253	-0.2071	-0.0729	**0.5667**
11W1	ΔGW_t	TOT	-0.1188	**-0.2731**	-0.0063	**0.1605**
		Dry	-0.0112	-0.2077	0.0339	0.2557
		Int	-0.0854	**-0.5224**	-0.0405	0.3062
		Wet	**-0.2169**	**-0.2592**	0.1061	-0.0102
11W2	ΔGW_t	TOT	-0.0623	**-0.4665**	-0.0906	**0.1674**
		Dry	0.1118	**-0.3827**	0.1918	0.1734
		Int	-0.2040	-0.4069	0.1075	-0.0510
		Wet	-0.1359	**-0.4714**	-0.0508	-0.0196
11W3	ΔGW_t	TOT	**-0.1937**	**-0.4618**	0.0240	-0.0598
		Dry	-0.0198	-0.1138	0.1093	-0.0071
		Int	-0.5846	**-0.5139**	0.2009	0.1064
		Wet	-0.1422	**-0.5397**	-0.0064	0.0411

Table C3 Spearman Rank correlation coefficients (in space) between the average precipitation depth that does not trigger a groundwater increase >1cm, the mean lag-time of the groundwater response after the beginning of a precipitation event (ΔGWt), and the mean groundwater increase following an event (ΔGWH) with local characteristics of the groundwater-monitoring network (regolith thickness between the topographic surface and the surface of the fractured bedrock, the regolith thickness between the topographic surface and the surface of the subsolum, elevation above and distance from the streambed). Bold font: significant correlation (p-values of Mann-Whitney test less than 0.05). Spearman Rank correlation coefficients are evaluated for different hydrologic conditions: dry, intermediate and wet.

		Depth surface-fractured bedrock (cm)	Depth surface-subsolum (cm)	Well topographic elevation above the streambed	Distance from the stream (m)
Average precipitation depth that does not trigger a groundwater increase	Dry	0.2264	0.1647	-0.0855	-0.0894
	Int	0.3977	**0.4650**	0.3087	-0.0896
	Wet	-0.3660	-0.2775	-0.2588	0.1687
(ΔGW_t)	Dry	**0.4512**	0.4197	0.3841	0.2830
	Int	0.2569	0.2800	0.1542	-0.0198
	Wet	**0.6793**	**0.6239**	**0.5168**	**0.4308**
(ΔGW_H)	Dry	-0.1914	-0.3767	**-0.4355**	-0.1942
	Int	-0.1417	-0.2178	-0.0683	0.1245
	Wet	**0.4270**	0.3765	0.3977	0.1931

parameter interval where the model is more sensitive to that parameter. The measure of the local gradient of the cumulative distribution will be represented by the height of the bar plot in each equally-sized bin across the parameter range. Higher bars and steeper gradients of the CDF line indicate greater model performances in that parameter range and, therefore, parameter sensitivity and identifiability (Figure D1g). On the contrary, equal eight of the bars and similar gradients of the CDF line indicate that the parameter is insensitive and non-identifiable (Figure D1h).

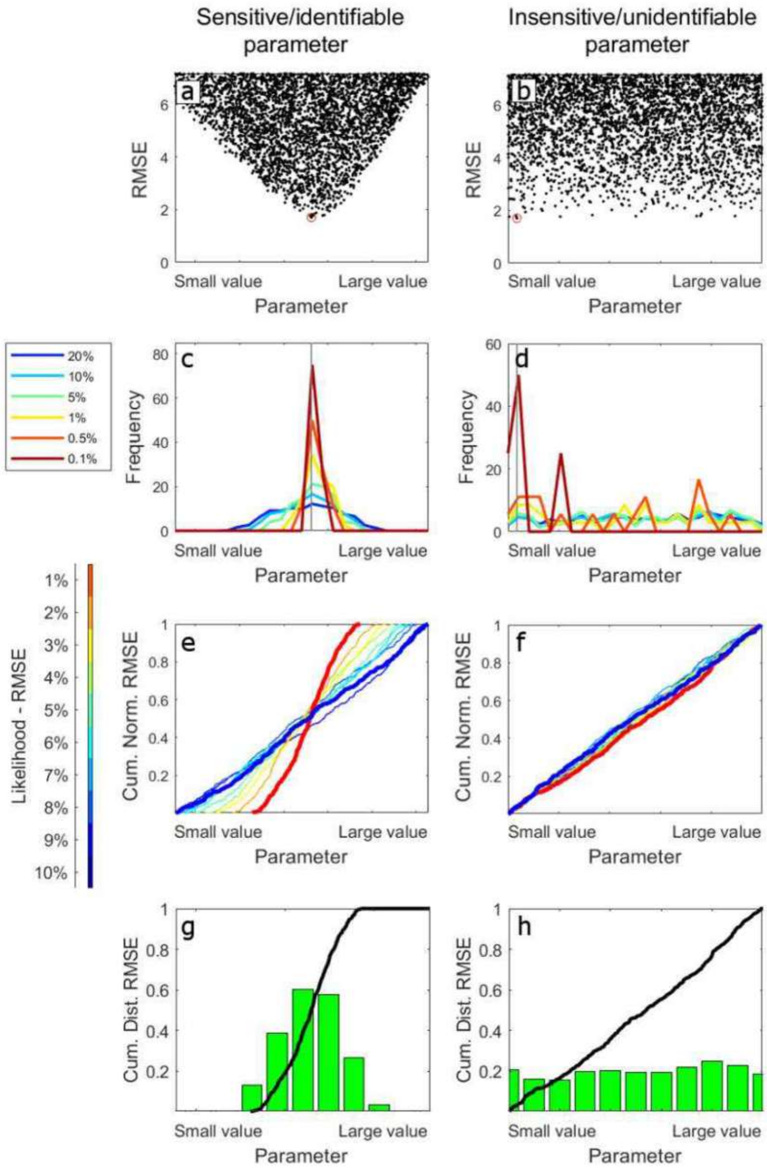

Figure D1: Examples of the four types of visualizations intended for parameter identifiability and sensitivity with the plots in the first column (a, c, e, and g) reporting an example of plots for sensitive and identifiable parameter and plots in the second column (b, d, f, and h) reporting an example of plots for insensitive and non-identifiable parameter. (a) and (b) parameter vs likelihood plots; (c) and (d) parameter distribution plots for the top 20, 10, 5, 1, and 0.1% of the results; (e) and (f) regional sensitivity analysis plots from the top 1% to the top 10% of the results; (g) and (h) identifiability plots for the top 1% of the model results.

Die approbierte gedruckte Originalversion dieser Dissertation ist an der TU Wien Bibliothek verfügbar.
The approved original version of this doctoral thesis is available in print at TU Wien Bibliothek.
TU Bibliothek Your knowledge hub WIEN

The plots used to address the global sensitivity analysis indicate parameter identifiability and sensitivity on the entire observed BTC, however they are unable to address if the *i-th* parameter describes the process it is meant to represent or if the role of the *i-th* parameter on the model is constant in time (Wagener and Kollat, 2007). To address identifiability and sensitivity of the *i-th* parameter on the different sections of the BTC we applied dynamic identifiability analysis which steps are reported in Figure D2 (Wagener et al., 2002).

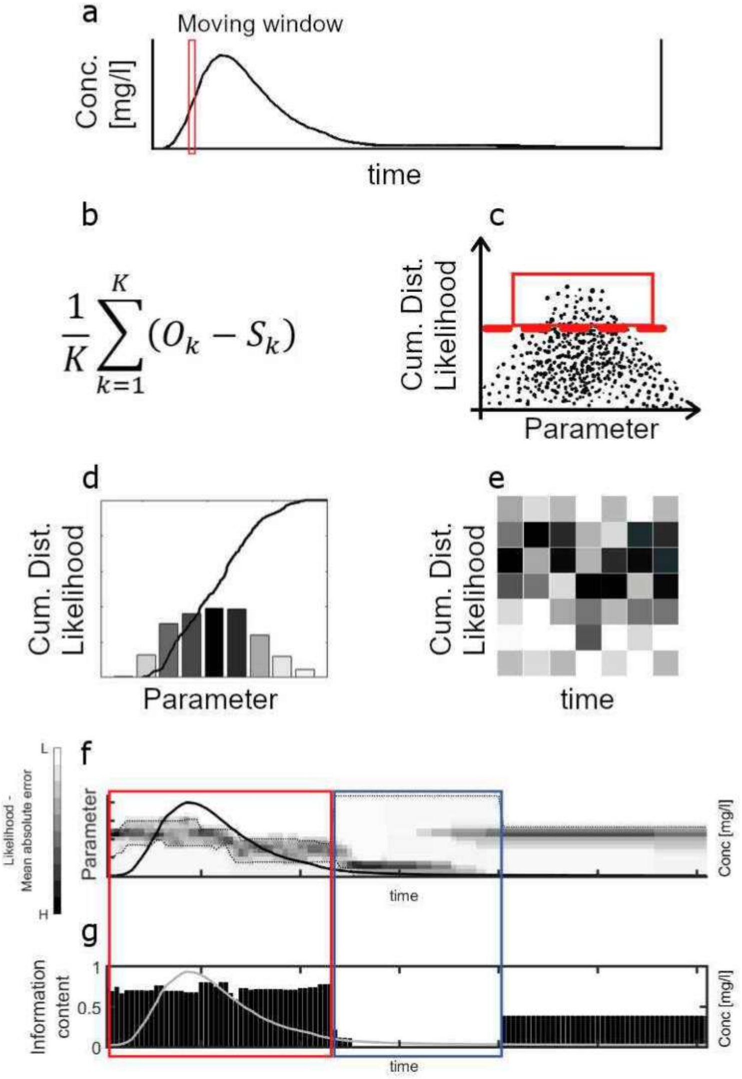
a
Moving window
Conc. [mg/l]
time
b
$\frac{1}{K}\sum_{k=1}^{K}(O_k - S_k)$
c
Cum. Dist. Likelihood
Parameter
d
Cum. Dist. Likelihood
Parameter
e
Cum. Dist. Likelihood
time
f
L
Likelihood - Mean absolute error
H
Parameter
time
Conc [mg/l]
g
Information content
1
0.5
0
time
Conc [mg/l]

Figure D2. Dynamic identifiability analysis algorithm flowchart. (a) The BTC is subdivided in moving windows (size equal to three times the BTC timestep, Wagener et al., 2002); (b) In each moving window the likelihood (efficiency) of every TSM simulation is evaluated via mean absolute error (Wagener and Kollat, 2007); (c) an efficiency-threshold is chosen (e.g. top 10%); (d) for the chosen model results, the cumulative distribution function is built for each investigated parameter; (e) steps from (b) to (d) are repeated for each moving window and model likelihood for the investigated parameter is plotted over time (white: minimum likelihood; black: maximum likelihood). (f) cumulative distribution function of the parameter distribution is plot vs the observed BTC together with 90% confidence limits. Narrow limits indicate identifiable parameter while wide limits indicate unidentifiable parameter. (g) a second plot reports the metric of one minus the normalized distance between the 90% confidence limits. Small values of this metric indicate that the selected time window contain a narrow identifiability range for the investigated parameter and, therefore, that it is informative on that part of the BTC (Wagener et al., 2002).

Die approbierte gedruckte Originalversion dieser Dissertation ist an der TU Wien Bibliothek verfügbar.
The approved original version of this doctoral thesis is available in print at TU Wien Bibliothek.
TU Bibliothek WIEN Your knowledge hub

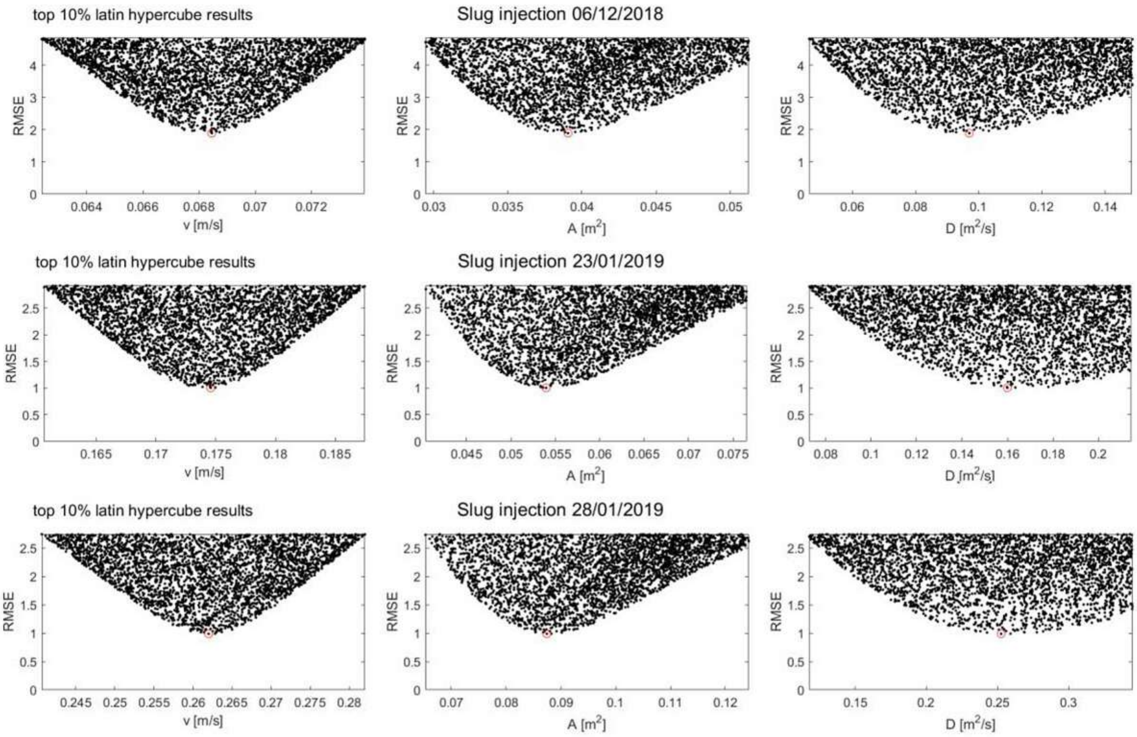

Figure D3. Parameter values plotted against the corresponding *RMSE* values for the ADE results for E1, E2, and E3.

Appendix E

The figure E1 shows the observed BTC for the three tracer experiments plotted against the top 100 simulated BTC obtained using the proposed iterative approach. The observed poor visual fit on the tail of the BTC obtained at the end of the iterative modelling approach (Figure E1d, e, f) is controlled by two factors: (i) the modelling structure of the TSM which assumes an exponential residence time distribution and (ii) the chosen objective function. By using alternative residence time distributions, TSM proved to have a more accurate fitting on the tail of the BTC (Haggerty et al., 2002; Bottacin-Busolin et al., 2011). Also, the RMSE could not be the best objective function for addressing a model fit on the tail of BTC because it gives higher importance on the sections of the BTC with higher concentration values (peak of the BTC) compared to the sections of the BTC with low concentration values (at the tail of the BTC). As an example, the best-fitting BTC obtained at the end of the second TSM iteration (E1) shows a visually better fit on the BTC tail (Figure E2) despite the large RMSE (1.5197 mg/l).

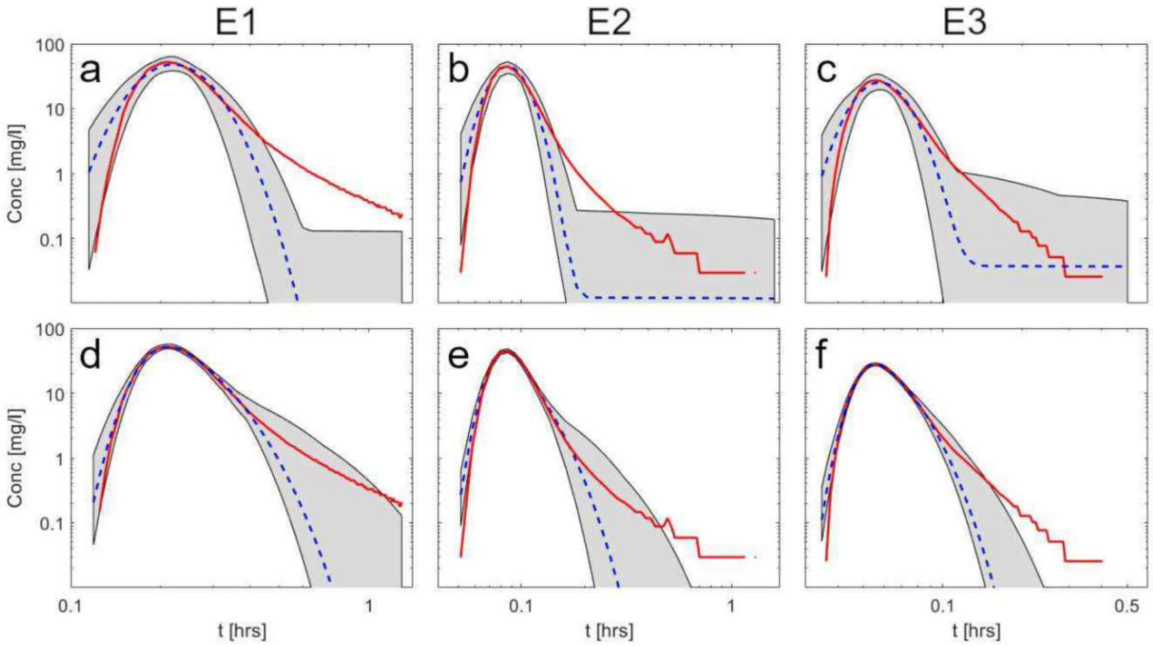

Figure E1: Observed BTC (red line) together with the grey area comprised between the top 100 simulated BTCs and the best-fitting BTC (blue dashed line) for (a, d) E1, (b, e) E2, and (c, f) E3. Results reported for the first (a, b, c) and last (d, e, f) TSM iterations.

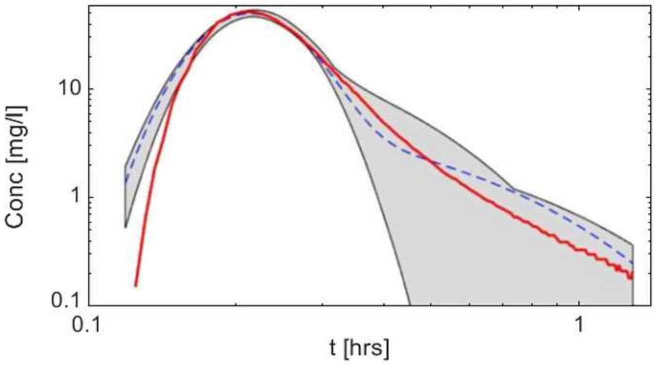

Figure E2: Observed BTC (red line) together with the grey area comprised between the top 100 simulated BTCs and the best-fitting BTC (blue dashed line) for the second TSM iteration (E1).

Die approbierte gedruckte Originalversion dieser Dissertation ist an der TU Wien Bibliothek verfügbar.
The approved original version of this doctoral thesis is available in print at TU Wien Bibliothek.
TU WIEN Bibliothek Your knowledge hub

Appendix F

Table F. Comparison between modelling results via iterative modelling approach and OTIS-P for 31 slug tracer experiments.

		v	A	D	α	A_{TS}	*RMSE*
E1	*OTIS-P*	0.0733	0.0364	0.0637	0.0006	0.0074	**0.6159**
	Identifiability analysis	0.0729	0.0370	0.0523	0.0014	0.0073	0.7230
E2	*OTIS-P*	0.2619	0.0540	0.1498	0.0052	0.0189	0.5375
	Identifiability analysis	0.2732	0.0543	0.1111	0.0078	0.0182	**0.4462**
E3	*OTIS-P*	0.1236	0.0374	0.0705	0.0016	0.0066	0.6745
	Identifiability analysis	0.1220	0.0392	0.0758	0.0017	0.0057	**0.6517**
E4	*OTIS-P*	0.11	0.0356	0.0738	0.001	0.0064	**0.6289**
	Identifiability analysis	0.1111	0.0365	0.0678	0.0017	0.0056	0.6852
E5	*OTIS-P*	0.1774	0.0509	0.1151	0.0016	0.0077	0.4152
	Identifiability analysis	0.1863	0.0531	0.0927	0.0037	0.0076	**0.2897**
E6	*OTIS-P*	0.1667	0.0479	0.09209	0.0025	0.0071	**0.4917**
	Identifiability analysis	0.1755	0.0479	0.0759	0.0051	0.0083	0.6057
E7	*OTIS-P*	0.275	0.081	0.1404	0.005	0.0144	**0.2544**
	Identifiability analysis	0.2894	0.0793	0.1189	0.0069	0.0159	0.2844
E8	*OTIS-P*	0.2292	0.0728	0.1752	0.0031	0.0122	0.3406
	Identifiability analysis	0.2440	0.0741	0.1440	0.0055	0.0140	**0.2344**
E9	*OTIS-P*	0.2444	0.0689	0.1475	0.0045	0.0128	**0.3490**
	Identifiability analysis	0.2550	0.0674	0.1259	0.0062	0.0142	0.3570
E10	*OTIS-P*	0.2245	0.0723	0.1778	0.0025	0.0104	0.3923
	Identifiability analysis	0.2503	0.0685	0.0984	0.0102	0.0176	**0.3262**
E11	*OTIS-P*	0.1250	0.0439	0.1566	0.0008	0.0071	**0.5482**
	Identifiability analysis	0.1206	0.0434	0.1566	0.0008	0.0076	0.6337
E12	*OTIS-P*	0.1279	0.0401	0.1475	0.0008	0.0059	**0.6228**
	Identifiability analysis	0.1226	0.0403	0.1488	0.0009	0.0052	0.6584
E13	*OTIS-P*	NaN	NaN	NaN	NaN	NaN	NaN
	Identifiability analysis	0.1210	0.0425	0.1557	0.0008	0.0082	**0.3840**
E14	*OTIS-P*	0.3438	0.0871	0.2694	0.0020	0.0162	0.3828
	Identifiability analysis	0.3486	0.0900	0.1984	0.0050	0.0130	**0.2075**
E15	*OTIS-P*	0.3235	0.0800	0.2775	0.0029	0.0139	0.4007
	Identifiability analysis	0.3506	0.0785	0.1816	0.0102	0.0177	**0.1953**

E16	*OTIS-P*	0.6707	0.1112	0.8761	0.0105	0.0226	0.2009
	Identifiability analysis	0.8239	0.0973	0.4599	0.0420	0.0403	**0.1172**
E17	*OTIS-P*	NaN	NaN	NaN	NaN	NaN	NaN
	Identifiability analysis	0.3858	0.1043	0.2582	0.0097	0.0283	**0.3986**
E18	*OTIS-P*	0.0591	0.0224	0.0332	0.0012	0.0082	**1.9087**
	Identifiability analysis	0.0583	0.0221	0.0346	0.0012	0.0082	2.2046
E19	*OTIS-P*	NaN	NaN	NaN	NaN	NaN	NaN
	Identifiability analysis	0.0480	0.0206	0.0181	0.0012	0.0074	**2.0557**
E20	*OTIS-P*	0.0308	0.0140	0.0213	0.0005	0.0068	2.9360
	Identifiability analysis	0.0296	0.0137	0.0200	0.0005	0.0074	**2.8272**
E21	*OTIS-P*	NaN	NaN	NaN	NaN	NaN	NaN
	Identifiability analysis	0.0537	0.0918	0.0575	0.0007	0.0534	**0.3799**
E22	*OTIS-P*	0.1418	0.0362	0.0924	0.0017	0.0060	0.7511
	Identifiability analysis	0.1518	0.0364	0.0716	0.0041	0.0066	**0.4699**
E23	*OTIS-P*	0.1447	0.0359	0.1093	0.0012	0.0058	0.6109
	Identifiability analysis	0.1433	0.0371	0.1006	0.0016	0.0051	**0.4291**
E24	*OTIS-P*	0.1447	0.0341	0.0957	0.0018	0.0055	0.6294
	Identifiability analysis	0.1444	0.0340	0.0910	0.0026	0.0055	**0.6104**
E25	*OTIS-P*	0.1410	0.0346	0.1025	0.0013	0.0054	**0.5388**
	Identifiability analysis	0.1414	0.0364	0.0943	0.0022	0.0044	0.5968
E26	*OTIS-P*	0.1392	0.0331	0.0734	0.0028	0.0063	**0.4404**
	Identifiability analysis	0.1399	0.0334	0.0896	0.0022	0.0050	0.4481
E27	*OTIS-P*	0.1390	0.0339	0.0939	0.0015	0.0056	0.5718
	Identifiability analysis	0.1389	0.0341	0.0808	0.0022	0.0057	**0.4866**
E28	*OTIS-P*	0.1375	0.0341	0.0922	0.0015	0.0056	**0.8518**
	Identifiability analysis	0.1399	0.0335	0.0759	0.0025	0.0061	0.9389
E29	*OTIS-P*	0.1341	0.0319	0.1215	0.0008	0.0085	1.2004
	Identifiability analysis	0.1319	0.0337	0.1052	0.0011	0.0049	**0.8392**
E30	*OTIS-P*	0.0917	0.0307	0.0508	0.0009	0.0044	0.7416
	Identifiability analysis	0.0966	0.0311	0.0378	0.0023	0.0052	**0.7226**
E31	*OTIS-P*	0.0902	0.0286	0.0582	0.0006	0.0048	1.1638
	Identifiability analysis	0.0893	0.0305	0.0468	0.0011	0.0041	**0.5656**

TU Bibliothek WIEN Your knowledge hub
Die approbierte gedruckte Originalversion dieser Dissertation ist an der TU Wien Bibliothek verfügbar.
The approved original version of this doctoral thesis is available in print at TU Wien Bibliothek.